University of Alberta

Luminescent Chiral Thin Films Fabricated Using Glancing Angle Deposition

by

Peter Charles Philip Hrudey

A thesis submitted to the Faculty of Graduate Studies and Research in partial fulfillment of the

requirements for the degree of Doctor of Philosophy

Department of Electrical and Computer Engineering

Edmonton, Alberta
Fall 2006

Library and Archives Canada

Published Heritage Branch

395 Wellington Street
Ottawa ON K1A 0N4
Canada

Bibliothèque et Archives Canada

Direction du Patrimoine de l'édition

395, rue Wellington
Ottawa ON K1A 0N4
Canada

Your file Votre référence
ISBN: 978-0-494-23045-9
Our file Notre référence
ISBN: 978-0-494-23045-9

NOTICE:
The author has granted a non-exclusive license allowing Library and Archives Canada to reproduce, publish, archive, preserve, conserve, communicate to the public by telecommunication or on the Internet, loan, distribute and sell theses worldwide, for commercial or non-commercial purposes, in microform, paper, electronic and/or any other formats.

The author retains copyright ownership and moral rights in this thesis. Neither the thesis nor substantial extracts from it may be printed or otherwise reproduced without the author's permission.

AVIS:
L'auteur a accordé une licence non exclusive permettant à la Bibliothèque et Archives Canada de reproduire, publier, archiver, sauvegarder, conserver, transmettre au public par télécommunication ou par l'Internet, prêter, distribuer et vendre des thèses partout dans le monde, à des fins commerciales ou autres, sur support microforme, papier, électronique et/ou autres formats.

L'auteur conserve la propriété du droit d'auteur et des droits moraux qui protège cette thèse. Ni la thèse ni des extraits substantiels de celle-ci ne doivent être imprimés ou autrement reproduits sans son autorisation.

In compliance with the Canadian Privacy Act some supporting forms may have been removed from this thesis.

While these forms may be included in the document page count, their removal does not represent any loss of content from the thesis.

Conformément à la loi canadienne sur la protection de la vie privée, quelques formulaires secondaires ont été enlevés de cette thèse.

Bien que ces formulaires aient inclus dans la pagination, il n'y aura aucun contenu manquant.

Canada

ABSTRACT

Glancing angle deposition (GLAD) can be used to fabricate unique, nanostructured thin films that exhibit intriguing optical properties because the characteristic length scale of the nanostructures is on the order the wavelength of visible light. Previous studies of the optical properties of such films have focused upon the light transmitted, reflected, or scattered by the nanostructures. Here, the optical properties of luminescent chiral thin films were explored. Following the initial structural and optical characterization of simple nanostructured thin films, chiral thin films were shown to exhibit a one-dimensional photonic stop band for one handedness of circularly polarized light, also known as circular Bragg phenomena, for both transmittance experiments and photoluminescence experiments. First inorganic, then organic photoluminescent materials were used to fabricate the luminescent chiral thin films studied, with europium-doped yttrium oxide (Y_2O_3:Eu) serving as the inorganic photoluminescent material and tris-(8-hydroxyquinoline) aluminum (Alq_3) serving as the organic photoluminescent material. Porous chiral Y_2O_3:Eu films were fabricated and found to emit partially circularly polarized light in photoluminescence. The highest degree of circular polarization measured for these chiral Y_2O_3:Eu was ~ 5%. The chiral Alq_3 films constituted the first directly deposited porous nanostructured organic films produced by GLAD. They were found to consist of a nearly hexagonal close-packed array of smooth, uniform helical structures. These structures, which do not tend to broaden with increasing thickness, were used to fabricate samples which exhibited strong circular Bragg phenomena with the degree of circular polarization of light emitted by chiral Alq_3 films reached a magnitude of ~ 71%. The remarkable

structural and optical properties of nanostructured Alq_3 films suggest that novel, directly deposited porous nanostructured organic films will find uses in many applications both within the field of photonics and beyond.

ACKNOWLEDGEMENT

There is a rather large and wonderful group of people to whom I am immeasurably grateful for their help, guidance, and support. First and foremost, I am forever grateful to my supervisor, Dr. Michael Brett, whose positive attitude and infectious enthusiasm for discovery were a constant source of encouragement over the past few years. Your strength and vision over the course of this work has been inspiring. To my examining committee, thank you for your guidance and your excellent suggestions for improving this thesis.

Naturally, the entire, ever-changing GLAD group has been a wonderful influence throughout the course of my research. To Karin Hayward, Dr. Doug Vick, Albert Huizinga, Dr. Jeremy Sit, Dr. Mary Seto, Dr. Ken Harris, Dr. Brian Dick, Dr. Scott Kennedy, Mike Colgan, Dr. Gregory Kiema, Dr. Jim Broughton, Ben Bathgate, Dr. Barb Djufors, Dr. Martin Jensen, Anastasia Elias, Andy van Popta, James Gospodyn, Shufen Tsoi, John Steele, Mark Summers, Matt Hawkeye, Doug Gish, Jason Sorge, Bryan Szeto, Nick Wakefield, Graeme Dice, and Dr. Mike Fleischauer, you all deserve more thanks than I can possibly offer here, but please know that I have valued all of the helpful discussions and distractions that I have enjoyed with you all over the years.

Thanks must also go to all of those individuals external to the GLAD group who I have collaborated with – Mike Taschuk, Dr. Robert Fedosejevs, Dr. Ying Tsui, Aaron Hryciw, Dr. Al Meldrum, Dr. Jon Veinot, and Dr. Dick Broer – who each provided valuable insights, advice, and suggestions over the course of my various research projects. Similarly, many thanks go to Dr. Ken Westra, Keith Franklin, Stephanie Bozic, Bob

Brebber, Shane McColman, Aruna Kroetch, and the rest of the staff at the Nanofab with which I have had the pleasure of working. Similarly, I thank the staff of the Alberta Centre for Surface Engineering and Science (ACSES) and Shiraz Merali of the Department of Chemical Engineering for their assistance with the compositional analysis and XRD analysis, respectively, contained in this thesis. And, to my very talented SEM mentor, George Braybrook, I am deeply grateful, both for your phenomenal skills at imaging the samples studied in this thesis, and for teaching me some of those skills along the way.

The final group of people to whom I owe so much is that of my family and close friends. Mom, Dad, Steve, and Jess, I could not have done this without your support and love. Thank you for teaching me to be the person I am. To Kim, Lu, and Ryder Ziola, your influence is definitely present in not only the appearance of this document, but in the spirit of it, too. Numerous friends have provided me with a few necessary "reality-check" over the course of this thesis. Whether it was through a game of shinny, a debate on the finer points of politics and philosophy, or simply some words of encouragement to see this thesis through to its conclusion, each of you has reminded me in your own way of the importance of broadening one's outlook on life. To Rahool Agarwal, Solanna Anderson, Sara Breitkreutz, Dickson Delorme, Neil Delorme, Akash Khokhar, Radek Kwasniewski, Jill Legaarden, Lisa Lemieux, Janine McCready, Kelsey McCready, Candace Rypien, Jai Shah, Adrian and Laura Sherman, Jordan Taft, Zoe Todd, Marika Warren, and Leslie Weigl, thank you all.

To my wife, Tai, your unwavering support, companionship, and love has been the sole influence that got me through the toughest times, especially over the last few most challenging months of this work. You are undeniably the answer to all of the questions of my life .

And, of course, thanks to my cat, Rookie, for her constant reminders that any time is a good time for a nap, and that there is no better place for it than on the keyboard. Without her I would likely have written this thesis twice as quickly … and smiled half as much.

To my darling Tai, who is the light in my life

CONTENTS

CHAPTER 1 Introduction **1**
1.1 Motivation 1
1.2 Scope 3
1.3 Thin films 5
1.3.1 Thin film deposition 5
1.3.2 Oblique angle deposition 8
1.3.3 Glancing angle deposition (GLAD) 13
1.3.4 Film imperfections common to GLAD 18
1.3.5 Applications of GLAD 21
References 24

CHAPTER 2 Background – chiral optics and luminescence **30**
2.1 Chiral optics 30
2.1.1 Polarized light 31
2.1.2 Circular birefringence and circular dichroism 36
2.1.3 Circular Bragg phenomena 37
2.2 Luminescence 40
2.2.1 Inorganic luminescence 41
2.2.2 Organic Luminescence 53
2.2.3 tris (8-hydroxyquinoline) aluminum (Alq_3) 54
2.3 Summary 57
References 57

CHAPTER 3 Fabrication and preliminary characterization of nanostructured Y_2O_3: Eu thin films **62**
3.1 Fabrication 62
3.2 Photoluminescence Detection Apparatus 67
3.3 Post-deposition annealing 71
3.4 Effect of the europium content of the source material 80
3.5 Effect of oxygen background during deposition 83
3.6 Summary 85
References 87

CHAPTER 4 Optical characterization of nanostructured Y_2O_3:Eu thin films 90
4.1 Optical characterization methods 91
4.1.1 Variable-angle spectroscopic ellipsometry 91
4.1.2 Transmittance-mode Mueller matrix ellipsometry 94
4.1.3 Stokes polarimetry 96
4.2 Determination of the optical constants of nanostructured Y_2O_3:Eu thin films 98
4.3 Polarized photoluminescence from nanostructured Y_2O_3:Eu thin films 109
4.4 Summary 115
References 116

CHAPTER 5 Fabrication and structural characterization of nanostructured Alq_3 thin films 120
5.1 Fabrication 121
5.2 Controlling the wetting layer thickness 130
5.3 Column geometry of nanostructured Alq_3 films 135
5.4 Variation of film porosity and column tilt angle with deposition angle 139
5.5 Summary 144
References 146

CHAPTER 6 Optical characterization of nanostructured Alq_3 thin films 149
6.1 Optical characterization methods 149
6.1.1 Variable angle spectroscopic ellipsometry 150
6.1.2 Transmittance-mode spectroscopic ellipsometry 151
6.1.3 Stokes polarimetry 151
6.2 Principal indices of refraction of tilted columnar Alq_3 thin films 154
6.3 Degree of polarization of photoluminescent output from tilted columnar Alq_3 thin films 161
6.4 Variation of circular Bragg phenomena with deposition angle in chiral Alq_3 thin films 164
6.5 Strong circular Bragg phenomena in thick chiral Alq_3 films 168
6.6 Potential for fabrication of enhanced spontaneous emission and low-threshold lasers using chiral Alq_3 films 179
6.7 Summary 184
References 185

CHAPTER 7 Summary and conclusions **189**
7.1 Summary 189
7.2 Suggested future research 192

APPENDIX A Thin film density and z-factor calibration method **194**
A.1 Thin Film Density Calibration 194
A.2 Z-factor Calibration 195
A.3 Results 196
References 196

APPENDIX B Polarized photoluminescence data for Y_2O_3:Eu: an example **197**

APPENDIX C Stokes parameter measurements of Alq_3 films **199**

List of Tables

Table 3.1 Determination of chemical composition of Y_2O_3:Eu films using XPS.....79

Table 4.1 Tilted Columnar Y_2O_3:Eu films fabricated for characterizing the optical constants. 99

Table 4.2 Chevronic and Chiral Y_2O_3:Eu films fabricated for polarized photoluminescence studies. 109

Table 4.3 Polarized photoluminescence data obtained chevronic and chiral Y_2O_3:Eu films. 111

Table 6.1 Tilted columnar Alq_3 films fabricated at various deposition angles. 155

Table 6.2 Chiral Alq_3 films fabricated at various deposition angles.....164

Table 6.3 Chiral Alq_3 films fabricated with various numbers of turns. 169

Table 6.4 Comparison between chiral optical properties of various chiral media. ..179

List of Figures

Figure 1.1 Normal incidence PVD film growth 8

Figure 1.2 Oblique angle PVD film growth. 10

Figure 1.3 Self-shadowing effects in PVD film growth. 11

Figure 1.4 SEM micrographs of tilted columnar thin films. 12

Figure 1.5 GLAD deposition apparatus. 14

Figure 1.6 SEM micrographs of GLAD films.. 15

Figure 1.7 SEM micrographs of Si square spiral. 17

Figure 1.8 Wedging effect in oblique angle deposition. 19

Figure 1.9 SEM micrograph of TiO_2 helices. 20

Figure 2.1 Elliptical polarization. 33

Figure 2.2 Linear polarization. 34

Figure 2.3 Circular polarization. 35

Figure 2.4 Band gap luminescence. 42

Figure 2.5 Generalized configurational coordinate diagram. 47

Figure 2.6 Y_2O_3 crystallographic symmetries. 50

Figure 2.7 Configurational coordinate diagram for Y_2O_3:Eu. 52

Figure 2.8 Photoluminescence spectrum of Y_2O_3:Eu. 52

Figure 2.9 Energy level diagram of molecular orbitals. 54

Figure 2.10 Chemical structure of tris-(8-hydroxyquinoline) aluminum (Alq_3).....56

Figure 2.11 Photoluminescence spectrum of Alq_3 56

Figure 3.1 Deposition apparatus.. 66

Figure 3.2 Schematic diagram of the photoluminescence detection apparatus. 68

Figure 3.3 Typical photoluminescence data.....70

Figure 3.4 SEM images of a tilted columnar Y_2O_3:Eu thin film.....72

Figure 3.5 Photoluminescent spectra as-deposited and annealed samples. 72

Figure 3.6 SEM images of a pillar film annealed at various temperatures. 74

Figure 3.7 SEM images of a chiral film annealed at various temperatures. 75

Figure 3.8 XRD patterns of a chiral Y_2O_3:Eu thin film before and after annealing.....77

Figure 3.9 Comparison of XRD data and SEM micrographs for Y_2O_3:Eu thin films with differing nanostructural morphologies. 78

Figure 3.10 SEM images of tilted columnar Y_2O_3:Eu thin films fabricated from different source materials.....82

Figure 3.11 Photoluminescent spectra of samples fabricated from different source materials.....82

Figure 3.12 SEM images of tilted columnar Y_2O_3:Eu thin films fabricated under differing vacuum conditions. 84

Figure 3.13 Effect of deposition pressure on the photoluminescence efficiency.....85

Figure 4.1 Principal indices of refraction of tilted columnar thin films.....92

Figure 4.2 Schematic diagram of the photoluminescence and Stokes polarimeter apparatus.. 97

Figure 4.3 Optical layer model of a solid Y_2O_3:Eu film. 101

Figure 4.4 Dispersion of the index of refraction of a solid Y_2O_3:Eu film.. 101

Figure 4.5 Optical layer model of a tilted columnar Y_2O_3:Eu film. 103

Figure 4.6 Variation of the column tilt angle of tilted columnar Y_2O_3:Eu thin films with deposition angle. 103

Figure 4.7 Variation of the porosity of tilted columnar Y_2O_3:Eu thin films with deposition angle. 104

Figure 4.8 Principal indices of refraction of tilted columnar Y_2O_3:Eu films. 105

Figure 4.9 Variation of the principal indices of refraction of tilted columnar Y_2O_3:Eu thin films with deposition angle. 106

Figure 4.10 Principal refractive index differences and normal incidence birefringence of tilted columnar Y_2O_3:Eu thin films. 108

Figure 4.11 Spectral variation of selective transmittance of LCP versus RCP light through chiral Y_2O_3:Eu films. 110

Figure 4.12 Selective transmittance of LCP versus RCP light and photoluminescence spectra of a chiral Y_2O_3:Eu film. 112

Figure 4.13 Comparison of degree of circular polarization of photoluminescent emission and selective transmittance of circularly polarized light for chiral Y_2O_3:Eu films. 114

Figure 5.1 Organic film deposition apparatus. 123

Figure 5.2 SEM micrographs of various Alq_3 films. 125

Figure 5.3 SEM micrographs and 2D FFT of SEM micrographs of organic and inorganic GLAD films. 129

Figure 5.4 Effect of surface treatments on the formation of the wetting layer. 131

Figure 5.5 SEM micrographs of chiral Alq_3 films 133

Figure 5.6 Effect of deposition angle on wetting layer thickness. 134

Figure 5.7 Square spiral Alq_3 film on a tetragonal array of seeds. 135

Figure 5.8 Effect of deposition angle on column diameter in Alq_3 helices. 136

Figure 5.9 SEM micrograph of a helical Alq_3 film and its 2D-FFT image. 137

Figure 5.10 Effect of deposition angle on inter-columnar spacing in helical Alq_3 films. 138

Figure 5.11 Effect of numbers of turns on inter-columnar spacing in helical Alq_3 films. 138

Figure 5.12 Optical model of solid Alq_3 film. 141

Figure 5.13 Optical model of a tilted columnar Alq_3 film.a 142

Figure 5.14 Effect of deposition angle on column tilt angle in tilted columnar Alq_3 films. 143

Figure 5.15 Effect of deposition angle on porosity in tilted columnar Alq_3 films. 144

Figure 6.1 Schematic diagram of a tilted columnar thin films fabricated using GLAD 151

Figure 6.2 Laser damage in nanostructured Alq_3 films. 152

Figure 6.3 Schematic diagram of the photoluminescence detection and Stokes polarimetry apparatus. 153

Figure 6.4 Dispersion of the principal refractive indices of tilted columnar Alq_3 films. 156

Figure 6.5 Variation of the principal indices of refraction of tilted columnar Alq_3 thin films with deposition angle. 158

Figure 6.6 Variation of the birefringence of tilted columnar Alq_3 thin films with deposition angle at a wavelength of 525 nm. 158

Figure 6.7 SEM micrographs of the column cross-sections of inorganic and organic tilted columnar thin films. 160

Figure 6.8 Schematic representation of the source of the normal incidence birefringence of tilted columnar Alq_3 thin films. 160

Figure 6.9 Spectral variation of (a) Stokes parameters and (b) degree of polarization for sample G. 162

Figure 6.10 Variation of the magnitude of the normal incidence birefringence at $\lambda = 525$ nm and maximum overall degree of polarization of tilted columnar Alq_3 thin films with deposition angle. 163

Figure 6.11 Dependence of circular Bragg effect strength and location upon film deposition angle.

Figure 6.12 Evidence of increased scattering in chiral Alq_3 films deposited at higher angles of incidence.. 167

Figure 6.13 Circular Bragg phenomena in a 10.5-turn chiral Alq_3 sample. 171

Figure 6.14 Circular Bragg phenomena in a 19-turn chiral Alq_3 sample. 172

Figure 6.15 Circular Bragg phenomena in a 40-turn chiral Alq_3 sample.. 173

Figure 6.16 SEM image of surface damage that occurred during film deposition. 175

Figure 6.17 Measured Stokes parameters for various chiral Alq_3 films. 176

Figure 6.18 Variation of the maximum selective transmittance of circularly polarized light and degree of circular polarization with the number of turn. 177

Figure 6.19 Optical defects in chiral Alq_3 films. 183

CHAPTER 1
Introduction

1.1 Motivation

The processing and generation of polarized light is a key ingredient to display and optical information processing technologies. Switchable polarization devices have become a mature technology integrated into products such as liquid crystal displays (LCDs). However, these use unpolarized light sources leading to decreased overall efficiency for the devices. In the last ten years research has begun to focus heavily on the aim of achieving active devices that emit polarized light [1, 2]. Circularly polarized light emitters are potentially applicable to emissive flat panel displays [3], image projection displays [2, 4], stereoscopic displays [2, 5], and mirrorless low-threshold lasing devices [6]. Thus far, attempts to form circularly polarized light emitters for such applications have focused on the formation of cholesteric liquid crystal (LC) films doped with dyes or other luminescent molecules [2, 6 – 10] . These films make use of the structural anisotropy of the LCs, as well as their chiral orientation, which periodically repeats on a similar scale to the wavelength of visible light, to achieve circularly polarized emission. As an alternative to such LC films, recent theoretical studies [6, 11 – 13] have proposed the use of luminescent chiral thin films fabricated using the glancing angle deposition (GLAD) technique [14 – 19] to form circularly polarized light emitters.

Since the first studies of vacuum-deposited chiral thin films by Young and Kowal [20], onward through the formalization of the modern technique of GLAD [14 – 19], the polarization-sensitive optical properties exhibited by the unique nanostrucured films yielded by the GLAD technique have been of primary interest. Numerous photonic applications of nanostructured thin films fabricated by GLAD have been explored. These include polarization optics [14, 15], three-dimensional (3D) photonic bandgap material applications [21 – 23], interference filters [24 – 26], wide band antireflection coatings [27], and high index contrast Bragg stacks [28]. Prior to the work discussed herein, only the aforementioned theoretical treatments of nanostructured luminescent chiral thin films had been developed, leaving the opportunity of realizing the fabrication and optical characterization of nanostructured luminescent chiral thin films yet to be studied.

As will be demonstrated within this thesis, photoluminescent chiral thin films can be fabricated by GLAD using either inorganic or organic luminescent source materials. When such films are properly designed, the photoluminescent emission exhibits a degree of circular polarization, the strength of which depends upon the number of turns of the chiral structure present in the films. Strong levels of circular polarized photoluminescence were achieved with organic chiral thin films, yielding samples that showed excellent potential to be developed further into devices such as mirrorless low-threshold lasers [6,7], tunable lasers [29] or sensors [30].

1.2 Scope

This thesis starts with a brief outline of traditional thin film deposition methods and the development of the GLAD method. This discussion of the GLAD technique comprises the remainder of this chapter. The fundamentals of thin film growth, and the mechanisms that enables the creation of nanostructured thin films using GLAD are reviewed. Also, a few of the numerous morphologies of nanostructured films that can be fabricated using GLAD and some of the emerging applications of films produced using this technique are presented.

Additional background and introductory information relevant to the research discussed in this thesis is provided in *Chapter 2*. This includes a discussion of the polarization-sensitive optical properties of chiral thin films, and an introduction to luminescent materials. Specific emphasis is placed upon the photoluminescence mechanisms of the materials used for the experiments in this thesis, europium-doped yttrium oxide (Y_2O_3:Eu) and tris-(8-hydroxyquinoline) aluminum (Alq_3).

Chapter 3 presents the initial work conducted on the fabrication of nanostructured Y_2O_3:Eu films and on measuring the photoluminescence from such films. The aim of this initial work was to observe the effects that variations in the fabrication process had upon the luminescent output of the films. Thus, an acceptable fabrication process for producing nanostructured Y_2O_3:Eu films with easily detectable levels of photoluminescence was established.

Additional work on the optical properties of nanostructured Y_2O_3:Eu films is presented in *Chapter 4*. This work included the determination of the principal indices of refraction of such films, as well as the observation of partially circularly polarized photoluminescence from chiral Y_2O_3:Eu films. This work allows one to design and

fabricate nanostructured luminescent thin films with GLAD with some level of control over the polarization state of the emitted light. This fulfills the fundamental aim of this thesis to provide the first experimental characterization of circularly polarized emission from chiral thin films fabricated by GLAD.

Chapter 5 then introduces the ground-breaking work conducted as part of this thesis on the direct deposition of organic nanostructured thin films of Alq_3 by GLAD. These experiments produced the first ever directly deposited porous organic nanostructured thin films. Initial observations of the nanostructural morphologies of these films are presented. These films exhibited remarkably smooth and uniform nanostructures, which formed in a nearly hexagonal close-packed array for chiral Alq_3 films. A growth mechanism is proposed in light of these observations.

The optical properties of nanostructured Alq_3 thin films are explored in *Chapter 6*. First, tilted columnar Alq_3 thin films were considered. Such films were shown to exhibit form birefringence that increases with the deposition angle used to fabricate the films. This trend was used to design and fabricate chiral Alq_3 films. The polarization-sensitive optical properties of the chiral Alq_3 films were characterized, culminating in the study of thick chiral Alq_3 films with strong chiral optical properties for both transmitted light and the photoluminescent light emission of the films. The circularly polarized photoluminescence produced by these films had an order of magnitude larger degree of circular polarization than observed for the chiral Y_2O_3:Eu films.

Lastly, *Chapter 7* summarizes the main conclusions of the work presented in this thesis and outlines a few proposals for future experiments.

1.3 Thin films

Thin films are ubiquitous, finding applications in such diverse fields as protective coatings for tools and mechanical parts, magnetic storage media, food packaging, sensors, microelectronics, and optical coatings. The size and composition of the coatings used varies widely depending on the intended application of the thin film. However, all thin films coat a substrate, such that the thickness of the coating is substantially smaller than that of the substrate. Depending on the applications, coatings as thin as tens of nanometers or thicker than tens of micrometers may be used.

1.3.1 Thin film deposition

Thin films can be formed by a wide range of techniques including solution-based methods such as spin coating or dip coating, and vacuum-based deposition methods. Only vacuum-based deposition methods, and of vacuum-based methods, only physical vapor deposition (PVD) methods will be discussed here, as these are the methods traditionally used in conjunction with GLAD. PVD methods, which involve the condensation of a vapor flux generated through physical means onto a substrate, are some of the oldest film deposition methods, dating back to experiments by Faraday in 1857 [31]. The most common modern PVD techniques are evaporation (or sublimation), and sputtering [32 – 35]. In evaporation, a source material is heated, either through resistive means (thermal evaporation) or with an electron beam (e-beam evaporation), to temperatures high enough to cause the vapor pressure of the source to be significantly higher than that of the surrounding vacuum. Alternatively, sputtering generates a vapor flux through momentum transfer between the ions of a plasma and a target of source material by accelerating the ions toward the target with an electric field.

Solid thin film growth usually occurs through nucleation, growth, and coalescence stages which involve such physical processes as adsorption and diffusion. Only a brief overview of the relationship between these stages will be given here -- interested readers are referred to [36 - 39]. Nucleation involves the clustering of adatoms that have adsorbed to the substrate. These clusters are called nuclei, and they are only stable over a certain critical size. Additional adatoms can join such stable nuclei and cause them to grow, eventually resulting in the coalescence of neighboring nuclei and the formation of a solid film. Coarsening phenomena, which involve the growth of larger clusters at the expense of smaller ones, often also plays a significant role in the formation and morphology of thin films [38]. Most commonly, coarsening phenomena consist of Ostwald ripening where the Gibbs-Thomson effect provides a long-range thermodynamic driving force for large clusters to grow at the expense of smaller ones. In scenarios where there is insufficient saturation vapor flux to enable the Gibbs-Thomson effect a process called direct ripening can occur instead [39]. Direct ripening involves two nearby clusters merging and is purely a short-range effect. This process has been demonstrated to have some bearing on the growth of amorphous organic thin films [40, 41].

Both evaporation and sputtering are performed in vacuum chambers evacuated to high vacuum conditions ($< 10^{-5}$ Torr). Such low pressures reduce contamination by ambient species present in the vacuum chamber, because the monolayer formation time for such species is inversely dependent upon the pressure [42]. Evaporation is often performed at pressures near the base pressure, however, a flow of high purity gas is required in sputtering to form the plasma. Thus, deposition pressures for sputtering processes are higher than for evaporation processes. Because the mean free path of the vapor flux produced is also inversely dependent upon the vacuum pressure [42], it is lower in sputtering processes than it in evaporation. Accordingly, evaporated vapor flux

tends to travel to the substrate without undergoing any collisions, while sputtered vapor flux undergoes a number of collisions prior to reaching the substrate. This means that the evaporated vapor flux arriving at the substrate has little angular distribution when the substrate is held sufficiently far from the source: thus, evaporated vapor flux is assumed to be collimated, when viewed from the substrate. The shorter mean free path of sputtered vapor flux means gives rise to a wider angular distribution of vapor flux at the substrate, such that sputtered vapor flux cannot strictly be considered collimated. The physical mechanism behind sputtering also leads to more energetic impinging vapor flux than for evaporation.

The different flux distributions incident at the substrate for, and energetics of, evaporation and sputtering give rise to slightly different film morphologies. This is evident from the different structure zone models proposed for evaporated films and sputtered films [43 – 46], which describe how the film morphology varies with certain deposition parameters, such as substrate temperature and deposition pressure. These models provide insights into the key processes that define the resultant film morphology: desorption, bulk diffusion, surface diffusion and self-shadowing [33]. Desorption and both types of diffusion are thermal processes, while self-shadowing is a geometric effect arising from the line-of-sight impingement of the vapor flux. At substrate temperatures nearing the source material melting point, diffusion processes dominate the film growth. Thus, adatoms migrate over the substrate until reaching positions that minimize their potential energy, sometimes leading to crystallization. Substrate temperatures lower than approximately one-third of the source material melting point allow self-shadowing effects to play a significant role, leading to a dense, columnar morphology, akin to that depicted in Fig. 1.1.

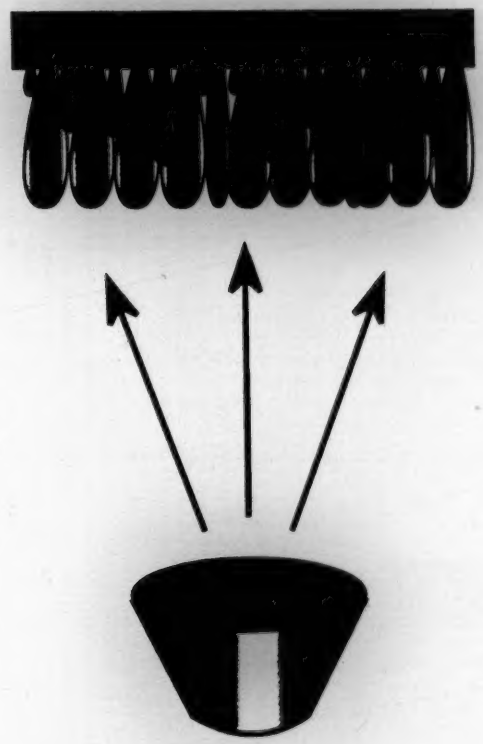

FIGURE 1.1

Normal incidence PVD film growth. At low substrate temperatures, self-shadowing effects contribute to the formation of a dense columnar film morphology.

1.3.2 Oblique angle deposition

Because traditional thin film growth focuses upon dense, solid thin films, effort is usually invested in reducing the effects of self-shadowing and enhancing the role of the thermal processes through the use of substrate heating during deposition. From the mid-20th century onward, researchers have increasingly explored the potential offered by films fabricated under conditions that enhance the role of self-shadowing in film growth. Most early investigations focused on enhancing self-shadowing through oblique

deposition at angles of incidence, $\alpha \leq 70°$, where α is the deposition angle as measured from the substrate normal [20, 47 – 49]. In oblique angle deposition, geometric self-shadowing and adatom diffusion (a temperature- and material-dependent parameter) are the dominant processes influencing the film morphology. These two effects oppose each other, however, as self-shadowing leads to voids in the resultant films, while adatom diffusion works to fill in these voids. This produces films composed of columns tilted at an angle, β, relative to the substrate normal. The geometric self-shadowing effect increases with deposition angle, though, leading Robbie *et al.* to explore the prospects of deposition at even more oblique angles, $\alpha \geq 80°$, the so-called glancing angles [50]. For certain deposition parameters (material, temperature, vapor flux energy, and deposition pressure) and at sufficiently high deposition angles, though, the effects of self-shadowing can dominate the effects of adatom diffusion, resulting in a porous tilted columnar film (Fig. 1.2).

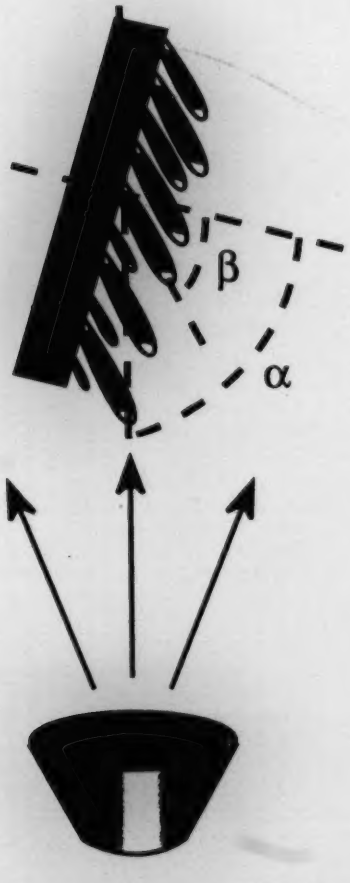

FIGURE 1.2
Oblique angle PVD film growth. At low substrate temperatures and oblique angles of incidence, self-shadowing effects dominate, producing a porous tilted columnar film morphology.

In the early growth stages, nuclei forming on the surface of the substrate shadow regions of the substrate from the source, encouraging continued growth at the nuclei themselves (Fig. 1.3a). As the deposition continues, self-shadowing is maintained such that only the top edges of the tallest structures intercept the vapor flux (Fig. 1.3b). Thus, a porous film composed of isolated, tilted columns, as demonstrated by the scanning electron microscopy (SEM) images shown in Fig. 1.4. These obliquely deposited films

are biaxial. This means the films have three principal axes: one along the length of the columns, and within the deposition plane; one within the deposition plane, but perpendicular to the columns; and one parallel to the substrate, but perpendicular to the deposition plane [51, 52]. This last axis is visible in Fig. 1.4b which depicts the structures fanning out along this axis because the self-shadowing effect only occurs within the deposition plane.

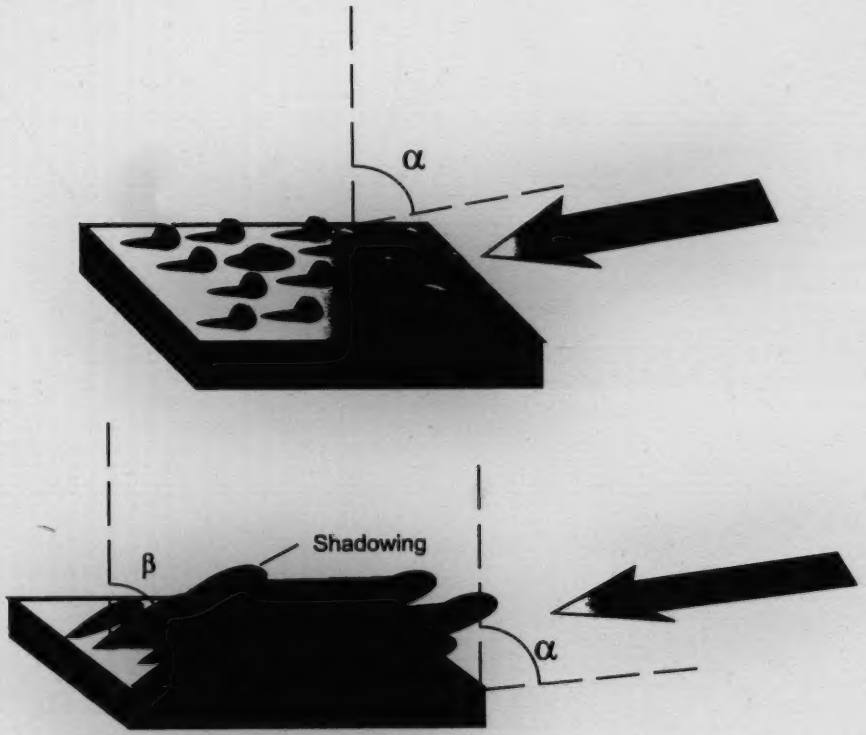

FIGURE 1.3

Self-shadowing effects in PVD film growth. (a) In the early stages of growth, nuclei form and shadow some regions of the substrate from the incident flux. Continued growth preferentially occurs at the nuclei, leading to (b) a porous morphology in which structures are inclined towards the source of the vapor flux. Here, continued growth preferentially occurs at the tallest structures, which shadow shorter structures.

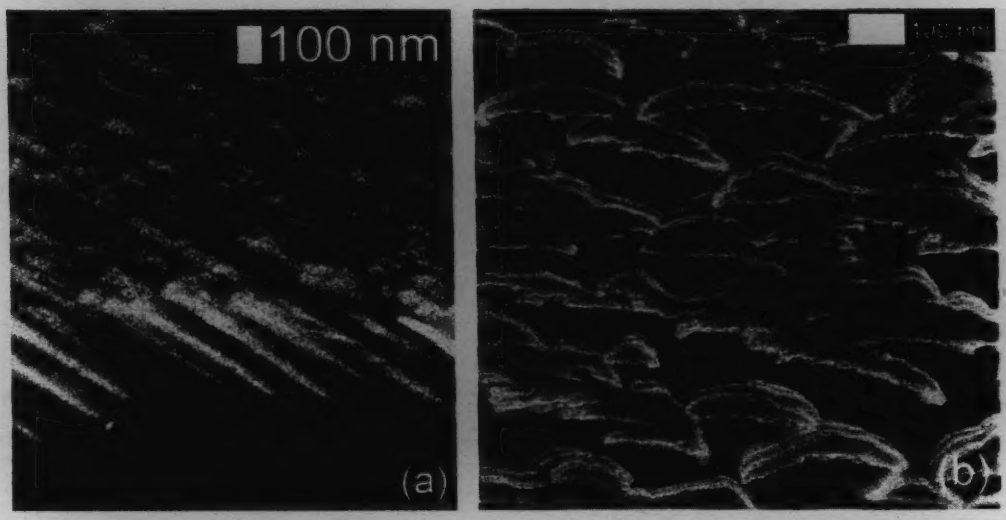

FIGURE 1.4

SEM micrographs of tilted columnar thin films. (a) A tilted columnar thin film of Y_2O_3:Eu film (section view) and (b) a tilted columnar thin film of TiO_2 film (plan view) are depicted. Note that the self-shadowing effect is only present in the deposition plane resulting in tilted columns with fan-shaped cross-sections. Image (b) courtesy A. C. van Popta.

The tilted columns of obliquely deposited films grow at a column tilt angle (measured from the substrate normal), β, that is inclined towards the vapor source, but is less than the deposition angle, α. A number of attempts have been made to formalize the relationship between the two angles, including the empirical tangent rule [53]

$$\tan\beta = \frac{1}{2}\tan\alpha \tag{1.1}$$

or Tait's rule [54]

$$\beta = \alpha - \arcsin\left[\frac{1}{2}(1-\cos\alpha)\right] \tag{1.2}$$

the latter having been generated through geometric analysis of oblique angle deposition. Neither of these expressions provides an excellent fit to all experimental data. The tangent rule gives inaccurate predictions of the column tilt angle for deposition angles greater than 50°, because it allows β to vary freely all the way to 90° without reaching some asymptotic value at sufficiently high values of α. Tait's rule, on the other hand, tends to be less accurate for lower deposition angles. Ultimately, neither of these expressions relating α and β are capable of providing accurate results for all tilted columnar thin films, because neither takes into account any spurious effects introduced by the film material or deposition conditions. Other relationships that attempt to account for material parameters through the inclusion of diffusion length terms have also been employed in the study of obliquely deposited films, with varying degrees of success [55. 56]. When used judiciously, though, these equations can prove useful in designing the film structure of obliquely deposited films for use in specific applications.

1.3.3 Glancing angle deposition (GLAD)

Typically, GLAD involves deposition at $\alpha \geq 80°$, for which isolated nanostructures form. The tilted columnar thin films that result from oblique angle deposition are the simplest morphology of thin film that can be formed by GLAD. The true advantage of GLAD is the use of computer-controlled motion of both the substrate rotation and deposition angle throughout the deposition. This is because the growing nanostructures tend to track the direction of the incoming vapor flux. Thus, the deposition angle can be varied to control the porosity of the film, while the substrate rotation is independently varied to control the morphology of the film.

The apparatus used to achieve such motions incorporates two independent computer-controlled stepper motors (Fig. 1.5), with the stepping rates of the motors tied to deposition rate feedback provided by a quartz crystal microbalance (QCM). Complex geometries such as helices, chevrons, vertical pillars, polygonal spirals, and many others can be formed (Fig. 1.6) with appropriate substrate motions. The precise rotational control offered by the computer-controlled stepper motors enables the nanometer-scale engineering of the deposited films structures.

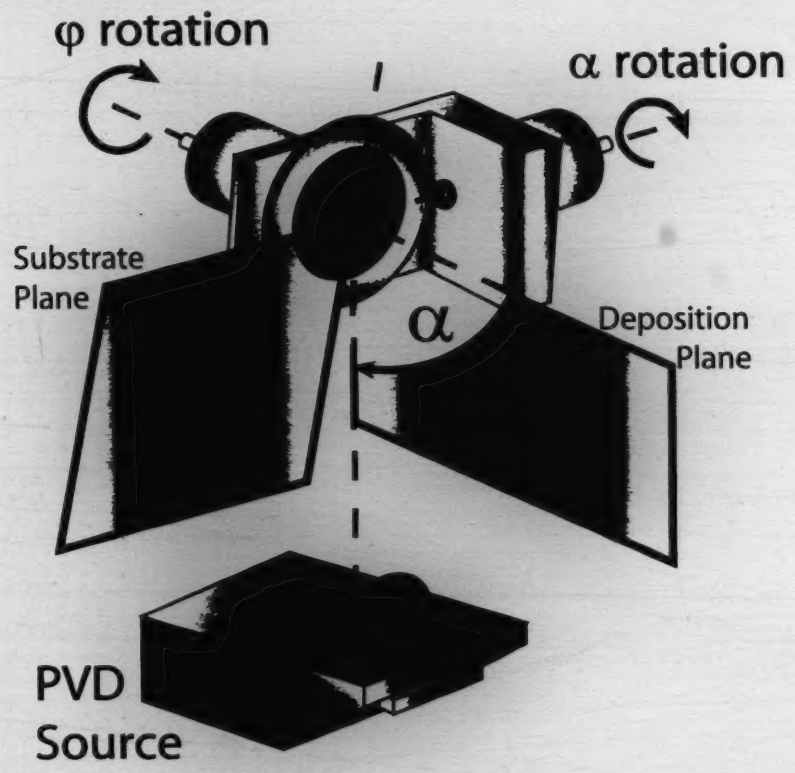

FIGURE 1.5

GLAD deposition apparatus. Note the location of the substrate plane and the deposition plane, which are perpendicular to each other. An e-beam gun is depicted as the PVD source used, an arrangement that is commonly used for GLAD film fabrication.

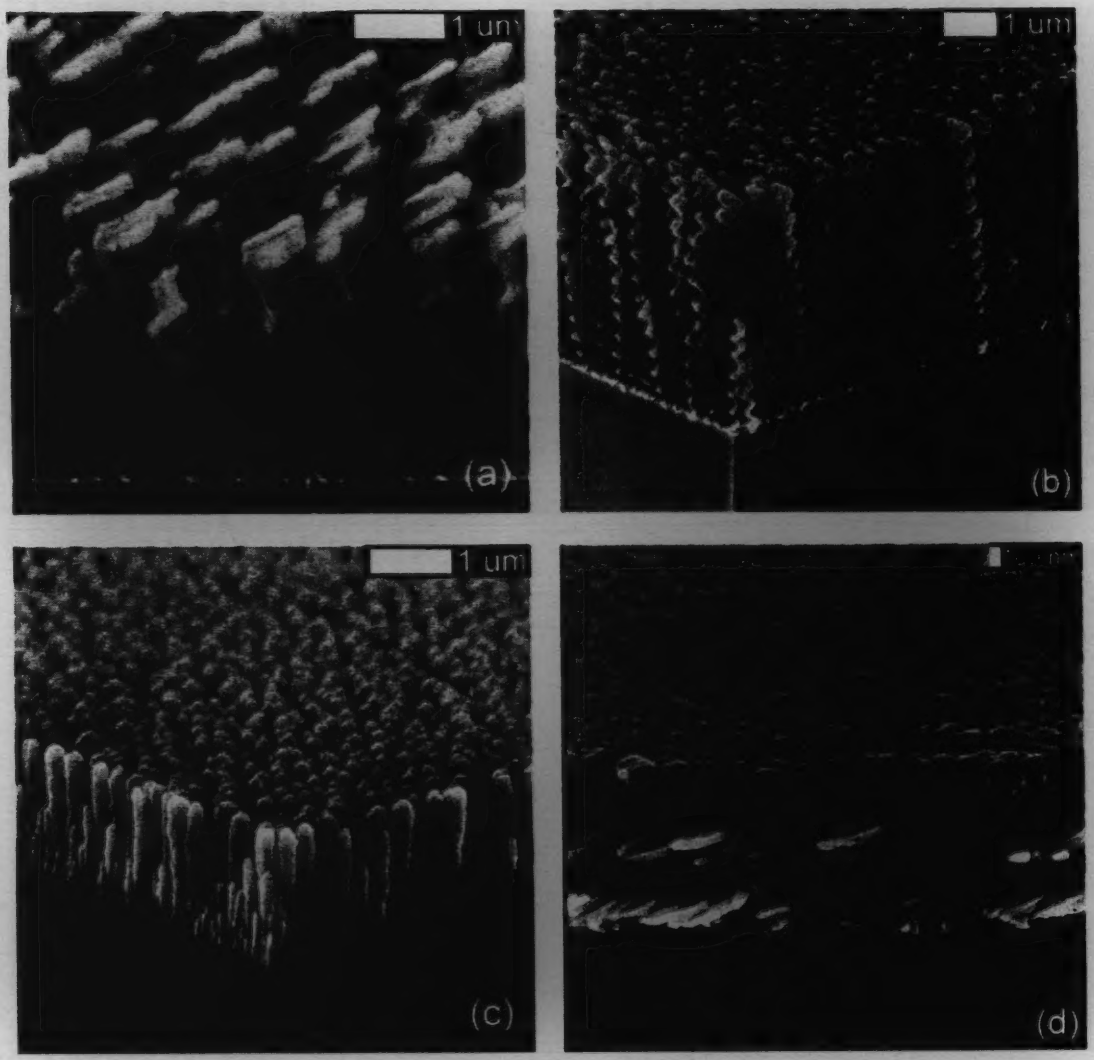

FIGURE 1.6

SEM micrographs of GLAD films. Morphologies such as (a) chevronic, (b) helical, (c) pillar, and (d) capped helical are readily fabricated using GLAD. Images courtesy (a) K. D. Harris, (b, c) J. C. Sit, and (d) B. Szeto.

The chevronic structure depicted in Fig. 1.6a is achieved by periodically and discretely rotating the substrate by 180° to effectively flip the direction of the incoming vapor source. Helical (Fig. 1.6b) and vertical pillar (Fig. 1.6c) structures are produced by continuous substrate rotation with the substrate rotation rate, ω_{sub}, varied to maintain a constant ratio, p, with the deposition rate, r. This ratio, $p = r/\omega_{sub}$, is the pitch of the structure, or the film thickness required to complete one period of a nanostructure that is periodic with increasing thickness. Thus, pillar structures are essentially helices for which the pitch is less than the diameter of the nanostructure, and can typically be produced with 5 nm < p < 25 nm, while helical structures are achieved with p > 30 nm. The capped helices depicted in Fig 1.6d are produced through similar means, however, the deposition angle is exponentially decreased in the latter stages of the deposition. This gradually reduce the porosity of the film until a solid capping layer is produced. Many more unique and intriguing morphologies can be attained through variations or combinations of those outlined here.

Normally the nanostructures that compose these GLAD films are simply arrayed randomly upon the substrate at whatever locations nucleation occurs during the initial growth stages. Randomly arrayed nuclei formed during the initial growth stages continue to receive more of the incoming flux than shadowed regions of the substrate as the deposition progresses owing to the self-shadowing effect. Methods to fabricate highly ordered, periodic arrays of nanostructures via GLAD have been developed, though [57–60]. These methods use lithographically defined topographical arrays, usually called seeds, applied to the substrates prior to film deposition. These seeds act as the nucleation centers for initial stages of film growth. If the seed array is designed correctly for the porosity and morphology of the film [60], a periodic array of nanostructures will result

(Fig 1.7a). Furthermore, defects in the periodicity seed array can be used to introduce defects in the periodicity of the resulting film (Fig. 1.7b). These techniques are vital to one of the key photonic applications of GLAD films, photonic band gap materials [21 – 23].

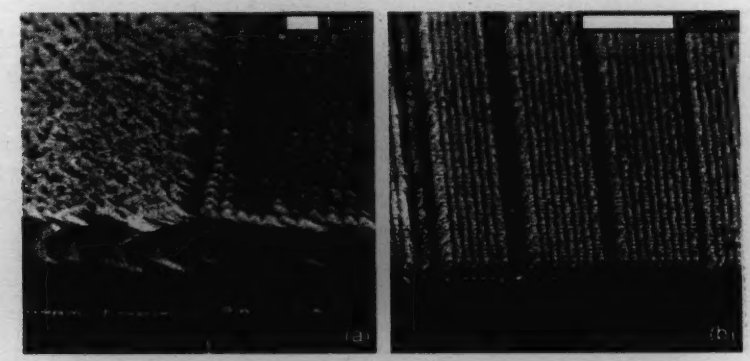

FIGURE 1.7

SEM micrographs of Si square spiral. (a) A tetragonal array of Si square spirals deposited on a lithographically patterned array of seeds and (b) a tetragonal array of Si square spirals with a linear defect in the seed array are shown. Images courtesy M. O. Jensen.

GLAD is compatible with many materials that can be deposited by PVD methods, provided that the process parameters ensure that self-shadowing is the dominant mechanism in the early film growth. Inorganic materials such as silicon, silicon dioxide, aluminum, aluminum oxide, titanium, titanium dioxide, and magnesium fluoride are but a few of the materials that have been used to fabricate nanostructured thin films with GLAD. These have been fabricated using thermal evaporation [14], e-beam evaporation [14], sputtering [61], and pulsed laser deposition (PLD) [62]. However, the higher angular distribution of the flux arriving at the substrate and the higher energy of the impinging flux in sputtering and PLD processes often lead to less well-defined nanostructures [63].

As a result, evaporation tends to be the preferred deposition method used with GLAD. Recently, the vacuum sublimation of organics [64] and spray pyrolysis of polymers [65] has also been successfully used with GLAD to produce novel nanostructured organic thin films. This has enabled the fabrication of nanostructured films of materials such as tris (8-hydroxyquinoline) aluminum (Alq_3) and parylene.

1.3.4 Film imperfections common to GLAD

Nanostructured films fabricated with GLAD are commonly subject to a number of imperfections. One of the earliest to be observed was a wedging effect [49]. The wedging effect is a thickness non-uniformity across the substrate that arises in tilted columnar films because of the deposition geometry (Fig. 1.8). Deposition rates for PVD techniques are highly dependent on the throw distance between the source and the substrate [35]; a distance which varies over the substrate in oblique angle deposition. Furthermore, this geometry gives rise to a non-uniform effective deposition angle across the substrate. Examination of section view SEM images that the wedging effect reduces the film thickness uniformity to ~ 70%, where the thickness uniformity is defined by Eq. 1.3.

$$uniformity = \left(1 - \frac{d_{max} - d_{min}}{d_{mean}}\right) \times 100\% \qquad (1.3)$$

Here, d_{max} is the maximum observed film thickness, d_{min} is the minimum observed film thickness, and d_{mean} is the mean observed film thickness. Morphologies produced by continuous substrate rotation are far less susceptible to the wedging effect, because the constant rotation of the substrate averages the variation across substrate, resulting in uniformities that can be > 95%.

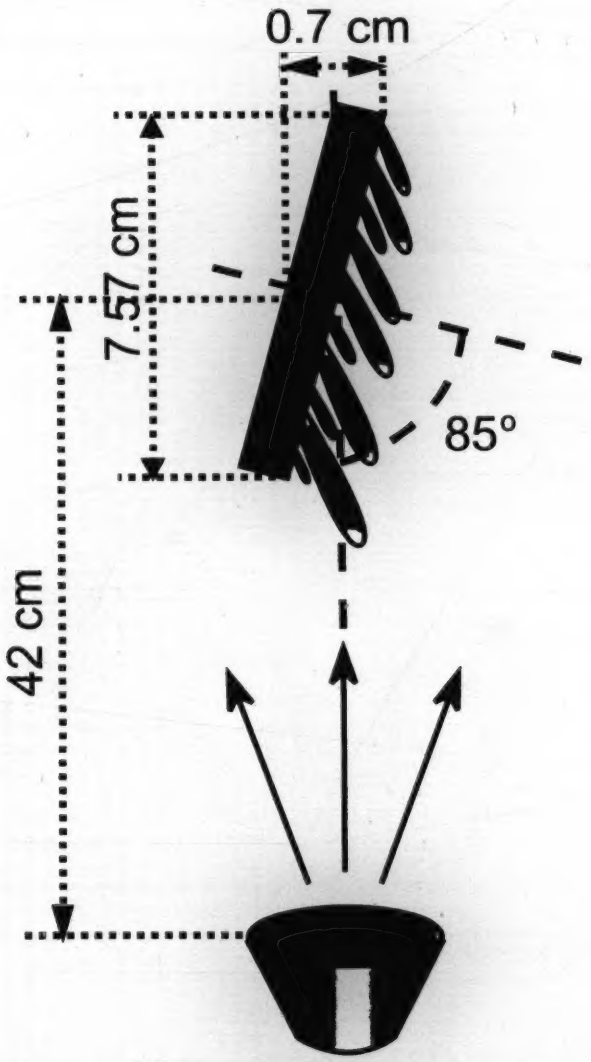

FIGURE 1.8

Wedging effect in oblique angle deposition. The different distances between the source and each point on the substrate lead to a variation in the effective deposition rate over the substrate, and thus to a thickness variation over the substrate. Note that the diagram is not to scale.

Other imperfections arise from the growth mechanisms of GLAD films. These include the fanning of the nanostructures observed in Fig 1.4b, the column competition and extinction visible in Fig. 1.6c, and the nanostructural broadening shown in Fig. 1.9. Fanning is an imperfection that has both positive and negative attributes. On the positive side, the structural anisotropy introduced by fanning gives rise to form birefringence in GLAD films, a trait that is useful for applications involving polarization optics. This trait, however, is undesirable for some other applications, however, such as photonic band gap materials.

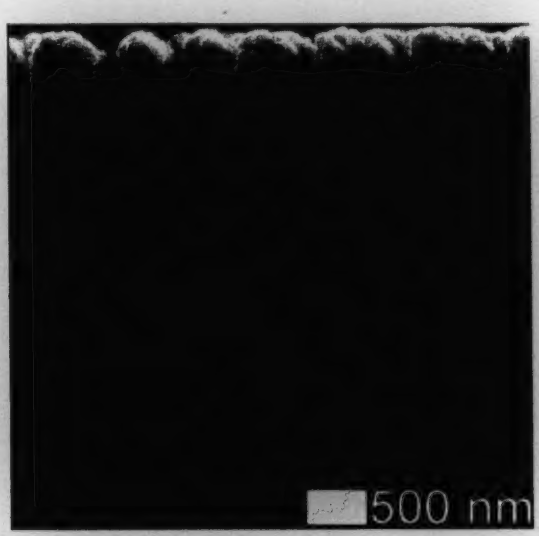

FIGURE 1.9

SEM micrograph of TiO_2 helices. The individual helices can be seen to broaden with increasing thickness. Image courtesy A. C. van Popta.

Column extinction occurs because the tallest structures in a GLAD film tend to intercept more flux and shadow larger regions of the substrate. Thus, other structures will inevitably begin to receive less flux and be shadowed by taller structures [66]. The result is that fewer nanostructures continue to grow the thicker the film gets. Despite

this, the amount of material being deposited at any given time remains the same, and thus the areal density of each slice through the film should be the same. Accordingly, column broadening occurs, because the tallest structures receive more flux and must broaden to accommodate this additional flux [52, 66]. Column extinction can adversely affect optical GLAD films, as it results in a layer of small nanostructures near the substrate that may lead to scattering of some wavelengths of light. Column broadening is also detrimental to optical applications, because the nanostructures gradually lose definition as films grow thicker [67]. For many optical applications, it is desirable to have periodic structures that repeat with increasing thickness with a large number of periods. The loss of structural definition that arises from column broadening inhibits the film designer's ability to produce arbitrarily large numbers of periods to such films.

1.3.5 Applications of GLAD

Porous nanostructured thin films produced by GLAD have garnered interest for many applications owing to the wide range of materials that can be used to make GLAD films, the unique nanoscale porous morphologies, and the high surface areas achievable through GLAD. Photonics applications are thus far among the most commonly studied uses of GLAD films. The original interest in GLAD films for photonic applications was focused upon the circular Bragg phenomena and optical activity exhibited by helical or chiral thin films fabricated by GLAD [14, 15, 20], eventually yielding dense chiral films optimized for use as circular polarization filters [68, 69]. The utility of porous chiral films was enhanced by capitalizing on the high porosity of the films to form hybrid devices through the infiltration of liquid crystals (LCs) [70]. This technique yielded novel devices with electro-optically switchable circular Bragg phenomena [71]. These

studies have also recently been extended to explore the properties of structures infiltrated by mixtures of dichroic dyes and LCs [72].

The ability to continuously vary the porosity during the deposition of GLAD films has yielded gradient index optical thin films, such as interference filters [24 – 26] and wide band antireflection coatings [27]. The effective refractive index of a more porous structure is less than that of the refractive index of a solid material, enabling the fabrication of refractive index gradients over the thickness of the film structure through variation in porosity. Sinusoidal variations in the effective refractive index can be used to form interference filters, called rugate filters, typified by a wide one-dimensional (1D) photonic stop band [24, 25]. The use of appropriately designed defects in such periodic variations of the porosity result in spectral hole filters that exhibit a characteristic narrow band transmittance peaks [26]. Similarly, wide band antireflection coatings are formed by gradually varying the effective refractive index from a value matching the refractive index of the substrate down to a value that matches the refractive index of the surrounding medium [27]. Recently, the low effective refractive indices exhibited by porous films fabricated by GLAD have been used to form high index contrast thin film stacks [28] with enhanced reflectance properties.

Three-dimensional (3D) photonic band gap (PBG) materials consisting of a tetragonal array of square spirals of a high refractive index material, such as Si, are currently one of the most active areas of photonics research involving GLAD structures [21 – 23]. These structures are predicted to exhibit a wide 3D PBG [73]. Experimental evidence that suggests the presence of a full, 3D PBG for tetragonal arrays of Si square spirals has been obtained at infrared wavelengths [21 – 23]. Recent work by Mark Summers, a Ph.D. student with Dr. M. J. Brett, has focused upon forming 3D PBG structures from

alternate materials to produce a 3D photonic stop band at visible wavelengths. Also, efforts to fabricate the inverse structure consisting of a high-index material perforated with low-index square spiral voids through the use of templating procedure [74] are under investigation, because it was predicted to exhibit a wider 3D PBG [73]. The study of defects in 3D PBG materials is also an active area of research, and will ultimately be crucial to yielding useful devices based upon this technology (see Fig. 1.7) [59, 60].

The high surface areas of GLAD films have driven the use of such films in sensing applications. Hydrocarbon sensors based upon nanostructured platinum films fabricated by GLAD have been tested [75]. Similarly, highly sensitive humidity sensors with extremely fast response times, compared to commercially available sensors, have been fabricated using SiO and Al_2O_3 pillar films [76]. These promising results have encouraged the design of new films for applications as sensitive and fast liquid and gas sensors; research that is currently being conducted by J. J. Steele under the supervision of Dr. M. J. Brett. The high surface area of GLAD films has also been used for microfluidics applications [77, 78], and in supercapacitor experiments [79]. Another related application is the use of GLAD to fabricate thermal barrier coatings [80]. These coatings are based upon alternating layers of low and high density – a structure that thermally isolates the substrate from harsh temperature environments.

Post-deposition processing of GLAD films has been used to expand the range of applications for GLAD films by enhancing the functionality of the films. Examples of this include the GLAD-LC hybrids mentioned previously [71], dye-sensitized solar cells [81], and field emitters produced by post-deposition ion-milling of pillar nanostructures [82]. Post-deposition processing has also been used to form novel nanostructured polymeric materials through templating [74], and inversion procedures [83].

References

1. M. Grell and D. D. C. Bradley, "Polarized luminescence from oriented molecular materials", *Advanced Materials* **11** (11), 895 (1999).

2. S. H. Chen, D. Katsis, A. W. Schmid, J. C. Mastrangelo, T. Tsutsui, and T. N. Blanton, "Circularly polarized light generated by photoexcitation of luminophores in glassy liquid-crystal films," *Nature*, **397**, 506 (1999).

3. D. J. Broer, J. Franciscus, J. J. van Tongeren, R. J. Visser, *US Patent Application*, 2005/0179371A1 (2005).

4. I. E. J. R. Heynderickx and D. J. Broer, *US Patent*, 5,626,408 (1997).

5. D. R. Hall, *US Patent*, 5,699,184 (1997).

6. V. I. Kopp, Z.-Q. Zhang, A. Z. Genack, "Lasing in chiral photonic structures," *Progress in quantum electronics*, **27**, 369 (2003).

7. V. I. Kopp, B. Fan, H. K. M. Vithana, and A. Z. Genack, "Low-threshold lasing at the edge of a photonic stop band in cholesteric liquid crystals," *Optics Letters*, **23**, 1707 (1998).

8. H. Finkelmann, S. T. Kim, A. Muñoz, P. Palffy-Muhoray, B. Taheri, "Tunable mirrorless lasing in cholesteric liquid crystalline elastomers," *Advanced Materials*, **13**, 1069 (2001).

9. J. Schmidtke and W. Stille, "Fluorescence of a dye-doped cholesteric liquid crystal film in the region of the stop band: theory and experiment," *The European Physical Journal B*, **31**, 179 (2003).

10. K. L. Woon, M. O'Neill, G. J. Richards, M. P. Aldred, S. M. Kelly, and A. M. Fox, "Highly circularly polarized photoluminescence over a broad spectral range from a calamitic, hole-transporting, chiral nematic glass and from an indirectly excited dye," *Advanced Materials*, **15**, 1555 (2003).

11. A. Lakhtakia, R. Messier, M. J. Brett, and K. Robbie, "Sculptured thin films (STFs) for optical, chemical and biological applications," *Innovations in Materials Research*, **1**, 165 (1996).

12. A. Lakhtakia, "Local inclination angle: a key structural factor in emission from chiral sculptured thin films," *Optics Communications*, **202**, 103 (2002).

13. A. Lakhtakia, "On radiation from canonical source configurations embedded in structurally chiral materials," *Microwave and Optical Technology Letters*, **37**, 37 (2003).

14. K. Robbie, M. J. Brett, and A. Lakhtakia, "First thin film realization of a helicoidal bianisotropic medium," *Journal of Vacuum Science and Technology A*, **13**, 2991 (1995).

15. K. Robbie, M. J. Brett, and A. Lakhtakia, "Chiral sculptured thin films," *Nature*, **384**, 616 (1996).

16. K. Robbie and M. J. Brett, "Sculptured thin films and glancing angle deposition: growth mechanics and applications," *Journal of Vacuum Science and Technology A*, **15**, 1460 (1997).

17. K. Robbie and M. J. Brett, *US Patent*, 5,866,204 (1999).

18. K. Robbie and M. J. Brett, *US Patent*, 6,206,065 (2001).

19. K. Robbie and M. J. Brett, *US Patent*, 6,248,422 (2001).

20. N. O. Young and J. Kowal, "Optically active fluorite films," *Nature*, **183**, 104 (1959).

21. S. R. Kennedy, M. J. Brett, O. Toader, and S. John, "Fabrication of tetragonal square spiral photonic crystals," *Nano Letters*, **2**, 59 (2002).

22. S. R. Kennedy, M. J. Brett, H. Miguez, O. Toader, and S. John, "Optical properties of a three-dimensional silicon square spiral photonic crystal," *Photonics and Nanostructures*, **1**, 37 (2003).

23. M. O. Jensen and M. J. Brett, "Square spiral 3D photonic bandgap crystals at telecommunications frequencies," *Optics Express*, **13**, 3348 (2005).

24. K. Robbie, A. J. P. Hnatiw, M. J. Brett, R. I. MacDonald and J. N. McMullin, "Inhomogeneous thin film optical filters fabricated using glancing angle deposition," *Electronics Letters*, **33**, 1213 (1997).

25. K. Kaminska, T. Brown, G. Beydaghyan, and K. Robbie, "Vacuum evaporated porous silicon photonic interference filters," *Applied Optics*, **42**, 4212 (2003).

26. A. C. van Popta, M. M. Hawkeye, J. C. Sit and M. J. Brett, "Gradient-index narrow-bandpass filter fabricated with glancing-angle deposition," *Optics Letters*, **29**, 2545 (2004).

27. S. R. Kennedy and M. J. Brett, "Porous broadband antireflection coating by glancing angle deposition," *Applied Optics*, **42**, 4573 (2003).

28. J.-Q. Xi, J. K. Kim, and E. F. Schubert, "Silica nanorod-array films with very low refractive indices," *Nano Letters*, **5**, 1385 (2005).

29. F. Wang, A. Lakhtakia, and R. Messier, "Towards piezoelectrically tunable chiral sculptured thin film lasers," *Sensors and Actuators A*, **102**, 31 (2002).

30. A. Lakhtakia, M. W. McCall, J. A. Sherwin, Q. H. Wu, Q. H. and I. J. Hodgkinson, "Sculptured-thin-film spectral holes for optical sensing of fluids" *Optics Communications*, **2001**, 194, 33.

31. M. Faraday, "Experimental relations of gold (and other metals) to light," *Philosophical Transactions*, **147**, 145 (1857).

32. R. F. Bunshah, *Handbook of Deposition Technologies for Films and Coatings*, Noyes Publications, Park Ridge (1994).

33. M. Ohring, *The Materials Science of Thin Films*, Academic Press, San Diego (1992).

34. B. N. Chapman, *Glow Discharge Processes*, Wiley, New York (1980).

35. L. I. Maissel and R. Glang, *Handbook of Thin Film Technology*, McGraw Hill, New York (1970).

36. J. A. Venables, G. D. T. Spiller, and M. Hanbucken, "Nucleation and growth of thin films," *Reports of Progress in Physics*, **47**, 399 (1984).

37. C. Ratsch and J. A. Venables, "Nucleation theory and the early stages of thin film growth," *Journal of Vacuum Science and Technology A*, **21**, S96 (2003).

38. M. Zinke-Allmang, L. C. Feldman, and M. H. Grabow, "Clustering on surfaces," *Surface Science Reports*, **16**, 377 (1992).

39. E. Ruckenstein and D. B. Dadyburjor, "Direct ripening of crystallites on a substrate," *Thin Solid Films*, **55**, 89 (1978).

40. M. Brinkmann, F. Biscarini, C. Taliani, I. Aeillo, and M. Ghedini, "Growth of mesoscopic correlated droplet patterns by high-vacuum sublimation," *Physical Review B*, **61**, R16339 (2000).

41. M. Brinkmann, S. Graff, and F. Biscarini, "Mechanism of nonrandom pattern formation of polar-conjugated molecules in a partial wetting regime," *Physical Review B*, **66**, 165430 (2002).

42. J. F. O'Hanlon, *A User's Guide to Vacuum Technology*, Wiley, New York (1989).

43. A. Movchan and A. V. Demchishin, "Study of the structure and properties of thick vacuum condensates of nickel, titanium, tungsten, aluminum oxide and zirconium dioxide," *The Physics of Metals and Metallography*, **28**, 83 (1969).

44. J. A. Thornton, "High rate thick film growth," *Annual Reviews of Materials Science*, **7**, 239 (1997).

45. R. Messier, A. P. Giri, and R. A. Roy, "Revised structure zone model for thin film physical structure," *Journal of Vacuum Science and Technology A*, **2**, 500 (1984).

46. R. Messier, "Toward quantification of thin film morphology," *Journal of Vacuum Science and Technology A*, **4**, 490 (1986).

47. T. G. Knorr and R. W. Hoffman, "Dependence of geometric magnetic anisotropy in thin iron films," *Physical Review B*, **113**, 1039 (1959).

48. D. O. Smith, "Anisotropy in permalloy films," *Journal of Applied Physics*, **30**, 264S (1959).

49. T. Motohiro and Y. Taga, "Thin film retardation plate by oblique deposition," *Applied Optics*, **28**, 2466 (1989).

50. K. Robbie, I. J. Friedrich, S. K. Dew, T. Smy, and M. J. Brett, "Fabrication of thin-films with highly porous microstructures," *Journal of Vacuum Science and Technology A*, **13**, 1032 (1995).

51. I. Hodgkinson, Q. H. Wu, and J. Hazel, "Empirical equations for the principal refractive indices and column angle of obliquely deposited films of tantalum oxide, titanium oxide, and zirconium oxide," *Applied Optics*, **37**, 2653 (1998).

52. J. Gospodyn and J. C. Sit, "Characterization of dielectric columnar thin films by variable angle Mueller matrix and spectroscopic ellipsometry," *Optical Materials*, in press (2006).

53. H. van Nieuwenhuizen and H. B. Haanstra, "Microfractography of thin films," *Philips Technical Review*, **27**, 87 (1966).

54. R. N. Tait, T. Smy, and M. J. Brett, "Modelling and characterization of columnar growth in evaporated films," *Thin Solid Films*, **226**, 196 (1993).

55. S. Lichter and J. Chen, "Model for columnar microstructure of thin solid films," *Physical Review Letters*, **56**, 1396 (1986).

56. Paritosh and D. J. Srolovitz, "Shadowing effects on the microstructure of obliquely deposited films," *Journal of Applied Physics*, **91**, 1963 (2002).

57. M. Malac, R. F. Egerton, M. J. Brett, and B. Dick, "Fabrication of submicrometer regular arrays of pillars and helices," *Journal of Vacuum Science and Technology B*, **17**, 2671 (1999).

58. B. Dick, M. J. Brett, T. J. Smy, M. R. Freeman, M. Malac, and R. F. Egerton, "Periodic magnetic microstructures by glancing angle deposition," *Journal of Vacuum Science and Technology A*, **18**, 1838 (2000).

59. M. O. Jensen and M. J. Brett, "Periodically structured glancing angle deposition thin films," *IEEE Transactions on Nanotechnology*, **4**, 269 (2005).

60. M. O. Jensen and M. J. Brett, "Functional pattern engineering in glancing angle deposition thin films," *Journal of Nanoscience and Nanotechnology*, **5**, 723 (2005).

61. J. C. Sit, D. Vick, K. Robbie, and M. J. Brett, "Thin film microstructure control using glancing angle deposition by sputtering," *Journal of Materials Research*, **14**, 1197 (1999).

62. D. Vick, Y. Y. Tsui, M. J. Brett, and R. Fedosejevs, "Production of porous carbon thin films by pulsed laser ablation," *Thin Solid Films*, **350**, 49 (1999).

63. B. Dick, "Properties and growth of thin films produced by glancing angle deposition," *Ph.D. Dissertation*, University of Alberta (2003).

64. P. C. P. Hrudey, K. L. Westra, and M. J. Brett, "Highly ordered organic Alq_3 chiral luminescent thin films fabricated by glancing-angle deposition," *Advanced Materials*, **18**, 224 (2006).

65. S. Pursel, M. W. Horn, M. C. Demirel, and A. Lakhtakia, "Growth of sculptured polymer submicron wire assemblies by vapor deposition," *Polymer*, **46**, 9544 (2005).

66. D. Vick, T. Smy, and M. J. Brett, "Growth behavior of evaporated porous thin films," *Journal of Materials Research*, **17**, 2904 (2002).

67. A. C. van Popta, J. C. Sit, and M. J. Brett, "Optical properties of porous helical thin films," *Applied Optics*, **43**, 3632 (2004).

68. I. Hodgkinson, Q. H. Wu, B. Knight, A. Lakhtakia, and K. Robbie, "Vacuum deposition of chiral sculptured thin films with high optical activity," *Applied Optics*, **39**, 642 (2000).

69. Q. H. Wu, I. J. Hodgkinson, and A. Lakhtakia, "Circular polarization filters made of chiral sculptured thin films: experimental and simulation results," *Optical Engineering*, **39**, 1863 (2000).

70. K. Robbie, D. J. Broer, and M. J. Brett, "Chiral nematic order in liquid crystals imposed by an engineered inorganic nanostructure", *Nature*, **399**, 764 (1996).

71. J. C. Sit, D. J. Broer, and M. J. Brett, "Alignment and switching of nematic liquid crystals embedded in porous chiral thin films," *Liquid Crystals*, **27**, 387 (2000).

72. N. G. Wakefield, A. L. Elias, M. J. Brett, and J. C. Sit, "Optical behaviour of hybrid LC/inorganic nanostructures," *SPIE Proceedings*, **6135**, 122 (2006).

73. O. Toader and S. John, "Proposed square spiral microfabrication for large three-dimensional photonic band gap crystals," *Science*, **292**, 1133 (2001).

74. K. D. Harris, K. L. Westra, and M. J. Brett, "Fabrication of perforated thin films with helical and chevron pore shapes," *Electrochemical and Solid-state Letters*, **4**, C39 (2001).

75. K. D. Harris, J. R. McBride, K. E. Niestering, and M. J. Brett, "Fabrication of porous platinum thin films for hydrocarbon sensor applications," *Sensors and Materials*, **13**, 225 (2001).

76. J. J. Steele, J. Gospodyn, J. C. Sit, M. J. Brett, "Impact of Morphology on High-Speed Humidity Sensor Performance," *IEEE Sensors*, **6**, 24 (2006).

77. K. D. Harris, M. J. Brett, T. J. Smy, and C. Backhouse, "Microchannel surface area enhancement using porous thin films," *Journal of the Electrochemical Society*, **147**, 2002 (2000).

78. G. K. Kiema, M. O. Jensen, and M. J. Brett, "Glancing angle deposition thin film microstructures for microfluidic applications," *Chemistry of Materials*, **17**, 4046 (2005).

79. J. N. Broughton and M. J. Brett, "Electrochemical capacitance in manganese thin films with chevron microstructure," *Electrochemical and Solid-state Letters*, **5**, A279 (2002).

80. K. D. Harris, D. Vick, E. J. Gonzalez, T. J. Smy, and M. J. Brett, "Porous thin films for thermal barrier coatings," *Surface and Coatings Technology*, **138**, 185 (2001).

81. G. K. Kiema, M .J. Colgan, and M. J. Brett, "Dye sensitized solar cells incorporating obliquely deposited titanium oxide layers," *Solar Energy Materials and Solar Cells*, **85**, 321(2005).

82. M .J. Colgan and M. J. Brett, "Field emission from carbon and silicon films with pillar microstructure", *Thin Solid Films*, **389**, 1 (2001).

83. A. L. Elias, K. D. Harris, C. W. M. Bastiaansen, D. J. Broer, and M. J. Brett, "Large-area microfabrication of three-dimensional, helical polymer structures," *Journal of Micromechanics and Microengineering*, **15**, 49 (2005).

CHAPTER 2
Background – chiral optics and luminescence

This aim of this chapter is to provide the reader with sufficient background on subjects that are relevant to the rest of this thesis, namely chiral optics and luminescence. The first portion of this chapter discusses the interactions between polarized light and the helical structures in chiral thin films. The second portion of this chapter reviews the concept of luminescence and outlines the mechanisms behind the photoluminescence of the commonly used inorganic and organic luminescent materials that were studied for the work in the rest of this thesis.

2.1 Chiral optics

Chirality, a term derived from the Greek work for 'handed,' is a type of asymmetry whereby an object and its mirror image are not identical to each other. Such pairs of unique, independent structures are termed enantiomorphs, and they can occur at any size scale. A screw is a macroscopic chiral object; the helices of chiral thin films fabricated by GLAD are microscopically chiral. Both a screw and a chiral thin film are examples of structurally chiral media, in contrast to the molecular chirality exhibited by many molecules, such as sucrose [1]. The study of the interaction between light and chiral media dates as far back as 1811 when Arago observed the rotation of the plane of polarization

of linearly polarized light as a beam of light propagated through a quartz crystal [2]. This effect, called optical activity, is but one effect examined in the general study of the interaction between light and chiral media, a field termed chiral optics. Other chiral optical effects include circular birefringence, circular dichroism, and circular Bragg phenomena. In order to understand these effects, it is first useful to review the classical equations defining the polarization states of light.

2.1.1 Polarized light

Light is classically described by a transverse electromagnetic wave that obeys Maxwell's equations [3]. To discuss polarization, it is convenient to consider a monochromatic plane wave. This wave is coherent and travels in the positive z-direction. The electric field and magnetic field vectors for such a wave are both orthogonal to the direction of propagation. In an isotropic, homogeneous, non-absorbing medium, the electric field vector is given by

$$\mathbf{E}(z,t) = \mathbf{A}\cos(\omega t - kz), \tag{2.1}$$

where $\mathbf{A}$ is the amplitude, ω is the angular frequency, t is time, and k is the wave number. By convention, the polarization state of this wave is defined by the temporal and spatial variance of this electric field vector. (The variance of the magnetic field vector can readily be determined if the electric field vector is known by using Maxwell's equations.) This electric field vector can be decomposed into two orthogonal components which are both in the plane perpendicular to the propagation direction. Generally, these components are

$$\mathbf{E}_x = \hat{\mathbf{x}}\, E_x \cos(\omega t - kz + \delta_x)$$
$$\mathbf{E}_y = \hat{\mathbf{y}}\, E_y \cos(\omega t - kz + \delta_y), \qquad (2.2)$$

where

$$\mathbf{A} = \hat{\mathbf{x}} E_x + \hat{\mathbf{y}} E_y \qquad (2.3)$$

and δ_x and δ_y are the independent phases of the two components. The amplitudes are restricted to positive values. This constrains the phase angles to the range $-\pi < \delta \leq \pi$. The amplitudes of these two electric field components are not necessarily equal ($E_x \neq E_y$) and the two components are not necessarily in phase ($\delta_x \neq \delta_y$). If one considers the shape that is projected onto a fixed plane orthogonal to the propagation direction, it is evident that the electric field vector traces out an ellipse (Fig 2.1). Accordingly, a light wave described by Eq. 2.2 is said to be elliptically polarized.

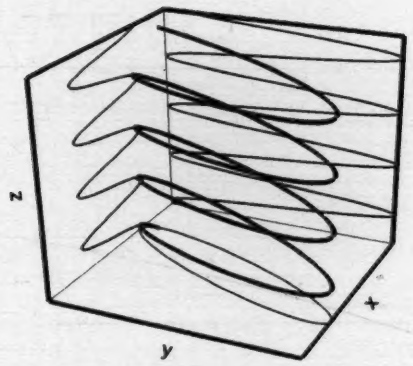

FIGURE 2.1

Elliptical polarization. Elliptical polarization is the most general polarization state and it arises when the electric field has two mutually independent components which differ in amplitude and are not in phase. When projected onto a plane parallel to the x-y plane at a given time, the electric field vector traces out an ellipse (red). The projections of the electric field vector in the x-z and y-z planes are both sinusoidal (blue and green lines).

Two other polarization states, linear and circular, exist and are special cases of the general elliptical polarization state described by Eq. 2.2. Linear polarization is the case where the electric field vector oscillates along a given line in the plane of observation (Fig. 2.2). This polarization state occurs when the components are either completely in phase ($\delta = \delta_y - \delta_x = 0$), or completely out of phase ($\delta = \delta_y - \delta_x = \pi$), giving Eq. 2.4.

$$\mathbf{E} = (\hat{\mathbf{x}}\, E_x \pm \hat{\mathbf{y}}\, E_y)\cos(\omega t - kz) \tag{2.4}$$

The orientation of the plane of polarization is determined by the relative magnitudes of E_x and E_y.

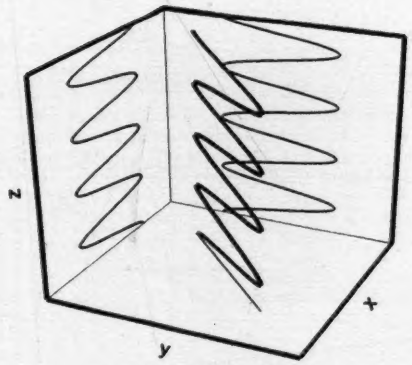

FIGURE 2.2

Linear polarization. Linear polarization occurs when the electric field vector has two mutually independent components that are either completely in phase or completely out of phase. When projected onto a plane parallel to the x-y plane at a given time, the electric field vector traces out a line (red). The projections of the electric field vector in the x-z and y-z planes are both sinusoidal (blue and green lines).

Circular polarization is where the electric field vector traces out a circle in the observation plane (Fig. 2.3). In this case, E_x and E_y are equal, and the phase difference is $\pm \pi/2$, giving Eq. 2.5.

$$\mathbf{E} = E\,[(\hat{\mathbf{x}}\cos(\omega t - kz) + \hat{\mathbf{y}}\cos(\omega t - kz + \delta)] \tag{2.5}$$

Two circular polarization states exist: one for $\delta = \pi/2$, and one for $\delta = -\pi/2$. To distinguish between these states, the case where $\delta = \pi/2$ will be called right-circularly polarized (RCP), and the case where $\delta = -\pi/2$ will be called left-circularly polarized (LCP). This definition arises from considering the helix that is traced out by the electric field vector when it is frozen in time. When $\delta = -\pi/2$, a left-handed helix results, hence the name left-circularly polarized light, and vice versa for $\delta = \pi/2$. This definition is called the

traditional convention for LCP and RCP [4]. An alternate definition, the modern physics and engineering convention, also exists. The modern physics convention reverses the definitions of LCP and RCP in terms of $\delta = \pm \pi/2$ from those considered here [1]. For the purposes of this thesis, the traditional convention where $\delta = -\pi/2$ is LCP and $\delta = \pi/2$ is RCP will be used, because it conveniently names the polarization state based upon the instantaneous spatial electric field pattern. Thus, the chiral optical effects discussed in the rest of this section are of the same handedness as the chiral structures that yield them.

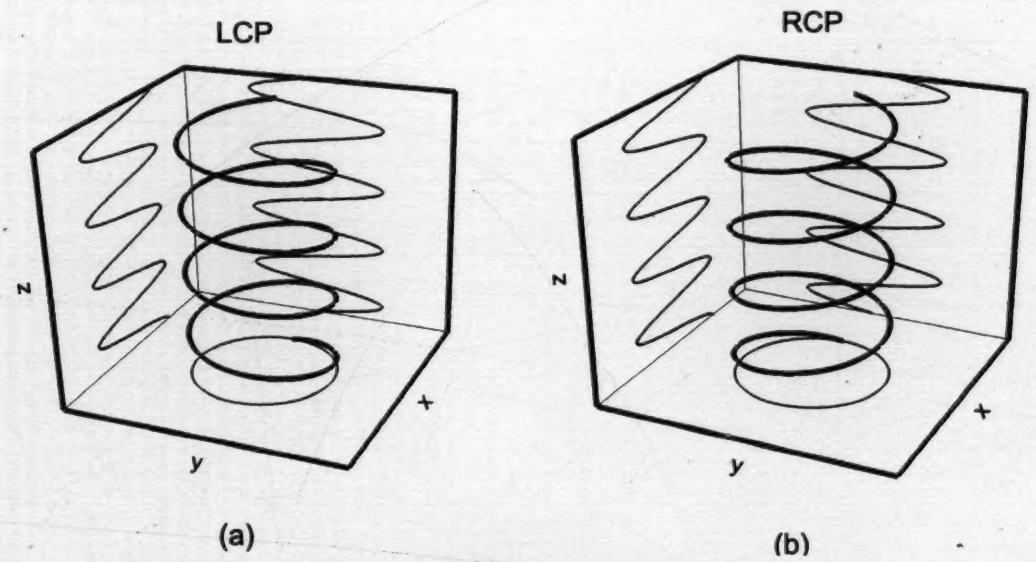

FIGURE 2.3:

Circular polarization. Examination of a snapshot frozen in time of the path traced by the electric field reveals the handedness of circularly polarized light: (a) a left-handed helical shape is attributed to left-circularly polarized (LCP) light, and vice versa for (b) a right-handed helical shape. When projected onto a plane parallel to the x-y plane at a given time, the electric field vector traces out a circle (red). The projections of the electric field vector in the x-z and y-z planes are both sinusoidal (blue and green lines).

2.1.2 Circular birefringence and circular dichroism

The optical properties of chiral media are readily understood by examining the interaction circularly polarized light with such materials. This approach can be used to explain all three of the widely studied chiral optical effects: circular birefringence [5, 6], circular dichroism [6, 7], and circular Bragg phenomena [1, 8 – 13]. Of these three effects, circular Bragg phenomena are the most likely to play a significant technological role when combined with a luminescent medium [14 – 17]. Thus, only a brief discussion of circular birefringence and circular dichroism will be given here.

Circular birefringence and circular dichroism were the first chiral optical effects to be observed. They are the source of the optical activity exhibited by chiral media such as a quartz crystal [2] and sugar solutions [18]. Fresnel considered the source of optical activity in quartz crystals, and he concluded that the propagation velocities of LCP and RCP light though differed for this chiral medium [5]. This means that the indices of refraction for LCP and RCP light differ in a chiral medium, and is analogous to the differing ordinary and extraordinary refractive indices of a linearly birefringent medium. This difference in refractive index for LCP and RCP light is termed circular birefringence. Circular dichroism, on the other hand, is the term applied to a chiral media that have a complex index of refraction (*i.e.* they are absorbing), and the extinction coefficients (the imaginary portion of the complex index of refraction) differ for LCP and RCP light.

When circularly polarized light traverses a chiral medium, only the circular polarization state that has the same handedness as that of the chiral medium will strongly couple to the medium; the opposite handedness does not couple to the medium and is thus unaffected by it. As optical activity involves the effects that a chiral medium has on a linearly polarized wave, it is necessary to recognize that a linearly polarized wave can

also be expressed in terms of two circularly polarized waves with opposite handedness, but with the same magnitude [19]. Thus, when a linearly polarized wave traverses a left-handed circularly birefringent medium, it can be thought of as a superposition of an LCP and an RCP wave. However, in a left-handed circularly birefringent medium, the phase velocity of the LCP component is reduced relative to the RCP component. Upon exiting the medium, the superposition of the LCP and RCP waves will produce a linearly polarized wave, however, the phase delay between the two circularly polarized states causes the plane of polarization of the linearly polarized output wave to be rotated relative to that of the input wave [6]. Similarly, in a left-handed circularly dichroic medium, the LCP component is attenuated as it travels through the medium. Thus, the superposition of the LCP and RCP waves that exit a circularly dichroic medium no longer forms a linearly polarized wave; the light that exits a circularly dichroic medium is elliptically polarized instead. The combination of both circular birefringence and circular dichroism accounts for the optical activity exhibited by any chiral medium.

2.1.3 Circular Bragg phenomena

While some combination of circular birefringence and circular dichroism occurs in all chiral media, the same cannot be said of circular Bragg phenomena. The circular Bragg phenomena that some chiral media display are a result of these media having some structural periodicity. A sugar solution has no structural periodicity so it will not display circular Bragg phenomena. Cholestric liquid crystals (CLCs) [1, 8 – 13] and chiral thin films [20] do , however, exhibit structural periodicity on the same scale as the wavelengths of visible light, so they do display observable circular Bragg phenomena. These phenomena are manifested as the selective reflection of one handedness of

circularly polarized light by the chiral medium. The theoretical foundations for circular Bragg phenomena have been widely studied over the past century [1, 8 – 13]. A brief summary of their theoretical derivation will be given here.

In a plane parallel to the substrate, both CLCs [1] and chiral thin films [21] are composed of anisotropic dielectric shapes of rods or fans, respectively. In each adjacent plane, these anistropic dielectric elements are slightly twisted, producing a periodic helical structure with a pitch, p. If these elements have no polarity (i.e. the ends of the element are indistinguishable from each other), then the spatial period is $p/2$, and the spatial wavenumber, q, is defined as

$$q = \frac{2\pi}{p} \tag{2.6}$$

Thus, a periodic chiral medium has a dielectric tensor given by

$$\varepsilon(z) = \varepsilon_0 \begin{pmatrix} \beta + \alpha\cos(2qz) & \alpha\sin(2qz) & 0 \\ \alpha\sin(2qz) & \beta - \alpha\cos(2qz) & 0 \\ 0 & 0 & \varepsilon_3/\varepsilon_0 \end{pmatrix} \tag{2.7}$$

where $\beta = (\varepsilon_1 + \varepsilon_2)/(2\varepsilon_0)$, $\alpha = (\varepsilon_1 - \varepsilon_2)/(2\varepsilon_0)$, ε_1, ε_2, and ε_3, are the principal dielectric constants of the local dielectric elements, and ε_0 is the dielectric constant of vacuum. By restricting the discussion to the consideration of propagation only along the helical axis, the solutions to the electric field wave equation for such a medium must obey the Bloch-Floquet theorem. This requires that the modes for propagation in the medium be expressed as the product of a periodic function and an exponential function [1]. In this case, the supported modes are defined by two wavenumbers, k_1 and k_2 given by

$$\begin{aligned} k_1^2 &= \beta k_0^2 + q^2 - \sqrt{4q^2\,\beta k_0^2 + \alpha^2 k_0^4} \\ k_2^2 &= \beta k_0^2 + q^2 + \sqrt{4q^2\,\beta k_0^2 + \alpha^2 k_0^4} \end{aligned} \tag{2.8}$$

where $k_0 = 2\pi/\lambda$ is the vacuum wavenumber. It is evident from Eq. 2.8 that k_2 is real for all wavelengths. On the other hand, k_1 is found to be purely imaginary for the wavelengths

$$n_o p < \lambda < n_e p \tag{2.9}$$

with $\varepsilon_2/\varepsilon_0 = n_o^2$ and $\varepsilon_1/\varepsilon_0 = n_e^2$. At these wavelengths, the mode with wavenumber k_1 cannot propagate through the chiral medium, and is reflected by the medium. However, the mode with k_2 can propagate through the chiral medium for these wavelengths, so the reflection is dependent upon polarization state of the incident light.

For reflection to occur, two conditions must be satisfied: the dynamic coupling condition and the Bragg condition [1]. The former stipulates that only the circular polarization state whose handedness matches that of the chiral structure will be reflected. The latter, states the conditions for constructive interference of waves reflected by the periodic structure, and can be expressed as

$$2k = 2q \tag{2.10}$$

for propagation along the helical axis. Substituting for q, and

$$k = \frac{2\pi}{\lambda} n_{eff} \tag{2.11}$$

with n_{eff} being the effective, or average, index of refraction of the medium, one can express the Bragg condition as

$$\lambda = n_{eff} p \tag{2.12}$$

As a final comment regarding circular Bragg phenomena, it should be noted that circularly polarized light reflected from a chiral medium through this selective reflection maintains

the same handedness as the incident light. This is in contrast to the reflection of circularly polarized light by metal mirrors [1].

2.2 Luminescence

Luminescence refers to energy conversion phenomena in which external, non-thermal energy excites a material, resulting in the emission of ultraviolet (UV), visible, or infrared (IR) light. This is in contrast to incandescence which is thermally-excited light emission from a material. Luminescence and incandescence can also be differentiated, because only certain materials exhibit luminescence, while incandescence occurs, in principle, for all materials, provided high enough temperatures are used. Luminescent materials can be either inorganic or organic, and are used in a wide variety of applications [22, 23]. These include fluorescent lamps, cathode-ray tubes, plasma display panels, electroluminescent displays, X-ray intensifying screens and scintillators for medical technologies, lasers, and even in luminous paints.

Luminescence is actually an umbrella term that covers a wide variety of light emission phenomena [22, 23]. These phenomena can be categorized based on the method of excitation involved, or by the time scales involved in the emissive process. Light, electric fields, electron bombardment, and X-rays are a few commonly used excitation methods, and the emission phenomena that occur because of these excitation methods are termed photoluminescence, electroluminescence, cathodoluminescence, and X-ray luminescence, accordingly. In a similar fashion, the terms fluorescence, phosphorescence, and after-glow are used to refer to emission processes with increasingly long decay times. There is, however, a wide variation in the true definition and usage of the terms

fluorescence and phosphorescence in the literature [22, 23]. Therefore, the umbrella term luminescence, or the excitation-based terms given above, will be used in this thesis, to avoid confusion. This is consistent with the convention established by Garlick [24], and used by Blasse and Grabmaier [22]. It should also be noted that for all of methods of excitation, luminescence phenomena must obey the law of energy conservation. Thus, the energy of the emitted light from a luminescent material must be less than that of the excitation source, a property called the Stokes shift [22, 25], with the rest of the energy being dissipated through non-radiative processes.

2.2.1 Inorganic luminescence

Inorganic luminescent materials tend to either be semiconducting materials or insulating materials [22]. Semiconductor luminescence typically occurs through charge recombination of electrons in the conduction or donor bands and holes in the valence or acceptor bands (Fig 2.4). In insulators, luminescence results from electronic transitions at localized centers such as impurity ions (*e.g.* Eu^{3+} in Y_2O_3:Eu), or, in some cases, complexes of the insulator itself (*e.g.* WO_4^- in $MgWO_4$). The experimental work in this thesis uses an insulating luminescent material, Y_2O_3:Eu. Hence, the subsequent discussion of inorganic luminescence mechanisms will be restricted to those relevant to luminescence from a localized center. Interested readers are referred to references [22, 25 – 27] for a rigorous treatment of inorganic luminescence.

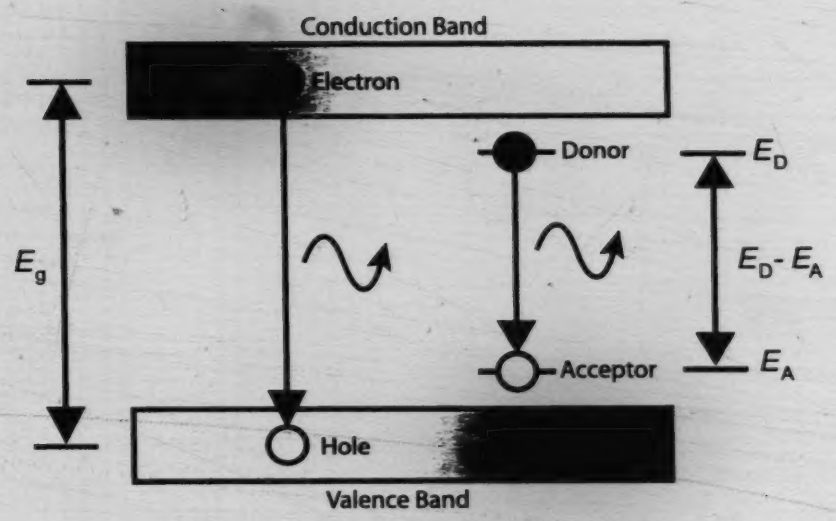

FIGURE 2.4

Band gap luminescence. Edge emission and donor-acceptor pair emission are two common emission band gap luminescence processes that occur when the recombination of an electron-hole pair results in the release of photons (depicted by waves here).

In most cases, insulating luminescent materials utilize transition metals or rare-earth elements as luminescent centers. To properly analyze the luminescence characteristics of materials incorporating such ions, a number of complex effects must be accounted for: coulombic interactions between the many electrons of the ion, spin interactions between the electrons (called spin-orbit coupling), and the coulombic effects of the crystal lattice that the ion is situated in (called the crystal field). While full and rigorous treatments of these effects exist [28 – 31], they are beyond the scope of this thesis. A brief overview of the key points needed to understand some of the terminology used to describe luminescence phenomena will be given here. This will include the introduction of the configurational coordinate model that is widely used [22, 25] to examine the transitions between electronic states for localized center luminescence.

2.2.1.1 *Term Symbols*

A short discussion will be given here of the meaning and formalism of term symbols, the representations of electronic states in many electron atoms. The quantum mechanical analysis of many electron atoms and ions is a great deal more complex than that of the hydrogen atom, because of the large number of electrons present. Interactions between electrons occur, including coulombic repulsion between electrons, and a weak magnetic interaction between the spin of the electrons and their orbital motion called spin-orbit coupling [28]. To analyze the effects that these interactions, complex calculations, such as Hartree-Fock calculations [28], are implemented. Such calculations assume one of two coupling regimes: *LS* coupling, where the electrostatic interaction is assumed to be much larger than the spin-orbit coupling; and *JJ* coupling, where the spin-orbit coupling is assumed to be larger than the electrostatic interaction. Typically, *LS* coupling is used in the analysis of lighter and medium-heavy atoms, and *JJ* coupling is used for the heaviest atoms [28 – 31]. These calculations determine the total angular momentum of the atom or ion under consideration.

Recall that the quantum mechanical state of an electron is completely described by four quantum numbers: n, the principal quantum number; l, the orbital angular momentum quantum number; m, the magnetic quantum number; and s, the spin quantum number [28]. Together these quantum numbers completely describe the electron configuration of a given electron. These numbers are allowed to take values in the ranges

$$\begin{aligned} &n = 1, \ldots \infty \\ &0 \le l \le n \\ &-l \le m \le l \\ &s = \pm ½ \end{aligned} \tag{2.13}$$

with the stipulation that no two electrons can be in the same state (Pauli's exclusion principle). The angular momentum of a given electron can be described by two quantized vectors, $\boldsymbol{l}$ and $\boldsymbol{s}$, that are related to l and s [28]. These vectors are used to determine electronic state of a many electron atom or ion by calculating the total orbital angular momentum, $\boldsymbol{L}$, the total spin angular momentum, $\boldsymbol{S}$, and the total angular momentum, $\boldsymbol{J}$. In the LS coupling scheme, these values are determined by

$$\begin{aligned} \boldsymbol{L} &= \sum_i \boldsymbol{l}_i \\ \boldsymbol{S} &= \sum_i \boldsymbol{s}_i \\ \boldsymbol{J} &= \boldsymbol{L} + \boldsymbol{S} \end{aligned} \tag{2.14}$$

and, in the JJ coupling scheme, these values are determined by

$$\begin{aligned} \boldsymbol{j}_i &= \boldsymbol{l}_i + \boldsymbol{s}_i \\ \boldsymbol{J} &= \sum_i \boldsymbol{j}_i \end{aligned} \tag{2.15}$$

Once the total orbital angular momentum, total spin angular momentum, and total angular momentum have been calculated, the total quantum numbers (L, S, and J) can be evaluated using

$$\begin{aligned} |\boldsymbol{L}| &= \hbar\sqrt{L(L+1)} \\ |\boldsymbol{S}| &= \hbar\sqrt{S(S+1)} \\ |\boldsymbol{J}| &= \hbar\sqrt{J(J+1)} \end{aligned} \tag{2.16}$$

where $\hbar$ is Planck's constant divided by 2π. Electronic states are then assigned a term symbol that takes the form

$$^{2S+1}L_J \tag{2.17}$$

and uses spectroscopists notation for L (i.e. L: S, P, D, F, G, H, ... for $L = 0, 1, 2, 3, 4, 5,$ ...). Electronic transitions are named accordingly with the form

$$({}^{2S+1}L_J)_{\text{initial}}\text{-}({}^{2S+1}L_J)_{\text{final}}. \tag{2.18}$$

2.2.1.2 Selection rules – forbidden and allowed electronic transitions

Electronic transitions in many electron atoms are categorized as either electric or magnetic multipoles. The strongest transitions, and transitions most relevant to the discussion of Y_2O_3:Eu that follows, are the electric dipole and magnetic dipole transitions. Not all electronic transitions are allowed by quantum mechanics: some transitions are forbidden by quantum mechanical selection rules that arise from the calculations used to analyze the electronic transitions of many electron atoms [22, 28, 32]. However, the effectiveness of these selection rules is highly dependent upon the circumstances, because the coupling scheme used, the type of transition being discussed, and the symmetry of the electric field (i.e. the crystal field) of surrounding atoms can all act to lift certain selection rules. For a full account of the selection rules, the interested reader is directed to reference [28]. The selection rules that will play a key role in the subsequent discussion of Y_2O_3:Eu are the parity selection rule ($\Delta l = \pm 1$), and the J selection rule ($\Delta J = 0, \pm 1$, $J = 0 \rightarrow J = 0$ forbidden) [22].

2.2.1.3 Configurational Coordinate Model

Because insulator luminescence occurs at localized luminescent centers, a band diagram analysis of the electronic transitions is not needed to gain a qualitative understanding of the electronic and vibrational processes involved in their luminescence.

Instead, a simpler model called the configurational coordinate model is used in these circumstances [22, 25]. In the configurational coordinate model, the localized nature of the situation allows only the luminescent ion and its surrounding ligands to be considered. Attributes such as the Stokes' shift, the width of the absorption and emission bands, and thermal quenching effects can all be qualitatively assessed for a given luminescent material using this model.

The configurational coordinate model gets its name because it examines the total energy of the electronic states of the metal ion as a function of the metal-ligand distance, which is referred to as a configurational coordinate, Q. This is done with the assumption that the bonding forces between the metal ion and its ligands are harmonic (i.e. they follow Hooke's law). Therefore, the total energy of the ground state can be written as

$$U_g = k_g \frac{Q^2}{2} \tag{2.19}$$

where U_g is the energy of the ground state, k_g is the force constant of the chemical bond, and Q is the configurational coordinate. The excited state is then generally described by Eq. 2.20

$$U_e = k_e \frac{(Q - Q_o)^2}{2} + U_o \tag{2.20}$$

where U_e is the energy of the excited state, k_e is the force constant of the chemical bond in the excited state, and Q_o is the equilibrium distance in the excited state, and U_o is the energy at $Q = Q_o$. The quantum mechanical solution to these forces is given by considering the well-known simple harmonic oscillator problem [22, 25], and this defines the quantized energy levels that can be considered in the configurational coordinate model. This situation can be depicted graphically (Fig. 2.5).

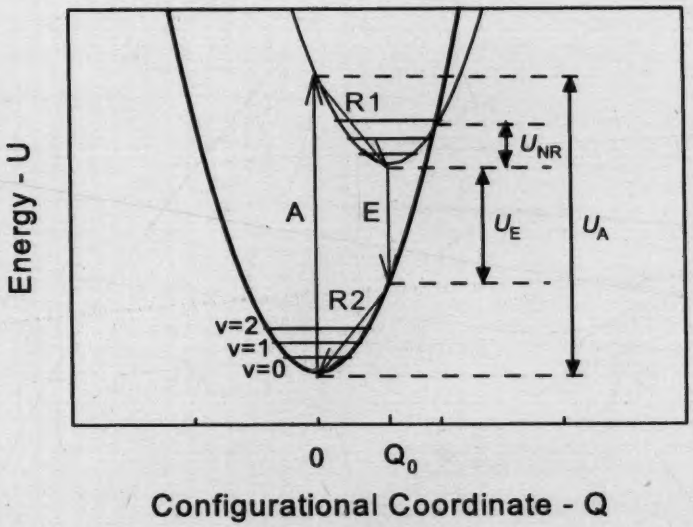

FIGURE 2.5

Generalized configurational coordinate diagram. Configurational coordinates are generated by considering the vibrations, and the potential energy due to such vibrations, between an ion and its surrounding ligands. In order to account for the quantum mechanical nature, the configurational coordinate models uses a harmonic oscillator model to yield the discrete energy levels depicted.

In Fig. 2.5, the horizontal lines represent the quantized energy levels, and the parabolic curves represent the total energy of a given state. Vertical displacements are electronic transitions, and horizontal displacements are nuclear in nature, since Q is an internuclear distance [22]. A typical luminescent process occurs as follows. External energy, such as the absorption of a photon with energy greater than U_A, excites an electron from the ground state to the excited state (transition A). Once in the excited state, the electron relaxes to the lowest vibrational level through lattice vibrations (transition R1). This is because the probability of energy being lost to lattice vibrations is higher than the probability of light emission for this arrangement [25]. Once relaxation has occurred,

the emission process is favoured, and luminescence occurs (transition E). The electron returns to the ground state through transition E, but must then undergo another relaxation process (transition R2) to return to the lowest vibrational level.

Some key observations can be made from this diagram. Qualitatively, Q_o is related to the width of both the optical transitions (A and E), and to the Stokes' shift. Larger values of Q_o lead to optical transitions with wider bands, and a larger Stokes' shift. This is because the wavefunction of the first vibrational mode (v = 0) of the ground state is most probable at the center of the parabola (i.e. $Q = 0$ for the ground state), the wavefunctions for the higher vibrational modes are most probable at the edges of the parabolas [22]. Thus, transitions A and E are only one possible set of excitation and emission phenomena, with additional transitions being made more probable for larger values of Q_o. Similarly, if Q_o is larger, then additional relaxation processes will follow the excitation and emission phenomenon. This results in greater amounts of energy being lost to these non-radiative relaxations. The relaxation processes, which lead to a lower energy for the emitted photon (U_E) than the absorbed energy, are the source of the Stokes' shift: therefore, a larger value of Q_o is related to a larger Stokes' shift. Another significant element of Fig. 2.3 is the cross-over point between the two parabolas. If the electron has enough thermal energy, $kT > U_{NR}$ (where k is Boltzmann's constant and T is the temperature), it can reach this cross-over point an return to the ground state through a non-radiative transition. Thus, this cross-over point demonstrates the potential for thermal quenching effects. More detailed evaluations of configurational coordinate diagrams can be performed, allowing some quantitative analysis of the energy transfer processes involved: the interested reader may find discussion of such calculations in reference [25].

2.2.1.4 Europium-doped yttrium oxide (Y_2O_3:Eu)

The inorganic luminescent material was used in this thesis was europium-doped yttrium oxide (Y_2O_3:Eu). This luminescent material has been extensively studied an characterized over the past half-century [33 – 39]. Europium-doped yttrium oxide has also been widely used over the same time period in commercial applications [22, 40], such as lighting and displays, because of the strong, narrow line emission it produces at a wavelength of 611 nm. The configurational coordinate diagram for this material [37], which was developed using knowledge of both the host material (Y_2O_3) and the dopant ions (Eu^{3+}), provides a clear description of the electronic transitions and luminescence processes at work.

The Eu^{3+} ions in Y_2O_3:Eu are substitutional impurities for Y^{3+} ions in Y_2O_3 [33 – 39]. Y_2O_3 forms either a monoclinic or cubic *C*-type sesquioxide crystal structure [41, 42], though the cubic *C*-type structure is of the most interest as it is solely used in commercial applications of Y_2O_3. In this structure, the Y^{3+} ion is located at the center of the cubic structure and is surrounded by six O^{2-} ions. This results in two possible site symmetries (Fig. 2.6): C_2, where the vacancy diagonal lies upon one face of the Y-centered cube; and S_6, where the vacancy lies upon the diagonal through the Y-centered cube. Thus, each O^{2-} ions bonds to two Y^{3+} ions, and to generate the full crystal lattice, 75% of the Y^{3+} ions sites have C_2 symmetry, and 25% have S_6 symmetry. Notably, S_6 symmetry sites exhibit inversion symmetry, however, the C_2 symmetry sites do not [22, 43].

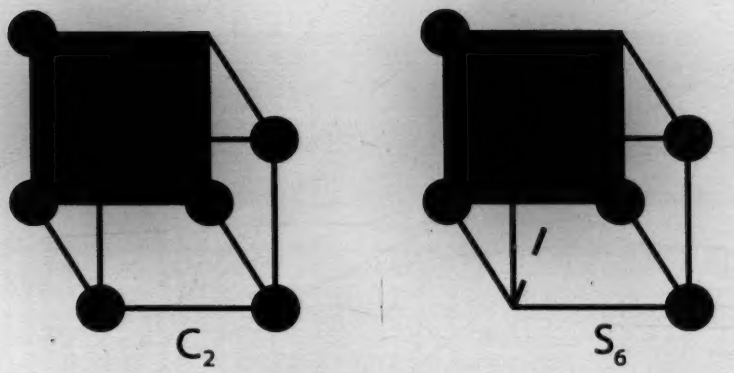

FIGURE 2.6

Y_2O_3 crystallographic symmetries. Y_2O_3 has a cubic C-type crystal structure in which six oxygen anions surround each yttrium cation to maintain charge neutrality. Two distorted cubic cells result: one with the vacancies lined up along the body diagonal (S_6), and one with the vacancies lined up along the face diagonal (C_2).

The Eu^{3+} impurity ion that acts as the luminescent center in Y_2O_3:Eu is a rare-earth metal ion that has been widely studied because it has an electron configuration of the form [Xe]$4f^6$ [29-31]. The energy levels of the $4f^6$ electrons are relatively insensitive to the surroudings of the ion, because they are shielded from the surrounding environment by the filled $5s^2$ and $5p^6$ orbitals. The electronic transitions of Eu^{3+} are determined by Judd-Ofelt theory, and found to involve electric dipole and magnetic dipole transitions between the ^7F_J (ground state) and ^5D_J (excited state) levels [29, 31] of the $4f$ orbital. However, the quantum selection rules must be considered. The electric dipole transitions are forbidden due the parity selection rule (i.e. $4f$-$4f$ transitions are forbidden). The magnetic dipole transitions are not subject to the parity selection rule and may occur provided the transitions satisfy the J selection rule, though these transitions are generally weak compared to electric dipole transitions [32, 43]. Also, emissions from the $^5D_1$ and $^5D_2$ states are quenched because electrons reaching these states readily relax to the

$^5D_0$ level [22, 43]. Thus, free Eu^{3+} ions primarily show a magnetic dipole emission based on the $^5D_0$-$^7F_1$ transition. Nonetheless, Y_2O_3:Eu yields a strong, efficient electric dipole emission peak at 611 nm. This is because 25% of the Eu^{3+} ions occupy the S_6 symmetry, and 75% sites C_2 symmetry sites. The lack of inversion symmetry at the C_2 sites produces a crystal field that relaxes the parity selection rule by mixing the 4f level with some opposite parity states [22, 35, 36, 38, 43]. Thus, Eu^{3+} ions at S_6 symmetry sites still tend to produce the $^5D_0$-$^7F_1$ magnetic dipole transition, or transfer energy to ions at C_2 sites. Ions at the C_2 sites yield the strong electric dipole transition, $^5D_0$-$^7F_2$, because this transition is sensitive to the relaxation of the parity selection rule [22, 35, 36, 38, 43]. The $^5D_0$-$^7F_2$ electric dipole transition is the source of the characteristic 611 nm peak used in commercial applications of Y_2O_3:Eu.

A simplified version of the configurational coordinate diagram for Y_2O_3:Eu looks as shown in Fig. 2.7, with only the $^5D_0$ and $^7F_2$ energy states that give rise to the largest luminescence peak observed for Y_2O_3:Eu displayed. The most common excitation mechanism for photoluminescence from Y_2O_3:Eu involves the charge-transfer state (CTS), which is depicted in Fig. 2.7. The CTS results from the Eu^{3+} only having 6 *f*-orbital electrons: one short of the much more stable configuration of 7 *f*-orbital electrons, for which half of the *f*-orbital is filled. Since the O^{2-} ion has two valence electrons, one electron jumps from the O^{2-} ion to the Eu^{3+} ion, resulting in the CTS. This leads to a strong, broad absorption band centered at 254 nm because of the interaction between light and the dipole that results from this charge transfer. The CTS readily feeds the emitting $^5D_0$ states, leading to very efficient emission [22, 34 – 38]. An example of the emission spectrum of Y_2O_3:Eu is shown in Fig. 2.8, with the commonly observed transitions labeled.

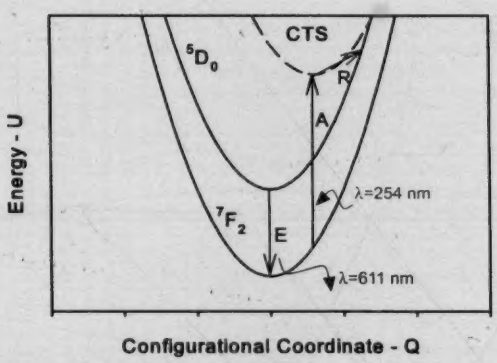

FIGURE 2.7

Configurational coordinate diagram for Y_2O_3:Eu. Y_2O_3:Eu has a very strong absorption band around 254 nm due to the allowed transition between the ^7F_J manifold and the CTS. Electrons excited to the CTS non-radiatively relax to the ^5D_J manifold, before emitting a photon to return to the ^7F_J manifold.

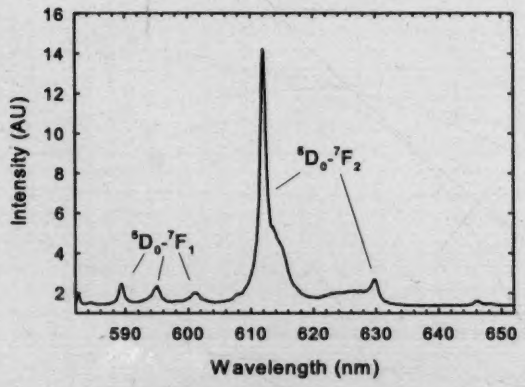

FIGURE 2.8

Photoluminescence spectrum of Y_2O_3:Eu. The most commonly studied optical transitions are labeled, including the $^5D_0$-$^7F_2$ transition at 611 nm which is due to a hypersensitive electric-dipole transition that is allowed due to the lack of inversion symmetry in the crystal structure of Y_2O_3:Eu. The multiple narrow lines for each transition are a result of the crystal field producing crystal field splitting of the ^7F_J states.

2.2.2 Organic Luminescence

Organic luminescence involves localized electronic transitions that are in some ways similar to both semiconductor and insulator luminescence for inorganic materials. The models used to describe organic luminescence bear a striking resemblance to discussion of conduction and valence bands in semiconductors. However, the electronic transitions involved in organic luminescence can be thought of localized phenomena that occur within the molecular structure of individual molecules [44 – 46].

For organic luminescence, the concepts of the highest occupied molecular orbital (HOMO) and lowest unoccupied molecular orbital (LUMO) are introduced [46], in analogy to the valence and conduction bands, respectively, that are used to model electronic transitions in semiconductors. Each molecular orbital contains no more than two electrons, with the electrons having antiparallel spins. These molecular orbitals can be calculated using quantum mechanical analysis and the methods of computational chemistry [46 – 48]. Excitation energy causes one of the electrons in the HOMO to be excited into the LUMO, as shown in Fig. 2.9. Upon returning to the HOMO, the electron emits a photon. Physically, these transitions involve electrons in the π bonds of the molecule [44, 45].

The energy states of the molecular orbitals can further be categorized by their spin multiplicity into either singlet (S) or triplet (T) states. Transitions between S and T states are forbidden, due to a quantum mechanical spin selection rule. Thus, as the ground state is typically S_0, any transitions by electrons in excited T states will take a long time (i.e. microseconds or milliseconds) compared to transitions that only occur between S states which typically take a few nanoseconds [44]. Thus, singlet state emission is more

common than triplet state emission. The organic luminescent material that was used in the work discussed here, tris (8-hydroxyquinoline) aluminum (Alq_3), is a singlet state emitter.

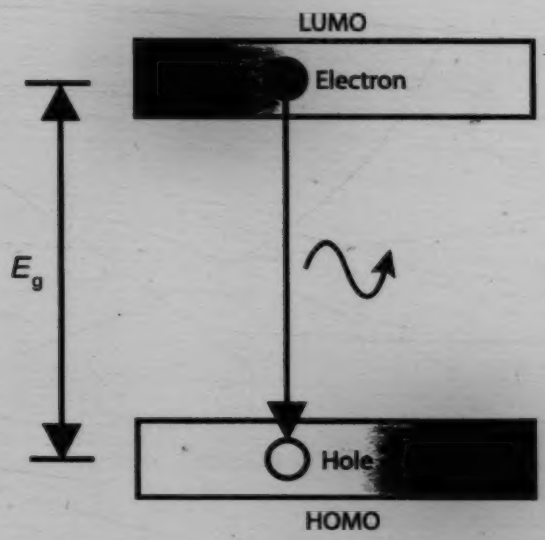

FIGURE 2.9

Energy level diagram of molecular orbitals. Organic luminescence occurs when electrons excited into the LUMO recombine with holes in the HOMO, releasing a photon (depicted by the wave) in the process.

2.2.3 tris (8-hydroxyquinoline) aluminum (Alq_3)

Tris-(8-hydroxyquinoline) aluminum (Alq_3) is a coordination complex that has been extensively studied ever since its use in the first low-voltage organic light emitting devices (OLEDs) [49]. Vacuum sublimed Alq_3 films have been frequenty examined for their use as emissive layers in OLEDs [44, 45, 49 – 54]. Alq_3 consists of an aluminum ion surrounded by three quinolate ligands (Fig. 2.10). This molecule forms either a meridianal isomer (*mer*) or a facial isomer (*iso*), though the *mer* isomer is more

energetically favorable and thus is observed more often [47]. Solid Alq_3 films are found to form in an amorphous phase, even for substrate temperatures near 170°C (desorption is dominant for higher substrate temperatures) [55].

The excited states that give rise to luminescence in Alq_3 (Fig. 2.11) occur at the quinolate ligands. Excitation energy generates an electron-hole pair. Because the dielectric constant is relatively low for Alq_3 compared to inorganic semiconductors, the electron-hole pair tends to have strong coulombic attractions, and is referred to as a Frenkel exciton [51]. Frenkel excitons formed by Alq_3 are localized to a given ligand, as the hole resides on the phenoxide ring and the electron is localized to the pyridyl ring [47, 51]. The photoexcitation absorption band that enables the formation of these excitons is found to be quite wide, extending from ~ 250 nm to ~ 470 nm [50, 56]. The breadth of the absorption band is attributed to the π-conjugation of the molecule, and to the incorporation of nitrogen and oxygen atoms in the chemical structure [44]. Light emission occurs when the Frenkel exciton recombines, giving rise to a broad luminescence peak near ~ 520 nm [47, 50, 51, 56]. The spectral breadth of the photoluminescence peak is the result of a structural relaxation of the molecule [51], called a Franck-Condon shift, which occurs because the excited state of the ligand couples some energy to vibrational modes.

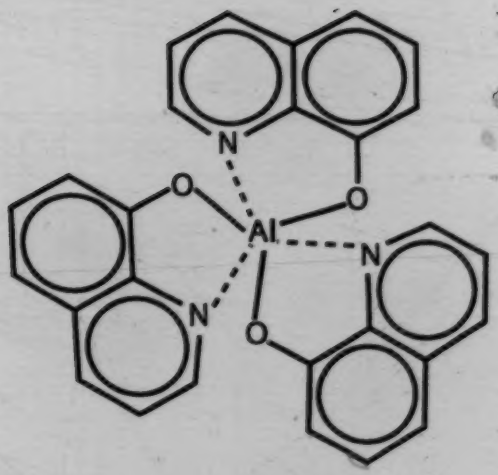

FIGURE 2.10

Chemical structure of tris-(8-hydroxyquinoline) aluminum (Alq_3). The molecule is made up of three quinolate ligands bonded to an aluminum ion. Each quinolate ligand includes a phenoxide ring which includes oxygen atom of the ligand and a pyridyl ring which includes the nitrogen atom of the ligand.

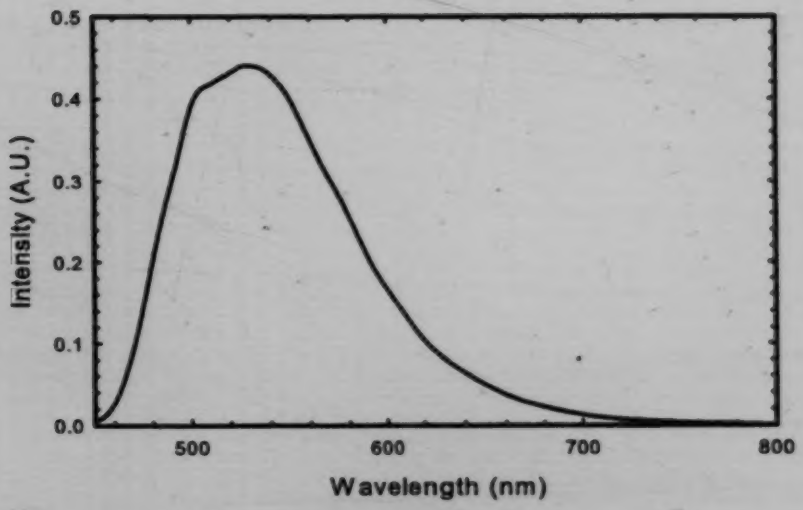

FIGURE 2.11

Photoluminescence spectrum of Alq_3. The spectrum consists of a single, broad peak that reaches a maximum value for 515 nm $< \lambda <$ 550 nm, depending on the purity and form of the material.

2.3 Summary

The research that will be discussed in the subsequent chapters focuses upon the study of the optical properties of chiral thin films of Y_2O_3:Eu and Alq_3, with the observation of circular Bragg phenomena for photoluminescent emission from such films being the main goal. The foundations of why circular Bragg phenomena occur for chiral thin films were outlined here, along with the luminescence mechanisms of Y_2O_3:Eu and Alq_3. Both of these materials are widely used, commercially important luminescent materials. This is advantageous for the work demonstrated in this thesis, because the luminescence properties of these films are understood quite well.

References

1. P. Yeh and C. Gu, *Optics of Liquid Crystal Displays*, Wiley, New York (1999).
2. D. F. J. Arago, *Mem. De l'Inst.*, **12**, 93 (1811).
3. B. E. A. Saleh and M. C. Teich, *Fundamentals of photonics*, Wiley, New York (1991).
4. C. F. Bohren and D. R. Huffman, *Absorption and scattering of light by small particles*, Wiley, New York (1983).
5. A. Fresnel, *Ann. Chim. Phys.*, **28**, 147 (1825).
6. E. U. Condon, "Theories of optical rotatory power," *Reviews of Modern Physics*, **9**, 432 (1937).
7. N. Berova, N. Nakanishi, and R. W. Woody (Eds.), *Circular Dichroism*, Wiley-VCH, New York (2000).
8. C. W. Oseen, "The theory of liquid crystals," *Transactions of the Faraday Society*, **29**, 883 (1933).
9. H. de Vries, "Rotatory power and other optical properties of certain liquid crystals," *Acta Crystallographica*, **4**, 219 (1951).

10. S. Chandrasekhar, *Liquid Crystals*, Cambridge University Press, Cambridge (1992).

11. P.G. de Gennes and J. Prost, *The Physics of Liquid Crystals*, Oxford University Press, Oxford (1993).

12. A. Lakhatakia and W. S. Weiglhofer, "On light propagation in helicoidal bianisotropic mediums," *Proceedings of the Royal Society of London A*, **448**, 419 (1995).

13. K. M. Flood and D. L Jaggard, "Band-gap structure for periodic chiral media," *Journal of the Optical Society of America A*, **13**, 1395 (1996).

14. D. J. Broer, J. Franciscus, J. J. van Tongeren, R. J. Visser, *US Patent Application*, 2005/0179371A1 (2005).

15. I. E. J. R. Heynderickx and D. J. Broer, *US Patent*, 5,626,408 (1997).

16. D. R. Hall, *US Patent*, 5,699,184 (1997).

17. V. I. Kopp, Z.-Q. Zhang, A. Z. Genack, "Lasing in chiral photonic structures," *Progress in quantum electronics*, **27**, 369 (2003).

18. J. B. Biot, *Mem. de l'Inst.*, **13**, 218 (1812).

19. E. Hecht, *Optics*, Addison-Wesley, Reading, Mass., USA (2001).

20. Q. H. Wu, I. J. Hodgkinson, and A. Lakhtakia, "Circular polarization filters made of chiral sculptured thin films: experimental and simulation results," *Optical Engineering*, **39**, 1863 (2000).

21. I. J. Hodgkinson, Q.H. Wu, *Birefringent Thin Films and Polarizing Elements*, World Scientific Press, Singapore (1997).

22. 22. G. Blasse and B. C. Grabmaier, *Luminescent Materials*, Springer-Verlag, Berlin (1994).

23. S. Shionoya, "Introduction to the handbook," *Phosphor Handbook*, ed. S. Shinoya and W. M. Yen, CRC Press, New York, 3 (1999).

24. G. F. J. Garlick, in *Handbook der Physik*, ed. S. Flügge, Springer, Berlin, 1 (1958).

25. H. Yamamoto, "Fundamentals of luminescence: luminescence of a localized center," *Phosphor Handbook*, ed. S. Shinoya and W. M. Yen, CRC Press, New York, 35 (1999).

26. S. Nara and S. Ibuki, "Fundamentals of luminescence: electronic states and optical transition of solid crystals," *Phosphor Handbook*, ed. S. Shinoya and W. M. Yen, CRC Press, New York, 21 (1999).

27. A. H. Kitai, *Solid state luminescence: Theory, Materials, and Devices*, Chapman and Hall, London (1993).

28. A. Thorne, U. Litzén, and S. Johansson, *Spectrophysics*, Springer, Berlin (1999).

29. B. R. Judd, "Optical absorption intensities of rare-earth ions," *Physical Review*, **127**, 750 (1962).

30. A. J. Freeman and R. E. Watson, "Theoretical investigation of some magnetic and spectroscopic properties of rare-earth ions," *Physical Review*, **127**, 2058 (1962).

31. G. S. Ofelt, "Structures of the f^6 configuration with application to rare-earth ions," *The Journal of Chemical Physics*, **38**, 2171 (1963).

32. E. Nakazawa, "Fundamentals of luminescence: absorption and emission of light," *Phosphor Handbook*, ed. S. Shinoya and W. M. Yen, CRC Press, New York, 11 (1999).

33. N. C. Chang, "Fluorescence and stimulated emission from trivalent europium in yttrium oxide," *Journal of Applied Physics*, **34**, 3500 (1963).

34. M. J. Weber, "Radiative and multiphonon relaxation of rare-earth ions in Y_2O_3," *Physical Review*, **171**, 283 (1968).

35. H. Forest and G. Ban, "Evidence for Eu^{3+} emission from two symmetry sites in Y_2O_3:Eu^{3+}," *Journal of the Electrochemical Society*, **116**, 474 (1969).

36. J. Heber, K. H. Hallwege, U. Köbler, and H. Murmann, "Energy levels and interaction between Eu^{3+}-ions at lattice sites of symmetry C_2 and symmetry C_{3i} in Y_2O_3," *Zeitschrift für Physik*, **237**, 189 (1970).

37. C. W. Struck and W. H. Fonger, "Role of the charge-transfer states in feeding and thermally emptying the ^5D states of Eu^{+3} in yttrium and lanthanum oxysulfides," *Journal of Luminescence*, **1-2**, 456 (1970).

38. M. Buijs, A. Meyerink, and G. Blasse, "Energy transfer between Eu^{3+} ions in a lattice with two different crystallographic sites: Y_2O_3:Eu^{3+}, Gd_2O_3:Eu^{3+}, and Eu_2O_3," *Journal of Luminescence*, **37**, 9 (1987).

39. R. M. Ranson, E. Evangelou, and C. B. Thomas, "Modeling the fluorescent lifetime of Y_2O_3:Eu," *Applied Physics Letters*, **72**, 2663 (1998).

40. S. Nakajima and M. Tamatani, "History of phosphor technology and industry," *Phosphor Handbook*, ed. S. Shinoya and W. M. Yen, CRC Press, New York, 821 (1999).

41. F. Jollet, C. Noguera, N. Thromat, M. Gautier, and J. P. Duraud, "Electronic structure of yttrium oxide," *Physical Review B*, **42**, 7587 (1990).

42. Y.-N. Xu, Z.-q. Gu, and W. Y. Ching, "Electronic, structural, and optical properties of crystalline yttria," *Physical Review B*, **56**, 14993 (1997).

43. T. Kano, "Principal phosphor materials and their optical properties," *Phosphor Handbook*, ed. S. Shinoya and W. M. Yen, CRC Press, New York, 177 (1999).

44. T. Tsutsui, "Fundamentals of luminescence: luminescence of organic compounds," *Phosphor Handbook*, ed. S. Shinoya and W. M. Yen, CRC Press, New York, 61 (1999).

45. T. Tsutsui, "Electroluminescence in small molecules," *Organic Electroluminescence*, ed. Z. H. Kafafi, CRC Press, New York (2005).

46. M. Pope and C. E. Swenberg, *Electronic processes in organic crystals and polymers*, Oxford University Press, Oxford (1999).

47. A. Curioni, M. Boero, and W. Andreoni, "Alq_3: ab initio calculations of its structure and electronic properties in neutral and charged states," *Chemical Physics Letters*, **294**, 263 (1998).

48. M. D. Halls and H. B. Schlegel, "Molecular orbital study of the first excited state of the OLED material tris(8-hydroxyquinoline)aluminum(III)," *Chemistry of Materials*, **13**, 2632 (2001).

49. C. W. Tang and S. A. VanSlyke, "Organic electroluminescent diodes," *Applied Physics Letters*, **51**, 913 (1987).

50. A. Schmidt, M. L. Anderson, and N. R. Armstrong, "Electronic states of vapor deposited electron and hole transport agents and luminescent materials for light-emitting diodes," *Journal of Applied Physics*, **78**, 5619 (1995).

51. P. E. Burrows, Z. Shen, V. Bulovic, D. M. McCarty, and S. R. Forrest, "Relationship between electroluminescence and current transport in organic heterojunction light-emitting devices," *Journal of Applied Physics*, **79**, 7991 (1996).

52. W. Humbs, E. van Veldhoven, H. Zhang, and M. Glasbeek, "Sub-picosecond fluorescence dynamics of organic light-emitting diode *tris*(8-hydroxyquinoline) metal complexes," *Chemical Physics Letters*, **304**, 10 (1999).

53. T. Tsuboi, Y. Wasai, and N. Nabatova-Gabain, "Spectroscopic ellipsometry study of organic light emitting diodes based on phosphorescent PtOEP," *IEICE Transactions on Electronics*, **E87-C**, 2039 (2004).

54. C. Himcinschi, N. Meyer, S. Hartmann, M. Gersdorff, H.-H. Johannes, W. Kowalsky, M. Schwambera, G. Strauch, M. Heuken, and D. R. T. Zahn, "Spectroscopic ellipsometric characterization of organic films obtained via organic vapor phase deposition," *Applied Physics A*, **80**, 551 (2005).

55. M. Brinkmann, G. Gadret, M. Muccini, C. Taliani, N. Masciocchi, and A. Sironi, "Correlation between molecular packing and optical properties in different crystalline polymorphs and amorphous thin films or *mer*-Tris(8-hydroxyquinoline) aluminum(III)," *Journal of the American Chemical Society*, **122**, 5147 (2000).

56. D. Z. Garbuzov, V. Bulović, P. E. Burrows, S. R. Forrest, "Photoluminescence efficiency and absorption of aluminum-tris-quinolate (Alq_3) thin films," *Chemical Physics Letters*, **249**, 433 (1996).

CHAPTER 3
Fabrication and preliminary characterization of nanostructured Y_2O_3:Eu thin films

This chapter deals with the fabrication of luminescent nanostructured Y_2O_3:Eu thin films and the preliminary characterization of such films. The film deposition and post-deposition processing methods are presented, along with the structural and compositional characterization data provided by scanning electron microscopy (SEM) imaging, X-ray diffraction (XRD), and X-ray photoelectron spectroscopy (XPS). Preliminary photoluminescence characterization of these initial nanostructured Y_2O_3:Eu thin films is also presented. These data were used to aid in establishing a reliable process for fabricating luminescent nanostructured Y_2O_3:Eu thin films with detectable levels of luminescence.

3.1 Fabrication

Solid thin films of Y_2O_3:Eu have been studied for decades with the aim of creating bright, high resolution luminescent thin films with good heat resistance characteristics for use in cathode ray tube displays [1 – 3], field emission displays [4], and thermographic sensors for measuring temperatures inside turbines [5, 6]. Such films have been fabricated using many different processes, including electron beam evaporation [1,2], magnetron sputtering [5], pulsed laser deposition (PLD) [4,7 – 10], metal-organic chemical vapor

deposition (MOCVD) [11], and sol-gel processing [12]. Commonly, Y_2O_3:Eu films produced via such deposition techniques exhibit poor luminescence characteristics unless subjected to high substrate temperatures or high temperature post-deposition annealing processes. Typically, temperatures in excess of 800°C are required, though temperatures in excess of 1000°C were shown to be preferable for maximum luminescence efficiency and brightness [1-12]. Even after being processed at high temperatures, solid luminescent thin films exhibit lower luminescence efficiencies than the same materials in bulk form. This is partly a result of issues such as waveguiding of the luminescent output within the film and absorption of the luminescent output by the substrate [8 – 10]. The combination of these waveguiding effects, non-radiative trap states, and small grain sizes has been shown to limit the photoluminescent efficiency of luminescent thin films to a few percent [4, 7 – 10] -- values substantially lower than the efficiency of the same materials in bulk form. As an alternative, the optical and structural properties of various nanocrystalline and nanoparticle forms of Y_2O_3:Eu have also been studied in the hopes that the conversion efficiencies of such materials will be improved compared to those of the bulk material [13 – 19]. None of these reports, however, have attempted to fabricate luminescent thin films designed to emit polarized light. This is a niche in which luminescent chiral thin films fabricated by GLAD could potentially prove useful. Prior to designing and fabricating luminescent chiral thin films that could emit polarized light, the ability to fabricate and produce photoluminescence with GLAD films first had to be demonstrated.

Of the fabrication methods that have been used to produce solid luminescent Y_2O_3:Eu films [1,2,5 – 11], electron beam evaporation, sputtering, and pulsed laser deposition are the only methods compatible with GLAD [20 – 22]. Of these three methods, the most efficient solid luminescent films have been reported for sputtering [5] and PLD

[4], and in both of these reports elevated substrate temperatures of 300°C – 800°C were commonly used during film deposition [4, 5]. While nanostructured thin films can be produced with GLAD using sputtering and PLD, the nanoscale morphologies of the films tend to be less well-defined when using these techniques instead of evaporation [23]. This is a result of the wider vapor flux distribution characteristic of sputtering and reactive PLD [24], when compared to evaporation. Furthermore, given the central role that limited adatom diffusion plays in GLAD, the elevated substrate temperatures cited in the literature for sputtering and PLD growth of solid Y_2O_3:Eu films would be expected to lead to even further degradation of the nanoscale morphology of the films. The nanoscale morphology has been theoretically demonstrated [25] to play a key role in determining the optical properties of films produced by GLAD. Thus, in attempting to fabricate luminescent chiral thin films of Y_2O_3:Eu a dilemma arises with respect to the fabrication process used – should the potential for luminescence efficiency be sacrificed in order to preserve the nanoscale morphology formed by GLAD, or vice versa?

Because the primary objective of this thesis was to fabricate luminescent chiral thin films that exhibit circularly polarized luminescence, the reliable nanoscale morphologies achievable with GLAD and evaporation were selected over the potential improvements in the luminescence characteristics offered by using sputtering and PLD with substrate heating. It should also be noted the studies by Jones *et al.* [4] and Bozse [5] both required post-deposition annealing to produce samples with strong luminescence, even though they heated their substrates during deposition. Thus, all of the Y_2O_3:Eu films fabricated in this work were deposited using electron beam evaporation onto unheated substrates, and a post-deposition annealing step was used as the sole thermal treatment that samples were subjected to during processing. While no efforts were taken to purposefully heat

the substrates during the deposition, radiant heating from the evaporation source may still lead to elevated substrate temperatures. However, at glancing angles, such radiant heating has been found to only cause elevated substrate temperatures of ~ 150°C [26], which should not be high enough to affect the luminescence or structural properties of the films.

Film depositions were carried out under high vacuum conditions (base pressure < 10^{-4} Torr) in deposition chambers (Fig 3.1) that held the center of the substrate chuck at a distance of 42 cm from the crucible. Initial tilted columnar thin film samples were fabricated with the aim of establishing a deposition process that produced films with strong enough luminescence characteristics to be detected with relative ease. The process parameters that were varied to determine an acceptable fabrication process included post-deposition annealing temperatures, europium content of the source material, and the oxygen content in the vacuum chamber during the deposition. Silicon and fused silica substrates were used in order to have samples on both a non-transparent (at visible wavelengths) and a transparent substrate, with both having thermal characteristics that would support high temperature processing. The source material used was either 4.0 wt% Eu-content Y_2O_3:Eu pellets or 5.6 wt% Eu-content powder. Oxygen pressures during the deposition were held to less than 2×10^{-4} Torr or less, because higher pressures would significantly degrade the performance of the electron beam gun.

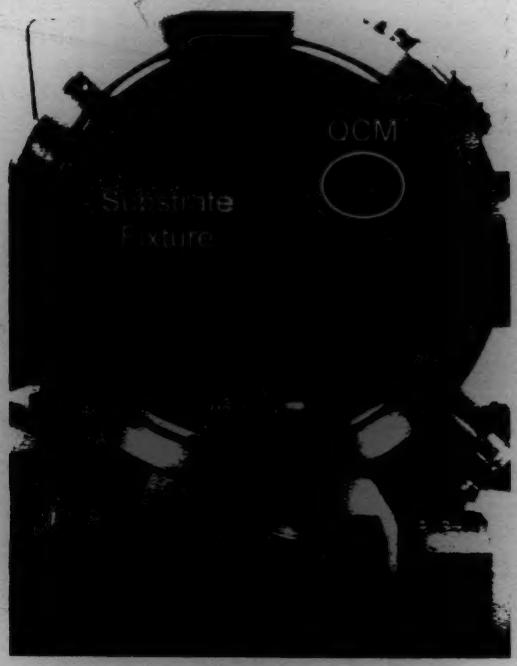

FIGURE 3.1

Deposition apparatus. A typical deposition system used in the fabrication of nanostructured Y_2O_3:Eu thin films is pictured with the substrate platform visible. The electron beam gun (not visible) is held in the lower chamber.

The source materials required significant pre-deposition conditioning by the electron beam. If the electron beam current was increased too quickly, explosive spitting of the source material would occur. In general, a 9 kV accelerating voltage was selected, and the current was slowly increased to 100 mA over the course of one hour in order to properly condition the source. Once conditioned, both source materials were found to sublimate easily under a 1.1 – 1.4 kW electron beam to obtain deposition rates of 10 – 30 Å/s, respectively, as measured by the quartz crystal microbalance (QCM). To accurately measure the deposition rate, the QCM was programmed with the density and z-factor for the deposited material. These values were not known for the source materials

used, so initial experiments used a density of 5.01 g/cm^3 and a z-factor of 1.00, as these are commonly listed in evaporation tables for Y_2O_3 [27]. Once an acceptable fabrication procedure had been developed, however, the density and z-factor were measured according to the procedure given in *Appendix A*. Also, because the material sublimated, or at best formed a localized melt, the electron beam had to be constantly swept across the source material during the depositions.

3.2 Photoluminescence Detection Apparatus

The apparatus used to detect the photoluminescence was carefully characterized to allow the measurement of the photoluminescent output in absolute radiometric units (Fig. 3.2). This apparatus was built by a fellow graduate student, Michael Taschuk, who helped obtain and analyze the photoluminescence data for the Y_2O_3:Eu films (i.e. the photoluminescence measurements in this chapter, and in *Chapter 4*).

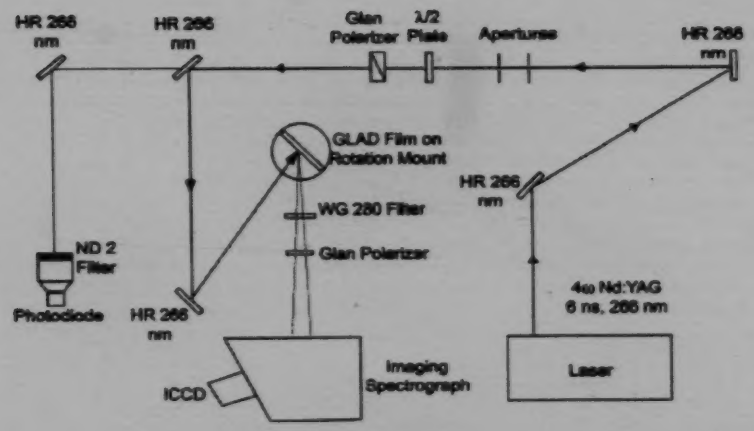

FIGURE 3.2

Schematic diagram of the photoluminescence detection apparatus. Laser pulses with a wavelength of 266 nm excited the photoluminescence from the nanostructured Y_2O_3:Eu thin films. The spectrograph and intensified charge coupled device (ICCD) detected the photoluminescent response of the samples.

The excitation source was the 266 nm line of a pulsed, twice frequency-doubled Nd:YAG laser (Big Sky Ultra). While no decay time measurements were performed in these studies, the use of a pulsed laser in this apparatus meant that the apparatus might be used in future for such measurements. The laser pulses were 6 ns long and were emitted at a repetition rate of 10 Hz. The energy of the beam delivered to the film was controlled by the rotational positions of the half waveplate and the Glan-Taylor polarizer. The energy was then monitored by the photodiode, which was calibrated using a calorimeter placed at the location of the film prior to testing of any of the samples. The photoluminescent output was detected by the spectrometer (Oriel MS260i) and the intensified charge coupled device (ICCD, Andor iStar DH720-25 mm). A 1200 lines/ mm grating was used to obtain high wavelength resolution for wavelengths near the known 611 nm wavelength luminescence of Y_2O_3:Eu. The spectrometer and ICCD

were calibrated using a mercury lamp, which produced known irradiances [28], and the spectral curves for the optics within the camera and spectrometer as obtained from the manufacturers, by calculating the fraction of light that arrives at the ICCD compared to that which arrives at the input slit of the spectrometer.. Additionally, the calibration was confirmed by placing a barium sulfate-coated aluminum plate at the sample location in the apparatus. The barium sulfate plate was a diffuse reflector, and should have acted as a Lambertian scattering source [29]. Thus, the intensity of the scattered laser light should have a cosine dependence on the viewing angle. A comparison of the observed scattering pattern from the barium plate to that of an ideal Lambertian yielded a confirmation of the calibration factor, because the beam energy incident upon the barium sulfate plate was simultaneously measured by the calibrated photodiode.

The calibration methods allowed the observed photoluminescence to be reported in absolute radiometric units, such as nJ Sr^{-1} cm^{-2} for time-integrated brightness, and nJ Sr^{-1} cm^{-2} nm^{-1} for time-integrated spectral brightness [29]. Time-integrated brightness values were obtained by integrating the detected signal over the wavelength range of interest (i.e over the photoluminescence peaks), after measuring the background signal in spectrally quiet regions and correcting for this background (the background signal was due to ambient light in the room that housed the detection apparatus). Figure 3.3 shows a typical photoluminescence spectrum obtained with this apparatus, as well as a typical plot of the time-integrated brightness versus the laser energy. The spectral region used to determine the background signal is also depicted in Fig. 3.3a. Estimates of the efficiency of the photoluminescence were obtained from the slopes generated in plots like Fig. 3.3b. These efficiency estimates were only useful for relative comparisons between samples. A reliable measurement of the amount of excitation light absorbed by the films was not obtained. This prevented the calculation of an absolute efficiency value.

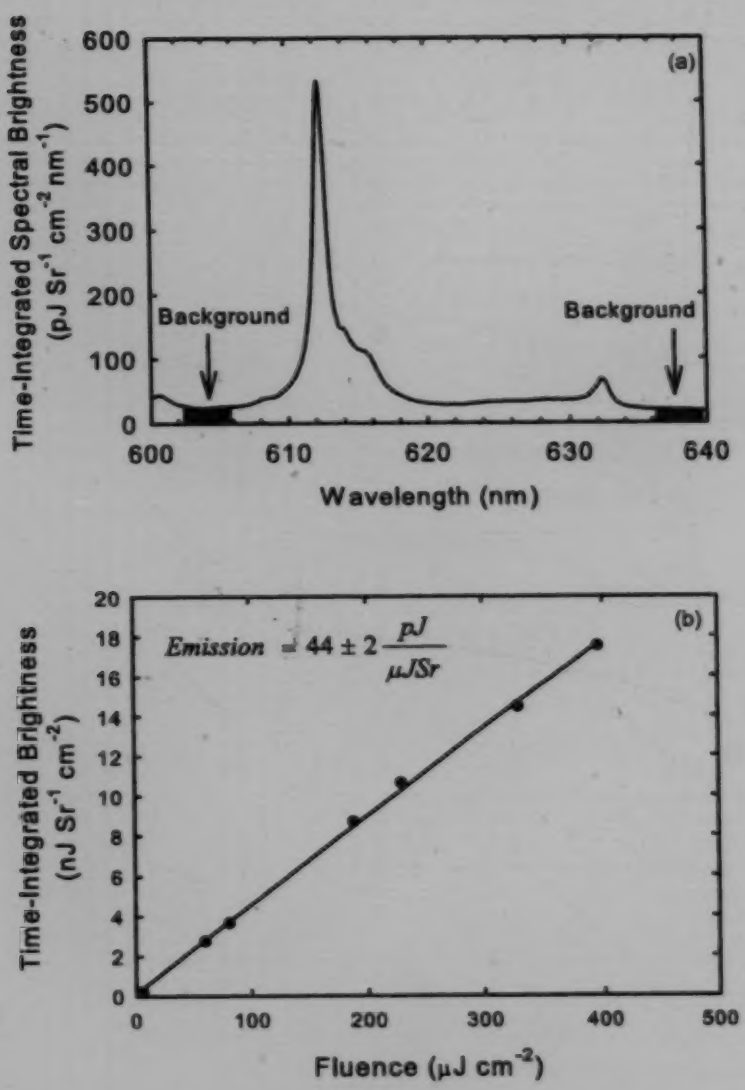

FIGURE 3.3

Typical photoluminescence data. An example of (a) a photoluminescence spectrum and (b) efficiency estimate curve obtained from a nanostructured Y_2O_3:Eu thin film are shown. The time-integrated spectral brightness was determined by wavelength-integrating the signal obtained for the main luminescence peak, and then correcting the obtained value for the background signal. The background signal was determined from the wavelength-integrated signal measured in spectrally quiet regions, such as those depicted in (a).

3.3 Post-deposition annealing

Following deposition, portions of each sample were treated to a high temperature annealing process in air. Published works on luminescent Y_2O_3:Eu thin films [1,4,5,12] have shown that annealing in air at temperatures greater than 800°C can result in significant increases in both the crystallinity of the films and the photoluminescence intensity. But, the effects that high temperatures annealing had upon the nanoscale morphology of the films were unknown. The nanoscale morphology of an as-deposited tilted columnar Y_2O_3:Eu is shown in Fig. 3.4a, and the photoluminescence spectra of the same sample is depicted in Fig. 3.5a. The as-deposited sample consisted of a series of fibrous tilted columns, and it yielded low levels of photoluminescence such that only the 611 nm wavelength photoluminescent peak could be resolved. To explore the effects of annealing on nanostructured Y_2O_3:Eu films, an initial process consisting of an 850°C air anneal for 10 hours was tested. The initial annealing process introduced only moderate structural changes in the nanoscale morphology of the films (Fig. 3.4). The annealed sample was less fibrous than the as-deposited one, and small nodules formed upon the tilted columnar structure likely related to some crystallization of the structure. However, the photoluminescence output of the annealed sample was greatly enhanced compared to the as-deposited film (Fig. 3.5). The photoluminescence peak at $\lambda = 611$ nm of the annealed film was approximately five times greater than for the as-deposited film. The lesser photoluminescence peaks of $^5D_0$-$^7F_2$ and $^5D_0$-$^7F_1$ transitions were only resolved for the spectra obtained from the annealed samples.

FIGURE 3.4

SEM images of a tilted columnar Y_2O_3:Eu thin film. A tilted columnar film is shown both (a) as-deposited and (b) after it has been annealed in air at 850 °C for 10 hours. Small nodules were present on the individual tilted columns of the annealed sample, but the two films showed little difference otherwise.

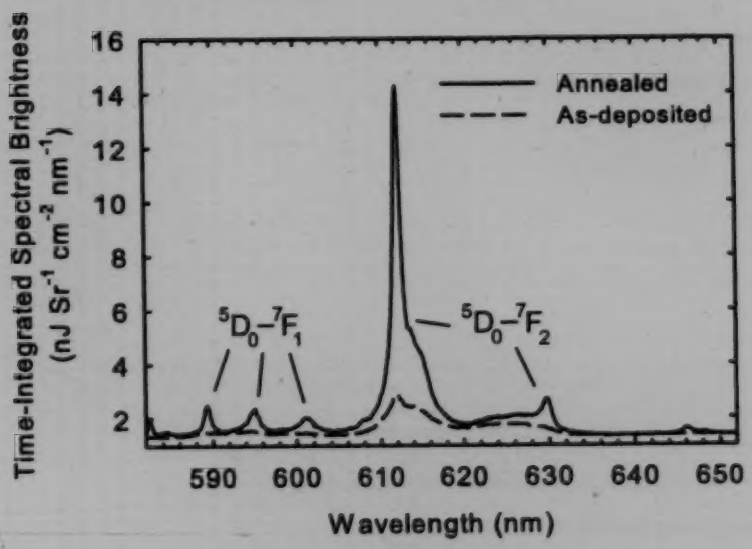

FIGURE 3.5

Photoluminescent spectra as-deposited and annealed samples. The measured photoluminescence spectra for a tilted columnar sample in the as-deposited and annealed states are shown. The annealed sample produced a significantly greater photoluminescent response.

Even higher annealing temperatures (temperatures up to ~ 1200°C have been reported) are known to yield samples that exhibit even stronger luminescence [4, 5, 12]. To explore the effects of increased annealing temperatures upon the nanoscale morphology, portions of a 1790 nm thick pillar and a 1100 nm thick chiral Y_2O_3:Eu film were subjected to one-hour long air anneals at temperatures between 900°C and 1100°C (at intervals of 50°C). These samples were then imaged through SEM, as shown in Fig. 3.6 and Fig. 3.7, respectively. Clearly, the changes to the nanoscale morphology became much more pronounced at higher annealing temperatures, as the individual structures agglomerated and lost definition. These results precluded the use of such temperatures for the ultimate goal of fabricating chiral Y_2O_3:Eu films capable of circularly polarized photoluminescence. Accordingly, the annealing process selected for the fabrication of subsequent samples consisted of a 10-hour air anneal at 850°C. Although annealing times longer than an hour were known [5] to provide little additional benefit to the photoluminescent output of the samples, a time of 10 hours was selected in order to allow direct comparisons between subsequent samples and the earliest samples fabricated.

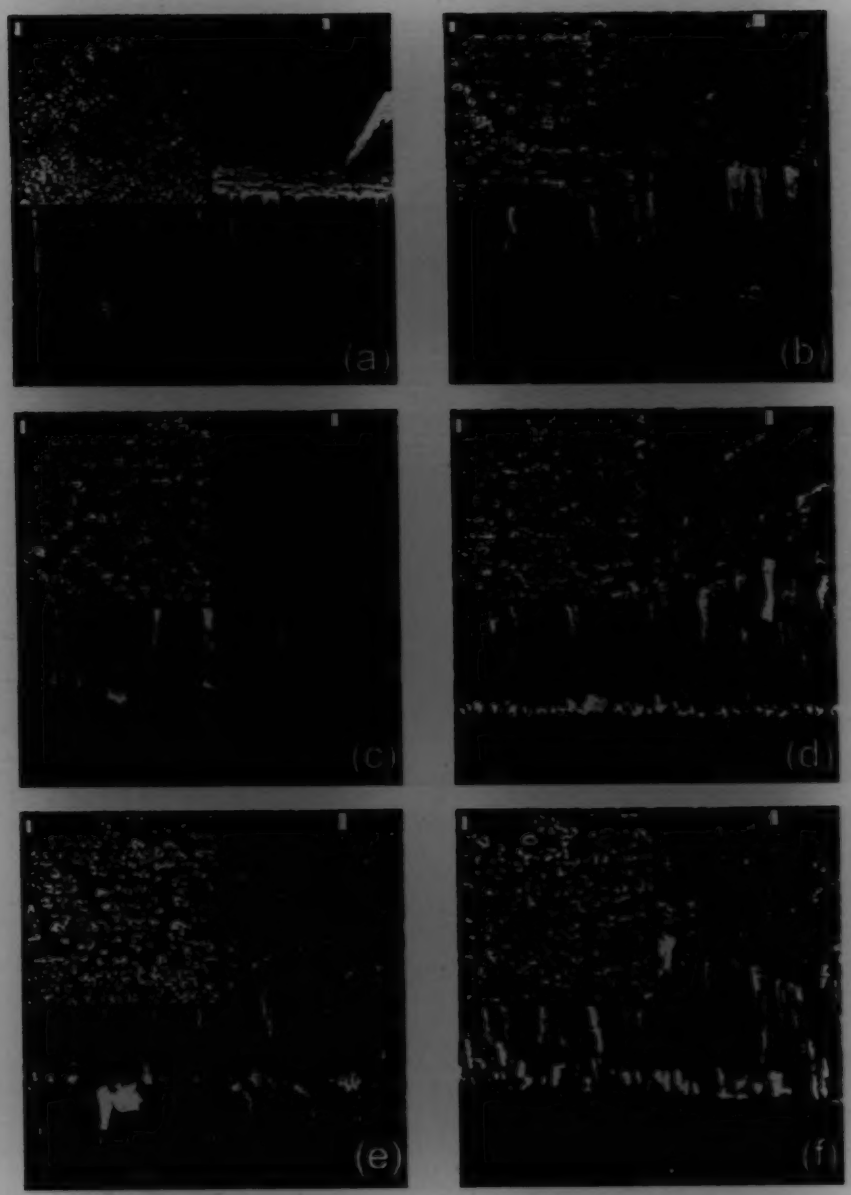

FIGURE 3.6

SEM images of a pillar film annealed at various temperatures. A 1790 nm pillar Y_2O_3:Eu thin film is shown (a) as-deposited, (b) annealed at 900°C, (c) annealed at 950°C, (d) annealed at 1000°C, (e) annealed at 1050°C, and (f) annealed at 1100°C. The annealing time was 1 hour in each case. Oblique and plan (inset) views are depicted and are magnified by 20,000 and 30,000 times, respectively.

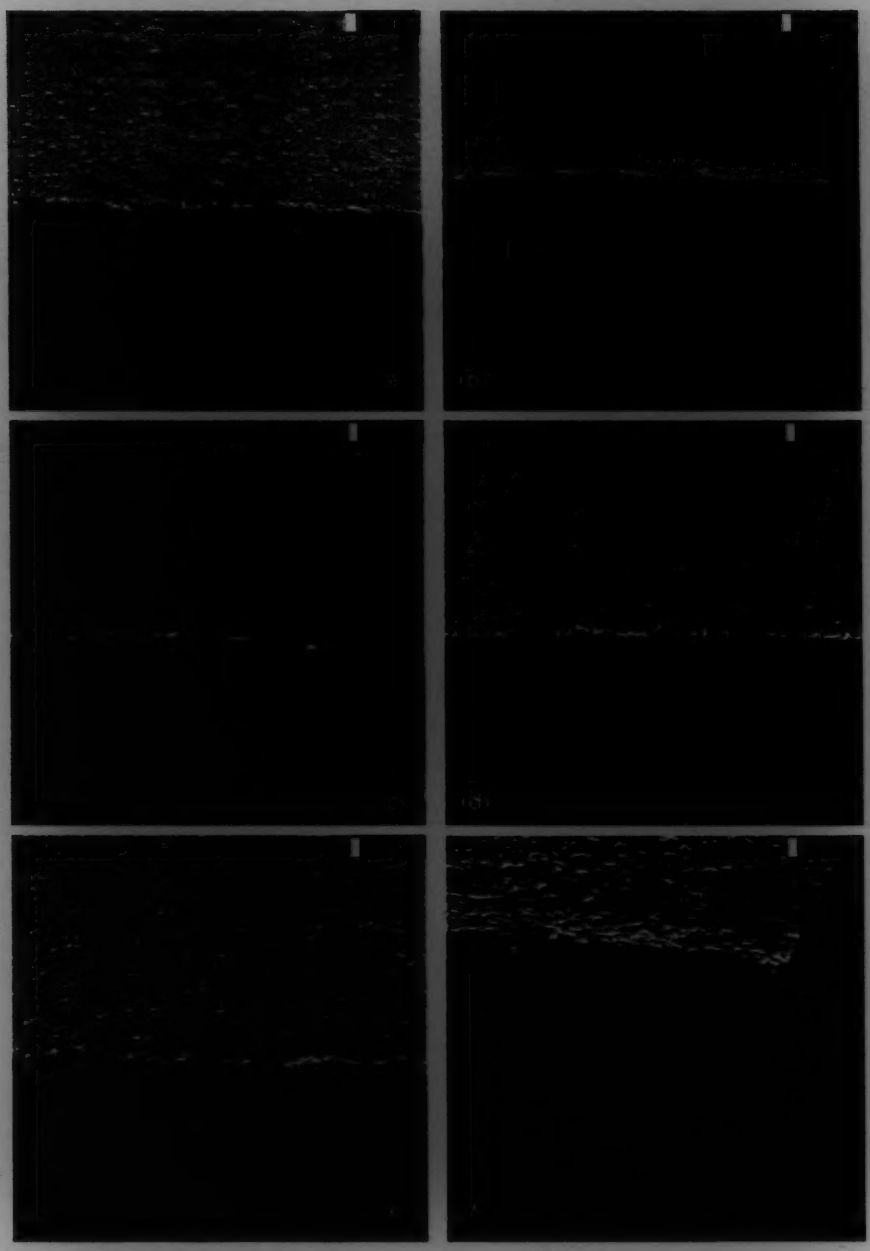

FIGURE 3.7

SEM images of a chiral film annealed at various temperatures. A 1100 nm chiral Y_2O_3:Eu thin film is shown (a) as-deposited, (b) annealed at 900°C, (c) annealed at 950°C, (d) annealed at 1000°C, (e) annealed at 1050°C, and (f) annealed at 1100°C. The annealing time was 1 hour in each case.

The changes brought on by the annealing process were explored further by X-ray diffraction (XRD) and X-ray photoelectron spectroscopy (XPS) measurements. These techniques were used to characterize the crystallinity and composition of the as-deposited and annealed forms of a number of nanostructured Y_2O_3:Eu films. XRD measurements were made on films with chevronic, pillar, and helical morphologies, and of a solid Y_2O_3:Eu film, all of which films were fabricated using the 5.6 wt% Eu source material. As mentioned in *Chapter* 2, Y_2O_3:Eu has the same cubic *C*-type crystal structure as un-doped Y_2O_3, since the Eu^{3+} dopants substitute for Y^{3+} ioms in the lattice [8]. XRD scans were obtained with a Rigaku Rotaflex XRD system with a thin-film camera attachment operated in θ-2θ mode. Figure 3.8 shows some representative XRD patterns that were obtained for as-deposited and annealed samples. The as-deposited samples showed slight peaks in the <222> direction of the measured XRD patterns, indicating that they were only slightly crystalline or nanocrystalline. The annealed samples, however, showed distinct peaks consistent with cubic crystal structure of Y_2O_3 as given by Joint Committee for Powder Diffraction Studies (JCPDS) card #41-1105 [5]. The XRD patterns formed by annealed nanostructured Y_2O_3:Eu films showed peaks in the same locations regardless of nanoscale morphology, as demonstrated in Fig. 3.9. As solid Y_2O_3:Eu films exhibited the same XRD patterns as nanostructured Y_2O_3:Eu films, it can be concluded that the nanoscale morphology of the film had no bearing on the crystal structure formed during the annealing process.

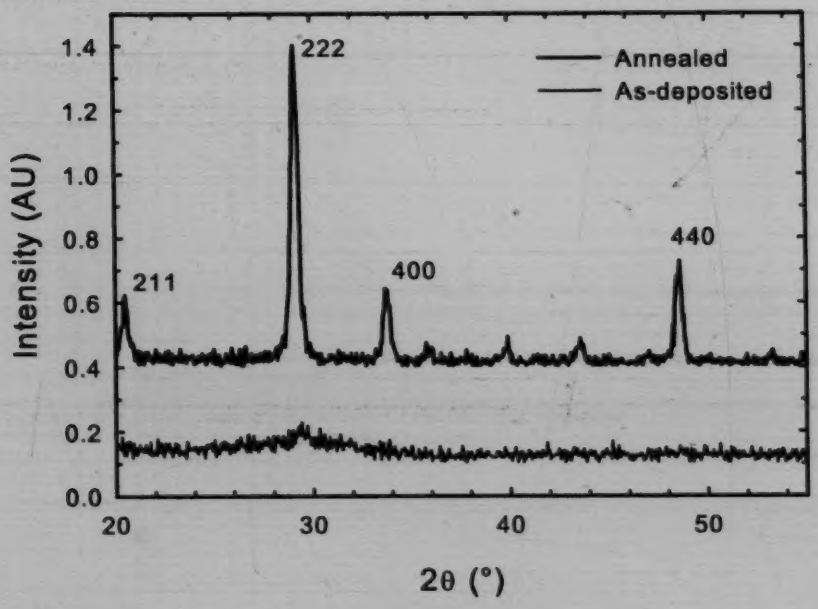

FIGURE 3.8

XRD patterns of a chiral Y_2O_3:Eu thin film before and after annealing. The as-deposited film was nanocrystalline, as indicated by the slight peak in the <222> direction. Following a 10-hour, 850°C anneal in air, the film produced an XRD pattern that was consistent with the cubic crystal structure of Y_2O_3.

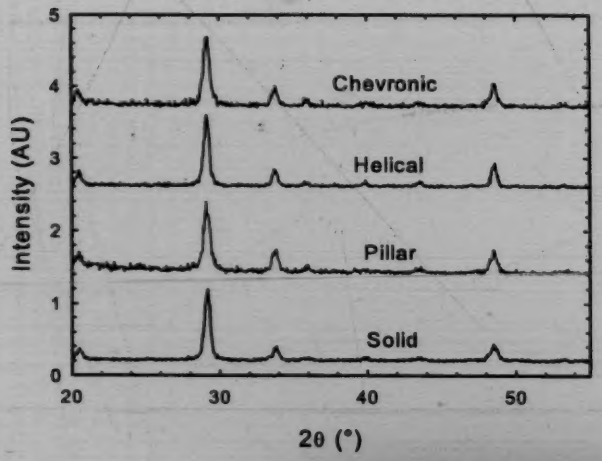

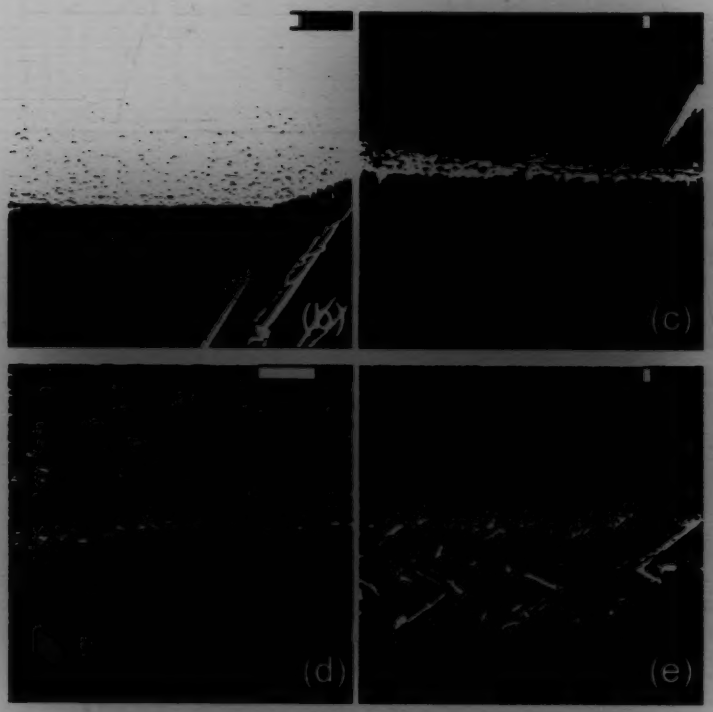

FIGURE 3.9

Comparison of XRD data and SEM micrographs for Y_2O_3:Eu thin films with differing nanostructural morphologies. The (a) XRD patterns (post-annealing) and SEM micrographs (as-deposited) of (b) solid, (c) pillar, (d) chiral, and (e) chevronic Y_2O_3:Eu thin films are displayed. The XRD patterns for all of the structures were all consistent with the cubic crystal structure of Y_2O_3.

The composition of some of the samples was characterized by XPS, both before and after annealing. XPS scans were obtained using a Kratos Axis 165 X-ray Photoelectron Spectrometer equipped with an ion gun for performing depth profiling. The ion gun was used for short time prior to acquiring the XPS spectra in order to sputter off any surface contamination present on the samples. Among the samples tested were a tilted columnar sample deposited from the 4.0 wt% Eu source material, and both as-deposited and annealed portions of a solid film and a pillar film (Table 3.1). Both the solid film and pillar film referred to in Table 3.1 were fabricated with the 5.6 wt% Eu source material.

TABLE 3.1

Determination of chemical composition of Y_2O_3:Eu films using XPS.

Sample Type	Source Stoichiometry	wt% Eu Doping in Source	at% Eu Doping in Film	wt% Eu Doping in Film
Annealed tilted columnar	$Y_{1.94}Eu_{0.06}O_3$	4.0	0.671	2.27
As-deposited solid	$Y_{1.914}Eu_{0.086}O_3$	5.6	0.714	2.94
Annealed solid	$Y_{1.914}Eu_{0.086}O_3$	5.6	1.33	4.28
As-deposited pillar	$Y_{1.914}Eu_{0.086}O_3$	5.6	0.556	2.57
Annealed pillar	$Y_{1.914}Eu_{0.086}O_3$	5.6	1.18	3.64

The XPS data showed an increased measure of europium for samples the annealed samples compared to the as-deposited ones. Because the annealing process could not have introduced additional europium into the films, the annealing process likely caused the europium to diffuse through the films and achieve a more even distribution over the entire thickness of the films. Other explanations involving the formation of Eu_2O_3 clusters in the nanostructures may also be possible. Also, the europium levels detected by the XPS measurements, and thus the europium concentrations, of the films were

consistently less than those of the source materials, regardless of whether 4.0 wt% Eu or 5.6 wt% Eu source materials were used. To explore the potential for europium depletion from the source material during evaporation, Eu_2O_3 films were evaporated so that the evaporation rates at a given e-beam power could be compared to those of the Y_2O_3:Eu source materials. This simple test showed that Eu_2O_3 films required ~ 0.3 kW less power than Y_2O_3:Eu to deposit thin films at a given deposition rate, confirming that europium depletion likely occurred during the source conditioning of the Y_2O_3:Eu evaporations..

The effects induced by the annealing process can be summarized as follows: a significant increase in luminescence is obtained, the films become polycrystalline, and the films seem to distribution of the europium dopants apparently changes. The crystallinity induced by the annealing process leads to an increase in the ratio between emission peak observed at 611 nm and the peak observed between 620 nm and 630 nm. The latter peak was known to result from a disordered or monoclinic nanocrystalline phase [13, 14, 17]. The improved crystallinity also allows for more efficient excitation of the europium ions via the charge transfer state. In amorphous or poorly crystalline Y_2O_3:Eu, the charge transfer state can overlap somewhat with both the excited state and the ground state, resulting in an increased occurrence of non-radiative processes [30].

3.4 Effect of the europium content of the source material

Samples were fabricated using source material with differing europium contents (either 4.0 wt% or 5.6 wt%). The europium content is known to strongly affect the photoluminescence intensity of Y_2O_3:Eu: low Eu levels provide too few luminescent centers to produce a strong luminescence output, while high Eu levels also result in poorly luminescent samples due to concentration quenching [30]. Europium levels of 4.0

– 5.3 wt% are known to result in the strongest luminescence output from Y_2O_3:Eu [31]. Thus, SEM imaging, photoluminescence characterization, and XPS (Table 3.1 above) were used to determine the effects that using the two different source materials had on the nanoscale morphology, photoluminescent output, and chemical composition of the nanostructured Y_2O_3:Eu films.

SEM imaging of samples deposited from both source materials revealed no major differences in the nanoscale morphologies of the deposited films (Fig. 3.10). The films both consisted of arrays of tilted columns. The tilted columns made from the 4.0 wt% Eu source material were somewhat broader and less fibrous that those obtained with the 5.6 wt% Eu source material. However, some of the differences could be attributed to the cleavage plane in Fig. 3.10 laying slightly outside of the deposition plane, so that the viewing angle was slightly different for the two images. The photoluminescent output (Fig. 3.11) was, however, much stronger (3.6 times) for the film deposited from the 5.6 wt% Eu source material than that of the 4.0 wt% Eu source material. The 5.6 wt% Eu source material sample was thicker (by ~ 300 nm) than the 4.0 wt% Eu source material sample, and this could have partially explained the increased photoluminescent response of the former. However, the photoluminescent response of Y_2O_3:Eu is highly dependent on the Eu doping level, so the data had to be considered in light of the XPS data presented previously in Table 3.2. The XPS data showed that a film deposited from the 4.0 wt% Eu source material only contained 2.27 wt% Eu following the annealing process, whereas a film deposited from the 5.6 wt% Eu source material contained 3.64 wt% Eu. Thus, samples deposited from the 5.6 wt% Eu source material were more likely to have an europium doping level that is close to the optimum of 4.0 – 5.3 wt% [31]. Therefore, the photoluminescence of samples deposited from the 5.6 wt% Eu source material would be expected to be higher.

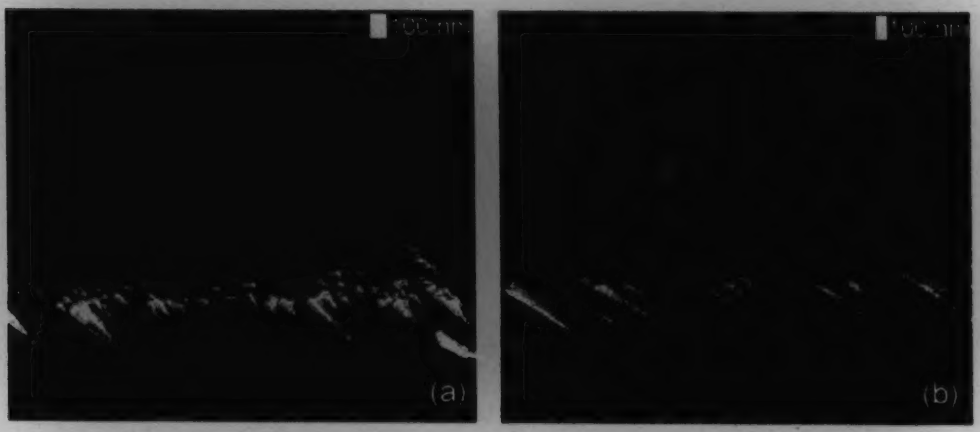

FIGURE 3.10

SEM images of tilted columnar Y_2O_3:Eu thin films fabricated from different source materials. Samples fabricated from (a) 4.0 wt% Eu source and (b) 5.6 wt% Eu source material are depicted. Note that the cleavage plane in (a) was not precisely in the deposition plane, as was the case for (b).

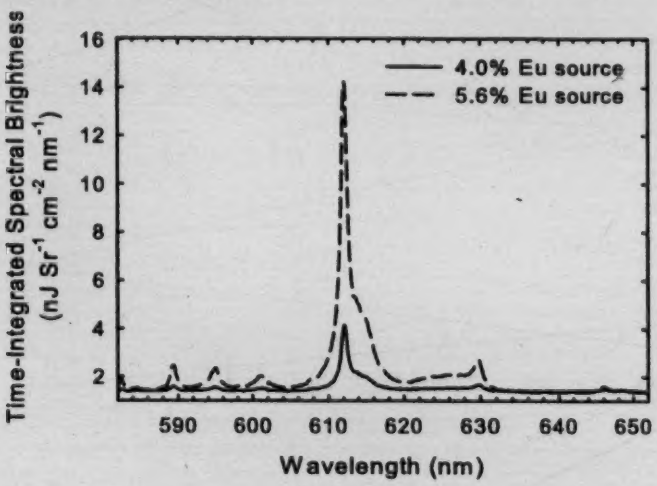

FIGURE 3.11

Photoluminescent spectra of samples fabricated from different Y_2O_3:Eu source materials. The photoluminescence spectra of samples fabricated from 4.0 wt% Eu source and 5.6 wt% Eu source are depicted. The photoluminescent response was significantly stronger from samples fabricated with 5.6 wt% Eu source material.

3.5 Effect of oxygen background during deposition

Solid Y_2O_3:Eu films deposited by PLD at high oxygen background pressures of a few hundred mTorr have been demonstrated to yield improved luminescence characteristics [4,6]. Samples were fabricated under differing vacuum conditions, to test the influence of the oxygen background pressure on the photoluminescence yielded by nanostructured Y_2O_3:Eu films. For this initial study, one sample was deposited in a chamber without oxygen added and at a deposition pressure of 4×10^{-5} Torr, while two additional samples were fabricated with oxygen added during the deposition to yield oxygen pressures of 1×10^{-4} Torr and 2×10^{-4} Torr. Of all of the parameters discussed in this chapter, the oxygen pressure during the deposition was most likely to affect the nanoscale morphology of the films. This is because the mean free path of the evaporated molecules decreases (as discussed in *Chapter 2*) at higher deposition pressures. Thus, the evaporated molecules undergo more collisions before reaching the substrate, and the angular distribution of the flux arriving at the substrate is larger as a result. In this work, however, varying the oxygen pressure during the deposition between $0.4 - 2 \times 10^{-4}$ Torr had no discernable effect on the nanoscale morphology of the films (Fig. 3.12).

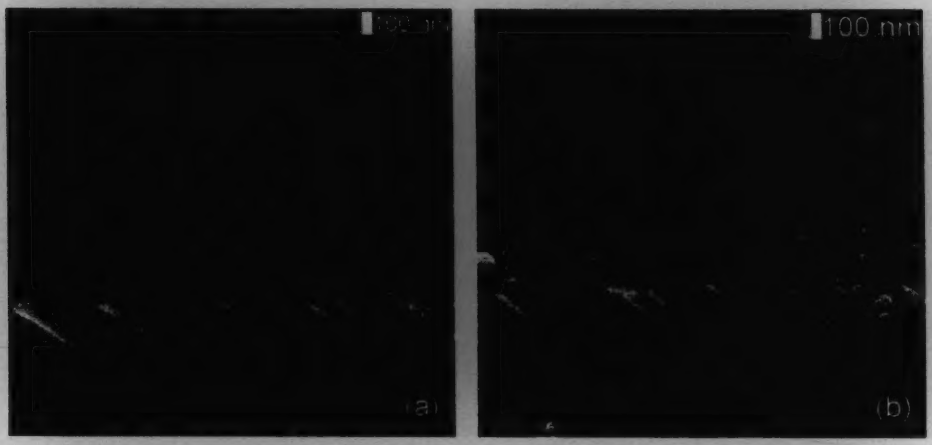

FIGURE 3.12

SEM images of tilted columnar Y_2O_3:Eu thin films fabricated under differing vacuum conditions. Samples deposited at pressures of (a) 4.0×10^{-5} Torr (without O_2 added during deposition) and (b) 2.0×10^{-4} Torr (with O_2 added during deposition) are depicted.

The effect of the background oxygen pressure in the vacuum chamber during film deposition on the photoluminescence output of the films is shown in Fig. 3.13. A minimum in the photoluminescent response was observed for the sample fabricated at an oxygen pressure of 1×10^{-4} Torr. The cause of this minimum has yet to be determined, however its existence corroborates the results of Jones *et al.* [7] who observed a photoluminescent intensity minimum for oxygen pressures near 1×10^{-4} Torr for PLD-based solid Y_2O_3:Eu films. Jones also observed much stronger photoluminescence for samples fabricated at oxygen pressures greater than 100 mTorr. Such high pressures were not compatible with e-beam evaporation, though, so no films could be fabricated at such pressures in this study. Thus, it seemed that introducing oxygen into the vacuum chamber during the deposition offered little benefit for the electron beam evaporation of photoluminescent Y_2O_3:Eu films.

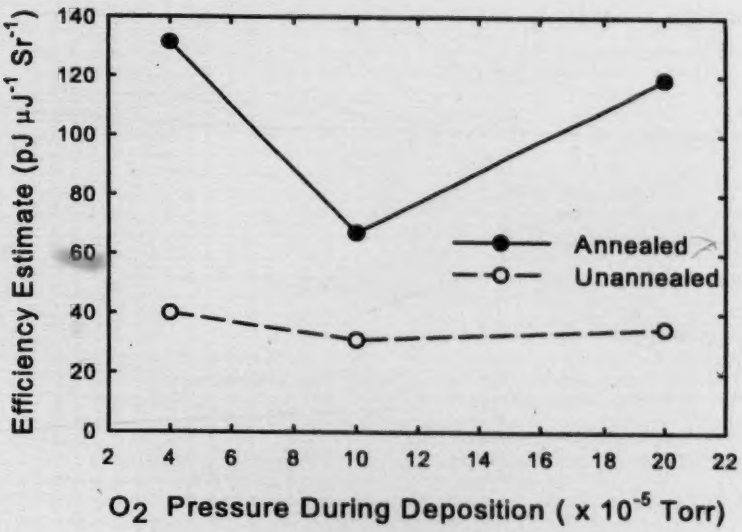

FIGURE 3.13

Effect of deposition pressure on the photoluminescence efficiency. Estimates of the photoluminescence efficiency for samples deposited at pressures of 4.0×10^{-5} Torr (without O_2 added), 1.0×10^{-4} Torr (with O_2 added) and 2.0×10^{-4} Torr (with O_2 added) were obtained to demonstrate the effect of deposition pressure on the photoluminescence emission. The efficiency estimates were obtained using the method described in Section 3.2.

3.6 Summary

The results obtained from the initial fabrication and characterization of nanostructured Y_2O_3:Eu thin films revealed some key considerations for establishing an acceptable evaporation-based fabrication procedure. It was vital that the procedure could ultimately be used for fabricating chiral Y_2O_3:Eu thin films with strong enough levels of photoluminescence to be tested for circularly polarized luminescence. High-temperature, post-deposition air annealing was found to substantially increase the

crystallinity of the films. Much stronger photoluminescent outputs were observed as a result of this crystallization of the film. Annealing in air at 850°C resulted in acceptable levels of degradation to the nanoscale morphology, however higher temperatures were found to significantly degrade the nanoscale morphology. Two different types of source material (4.0 wt% Eu content and 5.6 wt% Eu content) were tested. The 5.6 wt% Eu content source material yielded films with higher photoluminescent responses. This was because the 5.6 wt% Eu source yielded films with europium concentrations of ~ 3.5 – 4.5 wt% Eu, which were close to the optimal concentrations of 4.0 – 5.3 wt% Eu, while the 4.0 wt% Eu source material produced films with < 3 wt% Eu. The effect of introducing oxygen into the vacuum chamber during fabrication of the samples was also explored. It was determined that for the range of oxygen pressures suitable for electron beam evaporation, the use of an oxygen backfill offered no benefit, in terms of the photoluminescent output exhibited by the films.

Based on these findings, the fabrication process used for subsequent samples was established. This process involved the evaporation of Y_2O_3:Eu from the 5.6 wt% Eu source material onto silicon and fused silica substrates in a vacuum with no oxygen backfill. A post-deposition 10-hour 850°C anneal in air followed, in order to allow for some crystallization of the films. This process was used to fabricate all Y_2O_3:Eu films discussed henceforth.

References

1. W. W. Hansen and R. E. Myers, "Cathodoluminescence of thin films containing rare-earth oxides," *Applied Physics Letters*, **6**, 58 (1965).

2. V. Bondar, M. Grytsiv, A. Groodzinsky, and M. Vasyliv, "Cathodoluminescent characteristics and light technical parameters of thin film screens based on oxides and oxysulfides of rare earth materials," *SPIE Proceedings*, **2648**, 338 (1995).

3. X. Ouyang, A. H. Kitai, and R. Siegele, "Rare-earth-doped transparent yttrium silicate thin film phosphors for colour displays," *Thin Solid Films*, **254**, 268 (1995).

4. S. L. Jones, D. Kumar, K.-G. Cho, R. Singh, and P. H. Holloway, "Pulsed laser deposition of Y_2O_3:Eu thin film phosphors," *Displays*, **19**, 151 (1999).

5. E. J. Bozse, "Effect of temperature and microstructure on the luminescent properties of europium activated yttrium oxide," *Ph. D. dissertation*, University of California - San Diego (2003).

6. R. M. Ranson, E. Evangelou, and C. B. Thomas, "Modeling the fluorescent lifetime of Y_2O_3:Eu," *Applied Physics Letters*, **72**, 2663 (1998).

7. S. L. Jones, D. Kumar, R. K. Singh, and P. H. Holloway, "Luminescence of pulsed laser deposited Eu doped yttrium oxide films," *Applied Physics Letters*, **71**, 404 (1997).

8. K. G. Cho, D. Kumar, D. G. Lee, S. L. Jones, P. H. Holloway, and R. K. Singh, "Improved luminescence properties of pulsed laser deposited Eu:Y_2O_3 thin films on diamond coated silicon substrates," *Applied Physics Letters*, **71**, 3335 (1997).

9. K. G. Cho, D. Kumar, S. L. Jones, D. G. Lee, P. H. Holloway, and R. K. Singh, "Growth and characterization of Eu:Y_2O_3 thin-film phosphors on silicon and diamond-coated silicon substrates," *Journal of the Electrochemical Society*, **145**, 3456 (1998).

10. K. G. Cho, D. Kumar, P. H. Holloway, and R. K. Singh, "Luminescence behavior of pulsed laser deposited Eu:Y_2O_3 thin film phosphors on sapphire substrates," *Applied Physics Letters*, **73**, 3058 (1998).

11. G. A. Hirata, J. McKittrick, M. Avalos-Borja, J. M. Siquerios, and D. Devlin, "Physical properties of Y_2O_3:Eu luminescent films grown by MOCVD and laser ablation," *Applied Surface Science*, **113/114**, 509 (1997).

12. R. P. Rao, "Growth and characterization of Y_2O_3:Eu^{3+} phosphor films by sol-gel process," *Solid State Communications*, **99**, 439 (1996).

13. H. Eilers and B. M. Tissue, "Laser spectroscopy of nanocrystalline Eu_2O_3 and Eu^{3+}:Y_2O_3," *Chemical Physics Letters*, **251**, 74 (1996).

14. B. Bihari, H. Eilers, and B. M. Tissue, "Spectra and dynamics of monoclinic Eu_2O_3 and Eu^{3+}:Y_2O_3 nanocrystals," *Journal of Luminescence*, **75**, 1 (1997).

15. L. Sun, J. Yao, C. Liu, C. Liao, and C. Yan, "Rare earth activated nanosized oxide phosphors: synthesis and optical properties," *Journal of Luminescence*, **87 – 89**, 447 (2000).

16. G. Wakefield, E. Holland, P. J. Dobson, and J. L. Hutchinson, "Luminescence properties of nanocrystalline Y_2O_3:Eu," *Advanced Materials*, **13**, 1557 (2001).

17. W.-W. Zhang, M. Xu, W.-P. Zhang, M. Yin, Z.-M. Qi, S.-D. Xia, and C. Garapon, "Site-selective spectra and time-resolved spectra of nanocrytalline Y_2O_3:Eu," *Chemical Physics Letters*, **376**, 318 (2003).

18. T.-L. Phan, M.-H. Phan, N. Vu, T.-K. Anh, and S.-C. Yu, "Luminescent properties of Eu-doped Y_2O_3 nanophosphors," *Physica Status Solidi*, **201**, 2170 (2004).

19. J. Wan, Z. Wang, X. Chen, L. Mu, and Y. Qian, "Shape-tailored photoluminescent intensity of red phosphor Y_2O_3:Eu^{3+}," *Journal of Crystal Growth*, **284**, 538 (2005).

20. K. Robbie and M. J. Brett, "Sculptured thin films and glancing angle deposition: growth mechanics and applications," *Journal of Vacuum Science and Technology A*, **15**, 1460 (1997).

21. J. C. Sit, D. Vick, K. Robbie, and M. J. Brett, "Thin-film microstructure control using glancing angle deposition by sputtering," *Journal of Materials Research*, **14**, 1197 (1999).

22. D. Vick, Y. Y. Tsui, M. J. Brett, and R. Fedosejevs, "Production of porous carbon thin films by pulsed laser ablation," *Thin Solid Films*, **350**, 49 (1999).

23. B. Dick, "Properties and growth of thin films produced by glancing angle deposition," *Ph. D. dissertation*, University of Alberta (2003).

24. S. Dew, T. Smy, and M. J. Brett, "Step coverage, uniformity, and composition studies using integrated vapour transport and film-deposition models," *Japanese Journal of Applied Physics*, **33**, 1140 (1994).

25. V. C. Venugopal and A. Lakhtakia, "Axial excitation of a nonlinear dielectric TFHBM slab: second harmonic generation," *Proceedings of Bianisotropics 1997*, Glasgow, 73 (1997).

26. M. Seto, "Mechanical response of microspring thin films," *Ph. D. dissertation*, University of Alberta (2004).

27. *Material Evaporation Guide*, Inficon, available via www.inficon.com/en.

28. J. Reader, C. J. Sansonetti, and J. M. Bridges, "Irradiances of spectral lines in mercury pencil lamps," *Applied Optics*, **35**, 78 (1996).

29. M. Born and E. Wolf, *Principles of Optics*, Cambridge University Press, Cambridge (1999).

30. G. Blasse and B. C. Grabmaier, *Luminescent Materials*, Springer-Verlag, Berlin (1994).

31. L. Ozawa, *Cathodoluminescence, Theory and Application*, VCH Publishers, Weinheim (1990).

CHAPTER 4
Optical characterization of nanostructured Y_2O_3:Eu thin films

Chapter 3 reviewed the progress achieved in fabricating nanostructured Y_2O_3:Eu thin films by GLAD, and yielded an acceptable fabrication procedure capable of reliably producing luminescent nanostructured Y_2O_3:Eu thin films. This chapter discusses the optical characterization techniques that were used to further characterize luminescent nanostructured Y_2O_3:Eu thin films. The studies presented here include the determinination of the principal indices of refraction of nanostructured Y_2O_3:Eu thin films, and the measurement of the polarization state of the photoluminescent emission from nanostructured Y_2O_3:Eu thin films. The optical characterization of helical Y_2O_3:Eu thin films completes the work with Y_2O_3:Eu thin films discussed here. The initial motivation for fabricating nanostructured luminescent thin films fabricated by GLAD was to explore the potential for fabricating chiral luminescent thin films that emitted light with some degree of circular polarization, and chiral Y_2O_3:Eu films were demonstrated to do so.

4.1 Optical characterization methods

The methods used in the optical characterization studies of the Y_2O_3:Eu thin films included variable angle spectroscopic ellipsometry (VASE), transmission Mueller matrix ellipsometry, and Stokes polarimetry. VASE analysis was used to determine the principal indices of refraction of tilted columnar Y_2O_3:Eu thin films. Transmission Mueller matrix ellipsometry allowed the observation of the transmittance-mode manifestation of the circular Bragg phenomena exhibited by chiral Y_2O_3:Eu thin films. Stokes polarimetry was combined with photoluminescence measurements to ascertain the polarization state of light emitted by chevronic and chiral Y_2O_3:Eu thin films. These are established techniques that have been reliably used in the literature for measuring quantities such as the optical constants [1 – 8] and the polarization of light transmitted [9] by or emitted from a sample [10 – 14]. A brief overview of each technique will be given here.

4.1.1 Variable-angle spectroscopic ellipsometry

Tilted columnar films are the simplest morphology of nanostructured films to fabricate with GLAD, and are known to be biaxial [4 – 6, 8], exhibiting three principal indices of refraction (Fig 4.1). Knowledge of the principal indices is useful for designing and fabricating optical coatings based upon nanostructured films fabricated with GLAD. Typically, ellipsometric methods have been used to determine the principal indices of refraction of tilted columnar thin films [5, 6, 8]. Because the films discussed in *Chapter 3* were the first nanostructured Y_2O_3:Eu films fabricated by GLAD, no prior studies of the principal indices of refraction of tilted columnar Y_2O_3:Eu films existed.

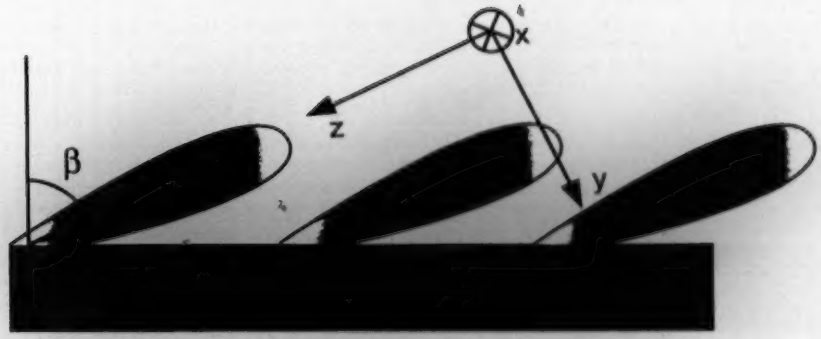

FIGURE 4.1

Principal indices of refraction of tilted columnar thin films. The orientation of the principal indices of refraction of tilted columnar thin films are depicted. Two indices exist within the deposition plane with one being parallel to the tilted columns, and the other perpendicular to the tilted columns. The final index is parallel to the substrate, but perpendicular to the deposition place.

Ellipsometry is a polarization-based measurement technique that involves the determination of two parameters, Ψ and Δ, that are related to the ratio of the complex Fresnel reflection coefficients

$$\tan(\Psi)e^{i\Delta} = \frac{r_p}{r_s} \tag{4.1}$$

Because ellipsometry measures the ratio of two quantities it can produce more precise and accurate data than simple intensity-based optical measurements [2, 3]. By obtaining ellipsometric measurements for various angles of incidence and over a large spectral region, the sensitivity of ellipsometric measurements to multiple parameters can be improved. Such a scheme is called variable angle spectroscopic ellipsometry (VASE) and it enables the simultaneous determination of a sample's thickness, optical constants, and numerous other parameters related to the optical constants [2, 3, 7, 8]. However, the

ellipsometric measurement does not directly yield these data because it only measures the ellispometric ratio, r_p/r_s. The desired parameters are instead extracted from the ellipsometric data through a model-based analysis procedure [2, 3]. One develops a model for the optical structure of the sample that is being examined, based on what is known regarding the materials present in the sample. This can consist of the optical constants of the materials if they are known, or of parametric dispersion models, such as a Cauchy model or Tauc-Lorentz oscillator model [15]. A computerized transfer matrix approach can then be used to calculate the ellipsometric ratio of the model, yielding generated data that can be compared to the experimental data measured by the ellipsometer. Iterative non-linear regression via the Marquardt-Levenberg algorithm [16] can then vary the model to produce a best fit between the generated data and the measured data. The mean-squared error (MSE) between the two sets of data is used to determine the quality of a given fit [2]. By exploring a wide range of potential parameters for a given model, a unique best fit can eventually be determined. Once a unique fit is obtained, the parameters that were being investigated can then be extracted from the model. Other types of external data, such as SEM-based thickness measurements, can also be compared to the model and used to guide the search for a unique fit [2].

These methods are well-established and used in a number of industrial metrology applications [1 – 3]. They have also been applied to the analysis of GLAD-fabricated samples [7, 8, 17 – 18]. Analysis based on the standard ellipsometric ratio [7, 17, 18] and on the measurement of the Mueller matrix [7] of a sample have both been used with GLAD films. However, the ellipsometric ratio approach assumes that the reflected light is completely polarized [3], which is not necessarily true for reflection from GLAD-fabrication samples. This is because the column sizes and porosities of GLAD films

lead to scattering and depolarization effects [3, 8]. Hence, the Mueller matrix approach can also be used. The Mueller matrix is a 4 × 4 matrix that relates the input and output polarizations states of light incident upon a sample, even if the polarization states are partially polarized, [10]. The input and output polarization states for the Mueller matrix are described by the Stokes parameters:

$$\begin{aligned} S_0 &= \langle E_{0x}^2 \rangle + \langle E_{0y}^2 \rangle, \\ S_1 &= \langle E_{0x}^2 \rangle - \langle E_{0y}^2 \rangle, \\ S_2 &= 2\langle E_{0x} E_{0y} \cos(\delta) \rangle, \\ S_3 &= 2\langle E_{0x} E_{0y} \sin(\delta) \rangle, \end{aligned} \tag{4.2}$$

where E_{0x} and E_{0y} are the electric field amplitudes along the x and y axes and δ is the phase difference. S_0 represents the total light intensity, while S_1, S_2, and S_3 represent the degree of linear horizontal (or vertical) polarization, linear polarization at +45° (or –45°), and RCP (or LCP), respectively. Mueller matrix data can be acquired by ellipsometers that are equipped with a means of producing circularly polarized light, in addition to the ability to produce the linearly polarized light used in all ellipsometric measurements. This data can be analyzed with the model-based methods outlined above. Parameters such as the principal indices of refraction, the thickness, the column tilt angle, and the porosity of tilted columnar films can be simultaneously determined in this manner [8, 18].

4.1.2 Transmittance-mode Mueller matrix ellipsometry

To explore the potential for fabricating chiral Y_2O_3:Eu thin films that emit partially circularly polarized light via photoluminescence, the spectral location of the circular

Bragg phenomenon produced by the chiral structure of the film must coincide with the emission band of Y_2O_3:Eu. The spectral location of the circular Bragg phenomena of chiral thin films can be determined using transmittance-mode Mueller matrix ellipsometry. To do so, a variable angle spectroscopic ellipsometer is used to perform normal incidence transmission and Mueller matrix measurements. The ellipsometer used in the work (VASE, J.A. Woollam Co., Inc.) can measure the first three rows of the transmission Mueller matrix [8, 9]. However, the ellipsometer automatically sets the m_{11} value to unity for all wavelengths to simplify the data acquistion. The m_{11} element of the Mueller matrix simply represents the overall transmittance of the system being studied. Thus, the actual values of m_{11} are determined by separate measurements of the transmittance of *p*- and *s*-polarized light (Eq. 4.3) [9, 10].

$$m_{11}(\lambda) = \frac{1}{2}[T_s(\lambda) + T_p(\lambda)] \tag{4.3}$$

This m_{11} value could then be used with the m_{14} element of the Mueller matrix to determine the transmittance of LCP and RCP light.

$$\begin{aligned} T_{LCP}(\lambda) &= m_{11}(\lambda) - m_{14}(\lambda) \\ T_{RCP}(\lambda) &= m_{11}(\lambda) + m_{14}(\lambda) \end{aligned} \tag{4.4}$$

From T_{LCP} and T_{RCP}, the selective transmittance of circularly polarized light is readily determined, providing a clear indication of the presence of circular Bragg phenomena.

4.1.3 Stokes polarimetry

The polarization state of light emitted by chiral luminescent thin films was measured by including a quarter waveplate and a Glan-Taylor polarizer in the photoluminescence detection apparatus described above, as depicted in Fig. 4.2. In such an arrangement, the intensity observed by the spectrometer is expressed as [8]:

$$I = \frac{1}{2}\left(S_0 + S_1\cos(2\psi) + S_2\sin(2\psi)\cos(\Delta) + S_3\sin(2\psi)\sin(\Delta)\right) \quad (4.5)$$

where S_N are the Stokes parameters defined in Eq. 4.1, ψ is the angular position of the polarizer axis, and Δ is the retardance present in the beam path. The photoluminescence output is then measured for various values of ψ both with the quarter waveplate in the beam path with its fast axis oriented at $\pm 45°$ to the polarizer axis (i.e. $\Delta = 90°$, ideally), and without the quarter waveplate present (i.e. $\Delta = 0°$, ideally).

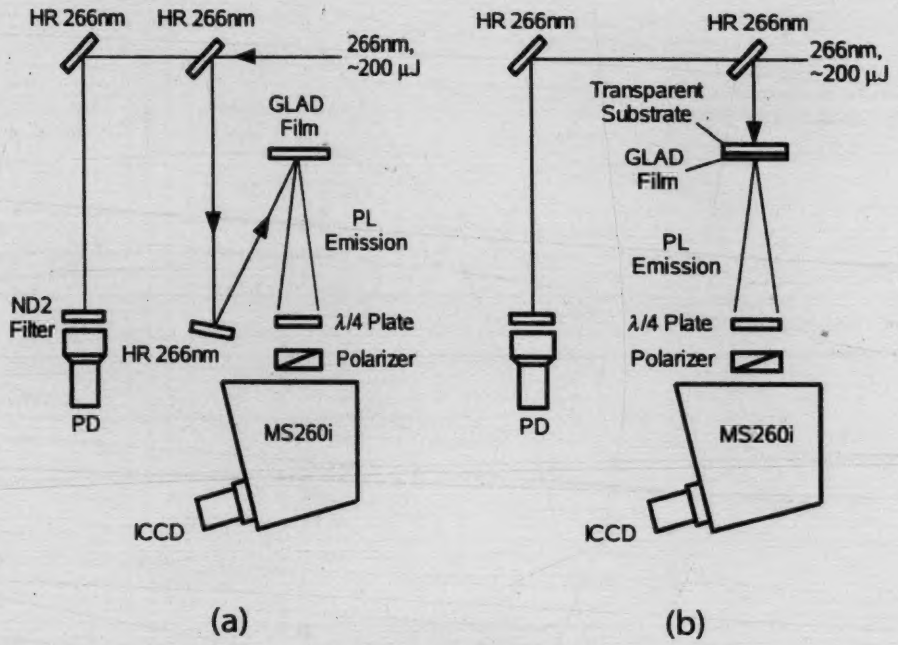

FIGURE 4.2

Schematic diagram of the photoluminescence and Stokes polarimeter apparatus. The apparatus can be adjusted to accommodate (a) samples on reflective (i.e. silicon) substrates, and (b) samples on transparent (i.e. fused silica) substrates.

For the experiments discussed below, the measured data were fit to Eq. 4.5. The fitting process was also used to correct for the polarization-sensitive reflectance of the grating in the spectrometer by including a factor in Eq. 4.5 to account for the grating. This additional factor was determined by consulting the polarization-sensitive reflectance curves for the grating, as provided by the manufacturer. An example of the data is given in *Appendix B*. From the best fit values of S_N, figures of merit for the polarization behaviour of the films were obtained. These figures of merit were the degree of polarization, ρ, and the degree of circular polarization, ρ_c:

$$\rho = \frac{\sqrt{S_1^2 + S_2^2 + S_3^2}}{S_0}$$

$$\rho_c = \frac{I_L - I_R}{I_{Total}} = \frac{-S_3}{S_0}. \qquad (4.6)$$

The dissymmetry factor, g_e [19], is an additional figure of merit commonly used in the literature to quantify the degree of circular polarization. However, the definition of this factor is such that it simply amounts to twice the value of ρ_c. In the data presented here, ρ and ρ_c will be used exclusively.

4.2 Determination of the optical constants of nanostructured Y_2O_3:Eu thin films

To determine the optical constants of tilted columnar Y_2O_3:Eu thin films, the ellipsometric techniques and the accompanying analysis methods described above were applied. This was done with the assistance of a fellow graduate student, James Gospodyn, who specializes in ellipsometric methods for studying GLAD films. The principal indices of refraction, porosity, and column tilt angle, β, of the tilted columnar Y_2O_3:Eu thin films listed in Table 4.1 were determined in this way. The measured data was obtained with a variable angle spectroscopic ellipsometer (VASE, J.A. Woollam Co., Inc.). The first three rows of the Mueller matrix were measured for angles of incidence in the range of 30 – 75°, and for wavelengths over the range of 300 – 1800 nm for each of the as-deposited films in Table 4.1.

TABLE 4.1

Tilted Columnar Y_2O_3:Eu films fabricated for characterizing the optical constants.

Sample	Nanostructure Type	Deposition Angle (°)	Thickness (nm)
A	Solid	0	678
B	Tilted Columnar	60	990
C	Tilted Columnar	65	998
D	Tilted Columnar	70	928
E	Tilted Columnar	75	991
F	Tilted Columnar	80	878
G	Tilted Columnar	85	882

Because the optical constants of solid Y_2O_3:Eu thin films deposited by the fabrication procedure described in *Chapter 3* were not known, the ellipsometer data acquired for the solid film was analyzed first. The model used for the analysis simply consisted of the silicon substrate and a Lorentz oscillator layer that was to serve as the Y_2O_3:Eu layer (Fig. 4.3). For the oscillator layer, the imaginary part of the complex dielectric constant, $\varepsilon(\omega)=\varepsilon_1(\omega)+i\varepsilon_2(\omega)$, was given by Eq. 4.7. The real part can then be determined from the integration of the Kramers-Kronig relation [20] for the imaginary part.

$$\varepsilon_2(\omega) = \sum_{j=1}^{m} \frac{A_j C E_j}{(E^2 - E_j^2)^2 + (C E_j)^2} \qquad (4.7)$$

The best fit to the experimental data was obtained for a single oscillator (m = 1) with an energy (E_j) of 4.92 eV, an amplitude (A) of 8.29 eV^2, and broadening (C) of 0.187 eV. The fitting process was performed by the WVASE 32 software package [21] provided with the VASE instrument used, which used the Marquardt-Levenberg algorithm [16] to minimize the MSE between the model-generated data and the measured data. The MSE obtained was rather high (~ 25), though this may have been due to the presence of an index gradient in the sample [8]. However, SEM imaging of the sample confirmed that the VASE analysis returned an accurate thickness for the Y_2O_3:Eu layer. The VASE

analysis determined the thickness of the solid Y_2O_3:Eu layer to be 678 nm, while the SEM imaging yielded a value of 681 nm.. Also, the fitting process used to determine the final model parameters was performed for a wide-variety of initial parameter values, and the final model parameters reported above were repeatedly obtained. Thus, the model seemed to provide a unique fit to the experimental data, and was used to determine the index of refraction of evaporated Y_2O_3:Eu films as a result (Fig. 4.4). The mean squared error between the data generated by the model and the data measured by the VASE was ~ 25 for the solid film. Thus, future work may aim to incorporate additional parameters in the model, such as an index gradient, in order to further improve the fit of the data.

The principal indices of refraction, porosity, and column tilt angle of the nanostructured Y_2O_3:Eu films listed in Table 4.1 were determined by modeling spectroscopic Mueller matrix data acquired for each of the samples. The Lorentz oscillator model established above served as the starting point for developing appropriate models. Each sample was modeled as a mixture of the solid Y_2O_3:Eu model and voids using the Bruggeman effective medium approach (Fig. 4.5) [22]. The model also treated the tilted columnar films as biaxial, in accordance with previous studies [4 – 6, 8]. This was achieved by adding a biaxial layer, and then coupling its optical properties to the Bruggeman effective medium layer. The use of these two coupled layers enabled the determination of the thickness, column tilt angle, porosity, and principal indices of refraction. The MSE values obtained for these tilted columnar films were higher (> 40) than the MSE obtained for the solid film (~ 25). It has been suggested that the scattering from GLAD films may cause the high MSE values that tend to be obtained when modeling some materials. This is suggested by the fact that MSE values have been observed to be higher for materials with higher indices of refraction, and the difference between the generated and experimental data is higher at lower wavelengths [23].

FIGURE 4.3

Optical layer model of a solid Y_2O_3:Eu film. The optical properties of the Y_2O_3:Eu film were modeled with a Lorentz oscillator.

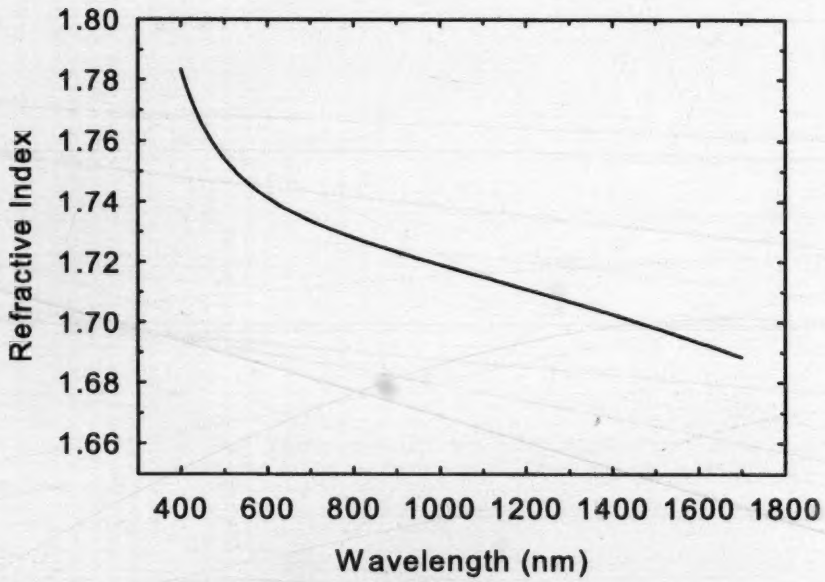

FIGURE 4.4

Dispersion of the index of refraction of a solid Y_2O_3:Eu film. The film was 670 nm thick. The index monotonically decreased at higher wavelengths.

To establish that the models still provided unique fits, the parameters yielded by the VASE analysis were again compared to values obtained from SEM images. The column tilt angle was one parameter that was determined both by VASE analysis and SEM imaging (Fig. 4.6), and the column tilt angles measured by VASE and SEM analysis were within ~ 4.5° of each other, on average, though, the SEM data systematically produced higher values for the column tilt angles. Neither the VASE data nor the SEM data produced column tilt angle behavior that was a good fit to the tangent rule [24] or Tait's rule [25]. Nonetheless, both sets of measured β values showed a trend with increasing deposition angle that was more similar to Tait's rule than to the tangent rule. The lack of fit between the measured column tilt angles and the tangent rule was expected, as the tangent rule is a poor predictor of β for $\alpha > 50°$, since the tangent rule expression allows for $\beta = 90°$ at $\alpha = 90°$. The lack of fit between Tait's rule and the column tilt angle data was due, in part, to the assumption used in the derivation of Tait's rule that the film consists of an ideal array of uniform and parallel tilted columns [4,12]. The porosity values obtained from the VASE data were also compared to the porosity predicted by the density formulation of Tait's rule (Fig 4.7):

$$porosity = 1 - d = 1 - \frac{2\cos\alpha}{1+\cos\alpha} \tag{4.8}$$

where d is the relative density. Again, the experimental data did not fit Tait's rule quantitatively, but did follow the same qualitative trend predicted by Tait's rule. Similar discrepancies between measured values and Tait's rule have been in the literature [8, 18, 25].

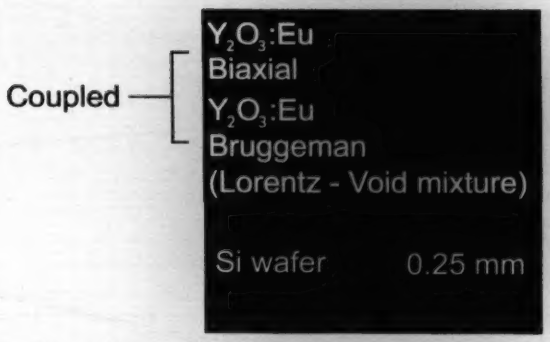

FIGURE 4.5

Optical layer model of a tilted columnar Y_2O_3:Eu film. The porous nature of the tilted columnar film was accounted for by the Bruggeman effective medium. The biaxial nature and orientation of the film was accounted for by a biaxial model that was coupled to the Bruggeman layer so that the two layers shared the same optical properties.

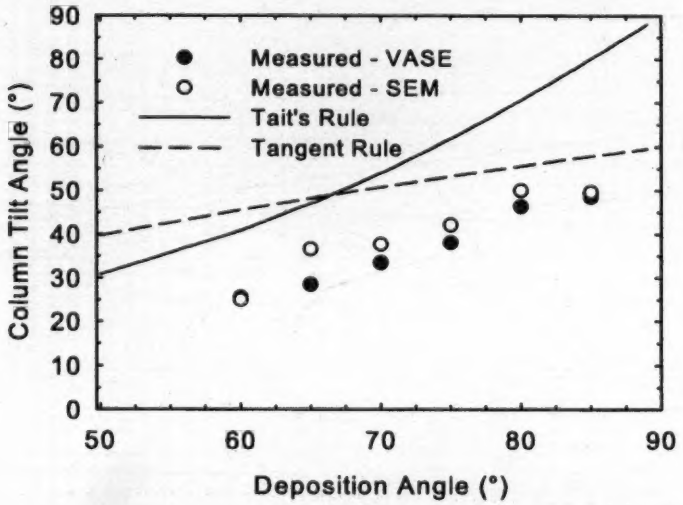

FIGURE 4.6

Variation of the column tilt angle of tilted columnar Y_2O_3:Eu thin films with deposition angle. The column tilt angles were determined from both section view SEM images and VASE analysis. The measured data were similar for both techniques, but they did not fit either the tangent rule or Tait's rule.

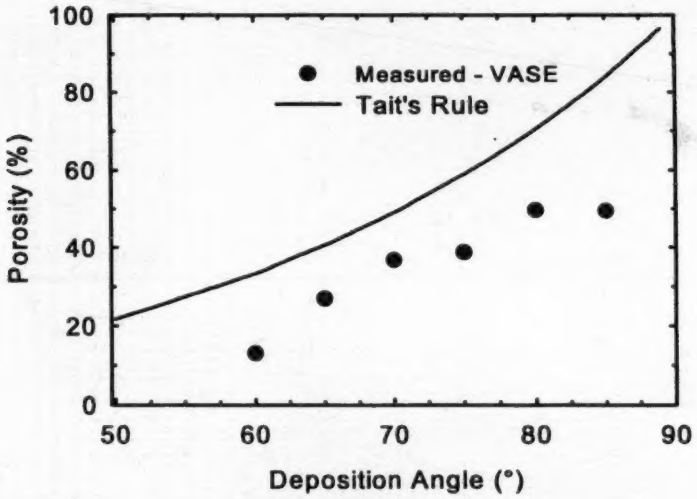

FIGURE 4.7

Variation of the porosity of tilted columnar Y_2O_3:Eu thin films with deposition angle. The porosities of the tilted columnar films were determined through VASE analysis. The measured values were not a good fit to Tait's rule for porosity, however, they do follow its trend. No error bars are shown because the 90% confidence limits calculated in the VASE analysis were smaller than the data symbols in the plot.

The principal indices of the tilted columnar samples were the key values determined by the VASE analysis. Examples of these indices are shown in Fig. 4.8. The principal indices decreased for increasing wavelengths. The principal indices (as defined in Fig. 4.1) followed the relation $n_y<n_x<n_z$, which was expected for this type of biaxial medium [5, 6, 8]. The principal indices were also found to decrease with deposition angle (Fig. 4.9) because the films were more porous when fabricated at higher deposition angles. The average refractive index for the sample deposited at $\alpha = 85°$ was found to be 1.36, which was a 22% decrease from the refractive index of 1.74 measured for the solid Y_2O_3:Eu film.

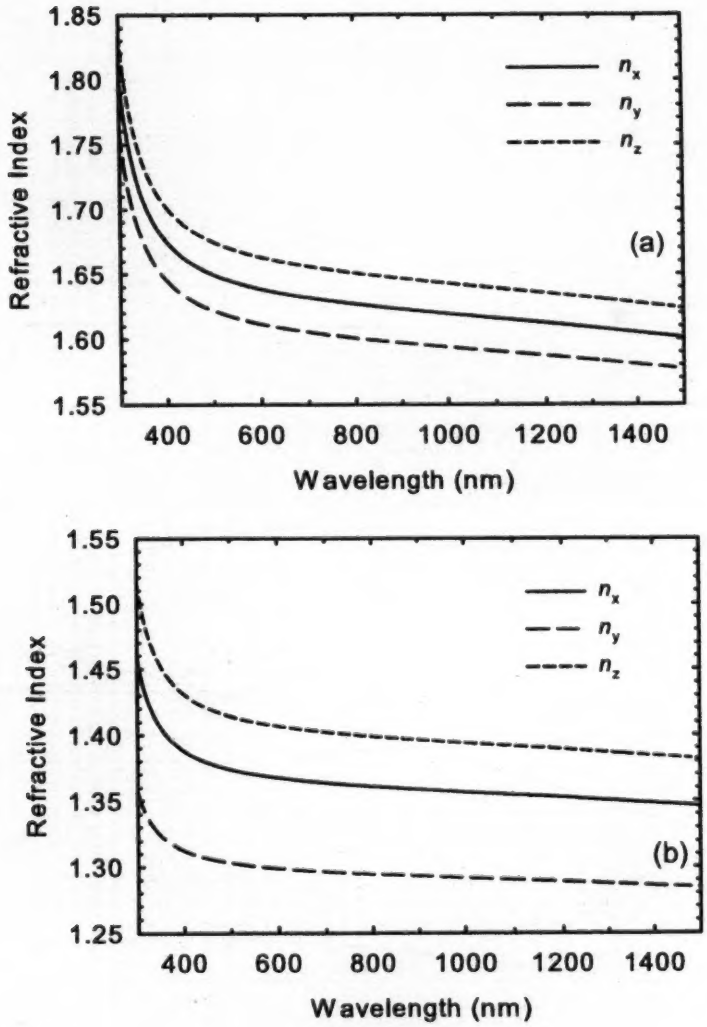

FIGURE 4.8

Principal indices of refraction of tilted columnar Y_2O_3:Eu films. The principal indices of samples B ($\alpha = 60°$) and G ($\alpha = 85°$) are depicted. The indices of sample B were greater than those of sample G because sample B was more dense.

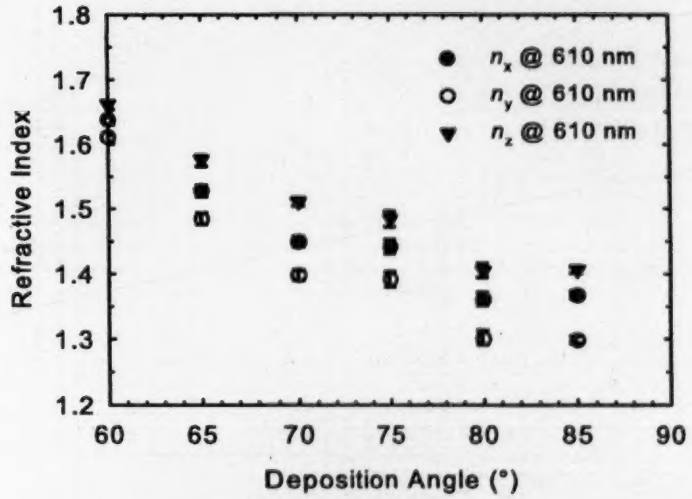

FIGURE 4.9

Variation of the principal indices of refraction of tilted columnar Y_2O_3:Eu thin films with deposition angle. The indices decreased with deposition angle because the films were more porous at higher deposition angles. The error bars were estimated using the 90% confidence limits calculated as part of the VASE analysis.

The refractive index anisotropies (n_x-n_y, n_z-n_y, n_z-n_x) were calculated from the principal indices, as was as the normal incidence birefringence

$$\Delta n = n_x - n_p \tag{4.9}$$

where n_p [5] was determined by

$$n_p = \left(\frac{\sin^2 \beta}{n_z^2} + \frac{\cos^2 \beta}{n_y^2} \right)^{-\frac{1}{2}}. \tag{4.10}$$

The variation of the refractive index anisotropies and normal incidence birefringence with deposition angle are depicted in Fig. 4.10. As expected, the largest refractive index anisotropies were observed for n_z-n_y, because $n_y < n_x < n_z$, for tilted thin films [5, 6, 8]. The

normal incidence birefringence, Δn, was found to reach a maximum value of ~ 0.02 at 65°. The maximum normal incidence birefringence occurred at a deposition angle very similar to that predicted to give the maximum column anisotropy in simulations [26]. The normal incidence birefringence is important because it is a good approximation of the local linear birefringence in a plane parallel to the substrate and at a given thickness of a chiral thin film. The strength of the circular Bragg phenomenon exhibited by a chiral thin film is approximately proportional to the square of the local linear birefringence [27]. The birefringence data determined here suggested that the optimum deposition angle for fabricating chiral Y_2O_3:Eu films exhibiting strong circular Bragg phenomena was 65°. However, given that local linear birefringence values of these Y_2O_3:Eu samples are < 0.02, and that values of 0.07 are routinely obtained for porous chiral TiO_2 films [28], the strength of the circular Bragg phenomena that could be achieved by chiral Y_2O_3:Eu films would be significantly less than those achieved with materials such as TiO_2, as the strength of the circular Bragg phenomenon has been theoretically predicted to depend strongly on this birefringence (see *Chapter 2* and references therein).

The characterization of the optical constants of tilted columnar Y_2O_3:Eu films fabricated at a variety of deposition angles was necessary to enable the proper design of chiral nanostructured Y_2O_3:Eu films exhibiting circular Bragg phenomena at desired spectral locations. These data are also proving useful in studies currently underway on gradient index and high-low index interference filters containing Y_2O_3:Eu in collaboration with fellow graduate students James Gospodyn and Matthew Hawkeye.

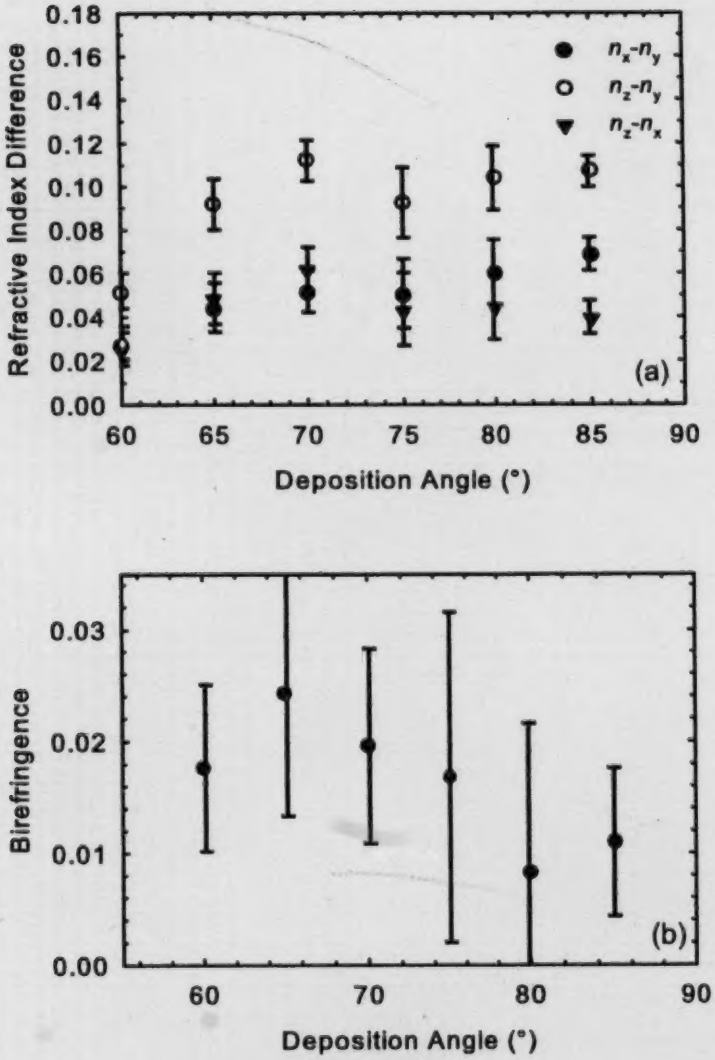

FIGURE 4.10

Principal refractive index differences and normal incidence birefringence of tilted columnar Y_2O_3:Eu thin films. (a) The variation of the differences between the principal refractive indices of tilted columnar Y_2O_3:Eu thin films are depicted. (b) The normal incidence birefringence of the films are also displayed. The normal incidence birefringence values reached a peak value of 0.024 at a deposition angle of 65°.

4.3 Polarized photoluminescence from nanostructured Y_2O_3:Eu thin films

Using transmission ellipsometry and Stokes polarimetry characterization techniques, the ability to control the polarization state of the light emitted by nanostructured Y_2O_3:Eu thin films was tested. Samples with appropriate nanoscale morphologies (Table 4.2) were provided using the fabrication process established in the previous chapter.

TABLE 4.2
Chevronic and Chiral Y_2O_3:Eu films fabricated for polarized photoluminescence studies.

Sample	Nanostructure Type	Deposition Angle (°)	Pitch (nm)	Thickness (nm)
H	Chevron	85	468	1405
I	Helical (RH)	85	440	2200
J	Helical (LH)	85	430	2150
K	Helical (RH)	85	429	3005
L	Helical (LH)	65	447	8940

The selective transmittance of LCP versus RCP light ($T_{LCP-RCP}$) for samples H – L is shown in Fig. 4.11. The left-handed chiral structures (samples J and L) preferentially transmitted RCP light, while the opposite was true of the right-handed structures (samples I and K). Samples I and J, which were fabricated with nearly identical values of pitch, thickness, and number of turns, but opposite handedness from each other, formed an enantiomorphic pair. This enantiomorphic pair yielded very similar selective transmittance spectra but with opposite sign owing to the opposing handedness of the two samples. This demonstrated the reliability of GLAD in forming controlled film structures from one deposition to the next. Figure 4.11 also provides a measure of the improvements created by the annealing process on the circular Bragg phenomena of samples I and J. Sample L clearly exhibited the strongest circular Bragg phenomena because it had a much larger

number of helical turns than the other samples. The selective transmittance spectrum of sample L has a number of narrow peaks owing interference effects and reduced scattering as a result of the increased thickness and reduced porosity of this sample. Large numbers of turns are only compatible with deposition angles in the range of 60° to 70°, because at higher deposition angles broadening of the nanostructures degrades the optical properties of the films [9]. Unfortunately, such thick, dense as-deposited films also tended to be highly stressed, leading to film delamination upon annealing.

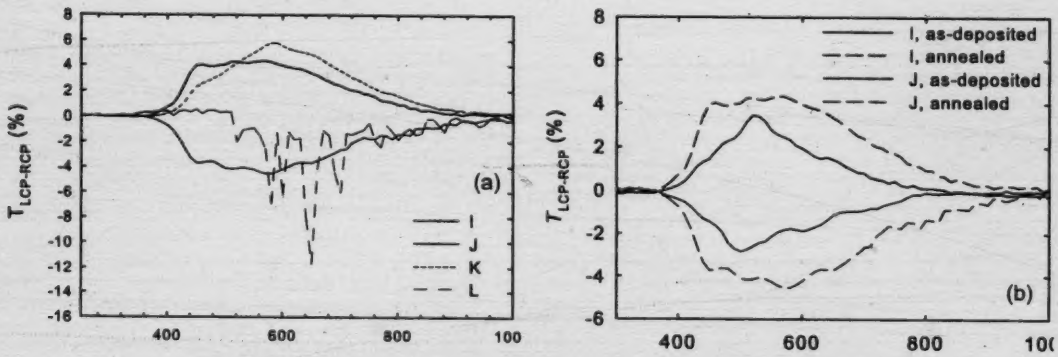

FIGURE 4.11

Spectral variation of selective transmittance of LCP versus RCP light through chiral Y_2O_3:Eu films. (a) The selective transmittance of LCP versus RCP light for samples I – L is displayed for annealed samples. (b) Measurements of the selective transmittance of LCP versus RCP light for samples I and J before and after annealing showed an improvement in the selective transmittance for the annealed samples.

TABLE 4.3

Polarized photoluminescence data obtained chevronic and chiral Y_2O_3:Eu films.

Sample	Peak $T_{LCP-RCP}$ (%)	$T_{LCP-RCP}$ @ 611 nm (%)	ρ (%)	ρ_c (%)
H	n/a	n/a	4.5 ± 0.8	0.6 ± 0.9
I	4.3 ± 0.4	3.8 ± 0.5	5.6 ± 0.7	5.1 ± 0.7
J	-4.6 ± 0.4	-4.0 ± 0.4	3.6 ± 0.7	-2.9 ± 0.7
K	5.8 ± 0.3	5.3 ± 0.3	5.3 ± 0.6	4.9 ± 0.6
L	-11.7 ± 0.6	-1.2 ± 0.4	2 ± 1	-1 ± 1

Table 4.3 summarizes the observed polarized photoluminescence data for the samples. Again, fellow graduate student Michael Taschuck collaborated on the data acquisition and analysis for these photoluminescence measurements. As the S_1 and S_2 components of the light emitted by the chevronic sample were non-zero, while the S_3 component was within error of zero, the chevronic sample (sample H) was observed to emit partially linearly polarized light. The overall degree of polarization, ρ, of light emitted by the chevronic sample was 4.5%, but the degree of circular polarization, ρ_c, was within error of zero. Thus, linear polarization components were the strongest contributors to the overall degree of polarization observed from the chevronic sample. This was expected, because chevronic films are known to exhibit anisotropic optical properties similar to those of tilted columnar films [4]. Thus, the light emitted by the Y_2O_3:Eu chevronic film traversed a birefringent medium, and became partially linear polarized.

Examination of the observed polarized photoluminescence data for the chiral Y_2O_3:Eu films revealed that partially circularly polarized photoluminescence was observed from samples for which the spectral location of the circular Bragg phenomenon overlapped the photoluminescent emission band. This overlap is demonstrated for sample J in Fig. 4.12. Samples I, J, and K produced values of selective transmittance of circularly polarized light at 611 nm that were in the range of 4 – 5 % in magnitude, while sample L

only yielded a selective transmittance value of -1.2 % at 611 nm. This was because the spectral location of the circular Bragg phenomenon and the photoluminescent emission band were not properly overlapped, which meant that the circular Bragg phenomenon was not very strong at the emission wavelengths. Thus, sample L exhibited the lowest observed degree of circular polarization. Samples I, J, and K yielded partially circularly polarized photoluminescence with degrees of circular polarization of 5.1 %, -2.9 %, and 4.9 %, respectively. This represented first experimental confirmation of earlier theoretical predictions [29 – 32] that appropriately designed chiral luminescent thin films fabricated using GLAD could emit partially circularly polarized light.

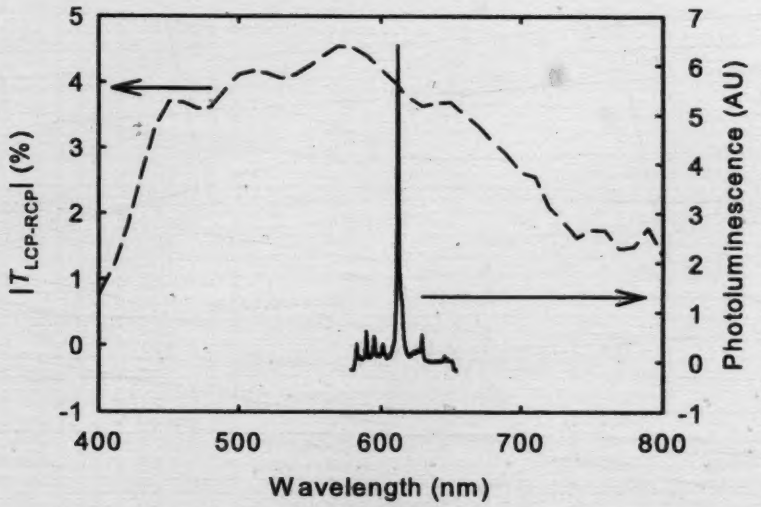

FIGURE 4.12

Selective transmittance of LCP versus RCP light and photoluminescence spectra of a chiral Y_2O_3:Eu film. The selective transmittance of LCP versus RCP light and the photoluminescence spectra of sample I (deposited at an angle of 85°) are both depicted. The photoluminescent emission band was within the wavelengths of the circular Bragg phenomenon for this sample.

The results obtained for both transmittance and photoluminescence polarization measurements upon samples I – L are plotted in Fig. 4.13 to provide a direct comparison between the magnitude of the circular Bragg phenomena for transmittance and for photoluminescence. Furthermore, Fig. 4.13 provides a comparison between the observed photoluminescence from samples deposited on silicon substrates versus those on fused silica substrates. The magnitude of the degree of circular polarization of the photoluminescent output was always observed to be greater for the samples deposited on fused silica than those deposited upon silicon substrates. This suggested that the observed photoluminescence was not emitted from all depths of the film uniformly, but rather primarily from a layer near the air-film interface that faced the incoming excitation beam (see Fig. 4.2). Thus, the emitted light would not travel through the entire chiral film before being observed for the samples deposited on silicon. On the other hand, the emitted light from the samples fabricated on transparent substrates would pass through most of the chiral structure and attain a higher degree of circular polarization as a result. This potential explanation is similar to an observation by Bjorknas *et al.*, who considered the limitations placed on the maximum degree of circular polarization of light emitted from dye-doped cholesteric LCs [33]. Assuming that the dye molecules were randomly distributed throughout the entire film thickness, they showed that the maximum observable degree of circular polarization was reduced from a theoretical maximum of 1 because not all of the emitted light would travel through a substantial thickness of the chiral medium before being detected.

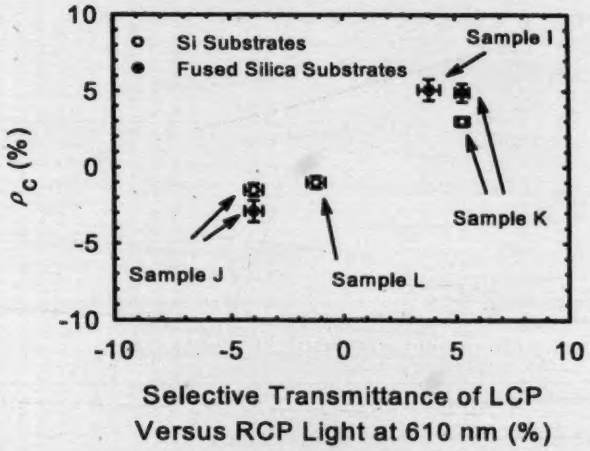

FIGURE 4.13

Comparison of degree of circular polarization of photoluminescent emission and selective transmittance of circularly polarized light for chiral Y_2O_3:Eu films. Samples with larger circular Bragg phenomena at 610 nm, as determined by the selective transmittance of circularly polarized light, exhibited larger degrees of circularly polarization for the photoluminescence measurements.

Unfortunately, the observed degrees of circular polarization were not of a magnitude that would be useful for applications such as low-threshold lasers [32] or circularly polarized emitters [19] for use in displays with anti-glare compensators [34]. For such applications, published data suggests that degrees of circular polarization in excess of 80% are required [14, 35]. Further improvements to the degree of circular polarization of light emitted by chiral Y_2O_3:Eu thin films may be possible, as suggested by the strong circular Bragg phenomena observed in transmittance-mode for the thicker, more dense sample L. However, the improvements offered by dense films would be limited because such films tended to be highly stressed as-deposited, and to delaminate from the substrate during the annealing process. The problem of film stress would be compounded by the low local linear birefringence of the chiral Y_2O_3:Eu thin films, which

would require the use of very thick samples that would likely have even higher stress, to obtain high degrees of circularly polarized photoluminescence (i.e. >80%). The primary factor that appeared to limit the strength of the circular Bragg phenomena of these films was likely the low local linear birefringence of the structures, though, the fibrous nature and random arrangement of the nanostructures on the substrate may have also played a role in this regard.

4.4 Summary

The optical properties of nanostructured Y_2O_3:Eu thin films were investigated using variable angle spectroscopic ellipsometry (VASE), transmission Mueller matrix ellipsometry, and Stokes polarimetry. The principal indices of refraction of tilted columnar Y_2O_3:Eu films were determined through VASE analysis, and were found to decrease with deposition angle. This was because the films were more porous at higher deposition angles. The normal incidence birefringence values of the tilted columnar Y_2O_3:Eu films were determined from the principal indices of refraction, and were found to reach a maximum value of ~ 0.02 at a deposition angle of 65°.

Using the principal index and normal incidence birefringence data, chiral Y_2O_3:Eu films were designed and fabricated. The circular Bragg phenomena of the chiral Y_2O_3:Eu films were observed for transmittance data obtained by transmission Mueller matrix ellipsometry. The chiral Y_2O_3:Eu thin films were also demonstrated to emit partially circularly polarized light, confirming earlier published predictions that nanostructured films fabricated by GLAD could be used to produce polarized luminescence [29 – 32]. Similarly, chevronic Y_2O_3:Eu thin films were found to emit partially linearly polarized

light. The observed degrees of circular polarization for chiral Y_2O_3:Eu thin films were on the order of a few percent. Because the maximum normal incidence birefringence measured for tilted columnar Y_2O_3:Eu thin films was only ~ 0.02, the potential for improving the circularly polarized photoluminescence response by fabricating denser films with large numbers of turns was limited. Very thick films would be required to obtain levels of circularly polarized luminescence that could prove technologically useful. Thus, while the Y_2O_3:Eu proved useful in demonstrating the concept of using luminescent nanostructured thin films fabricated by GLAD to produce polarized luminescence, it is not an ideal material system for fabricating luminescent chiral thin films with high enough degrees of circular polarization to be used in applications such as low-threshold band edges lasers and circularly polarized emitters.

References

1. R. M. A. Azzam and N. M. Bashara, *Ellipsometry and Polarized Light*, North Holland Press, Amsterdam (1987).
2. J. A. Woollam, B. Johs, C. M. Herzinger, J. Hilfiker, R. Synowicki, and C. L. Bungay, "Overview of variable angled spectroscopic ellipsometry (VASE), part I: basic theory and typical applications," *Proceedings of SPIE*, **CR72**, 3 (1999).
3. B. Johs, J. A. Woollam, C. M. Herzinger, J. Hilfiker, R. Synowicki, and C. L. Bungay, "Overview of variable angled spectroscopic ellipsometry (VASE), part II: advanced applications," *Proceedings of SPIE*, **CR72**, 29 (1999).
4. T. Motohiro and Y. Taga, "Thin film retardation plate by oblique deposition," *Applied Optics*, **28**, 2466 (1989).
5. I. Hodgkinson, Q. H. Wu, and J. Hazel, "Empirical equations for the principal refractive indices and column angle of obliquely deposited films of tantalum oxide, titanium oxide, and zirconium oxide," *Applied Optics*, **37**, 2653 (1998).

6. I. Hodgkinson, Q. H. Wu, and S. Collett, "Dispersion equations for vacuum-deposited tilted-columnar biaxial media," *Applied Optics*, **40**, 452 (2001).

7. G. Beydahyan, K. Kaminska, T. Brown, and K. Robbie, "Enhanced birefringence in vacuum evaporated silicon thin films," *Applied Optics*, **43**, 5343 (2004).

8. J. Gospodyn and J. C. Sit, "Characterization of dielectric columnar thin films by variable angle Mueller matrix and spectroscopic ellipsometry," *Optical Materials*, in press (2006).

9. A. C. van Popta, J. C. Sit, and M. J. Brett, "Optical properties of porous helical thin films," *Applied Optics*, **43**, 3632 (2004).

10. E. Collett, *Polarized Light: Fundamentals and Applications*, Marcel Dekker, New York (1993).

11. E. Collett and V. Gazerro, "Polarization measurements in a spectrofluorometer," *Optics Communications*, **129**, 229 (1996).

12. E. Collett and V. Gazerro, "Polarization measurements in spectrometers and spectrofluorometers," *Spectroscopy*, **13**, 21 (1998).

13. V. Yamamoto, I. Hosako, M. Akiba, and N. Ohtani, "Excitation of right- and left-circularly polarized photoluminescence in silicon-based luminescent materials," *Journal of Applied Physics*, **91**, 2725 (2002).

14. K. L. Woon, M. O'Neill, G. J. Richards, M. P. Aldred, and S. M. Kelly, "Stokes parameter studies of spontaneous emission from chiral nematic liquid crystals as a one-dimensional photonic stopband crystal: experiment and theory," *Physical Review E*, **71**, 041706 (2005).

15. G. E. Jellison, Jr. and F. A. Modine, "Parameterization of the optical functions of amorphous materials in the interband region," *Applied Physics Letters*, **69**, 371 (1996).

16. W. H. Press, S. A. Teukolsky, W. T. Vetterling, and B. P. Flannery, *Numerical Recipes in Fortran: the Art of Scientific Computing*, Cambridge University Press, Cambridge (1992).

17. K. Kaminska, A. Amassian, L. Martinu, and K. Robbie, "Growth of vacuum evaporated ultraporous silicon studied with spectroscopic ellipsometry and scanning electron microscopy," *Journal of Applied Physics*, **97**, 013511 (2005).

18. G. Beydaghyan, C. Buzea, Y. Cui, C. Elliott, and K. Robbie, "*Ex situ* ellipsometric investigation of nanocolumns inclination angle of obliquely evaporated silicon thin films," *Applied Physics Letters*, **87**, 153103 (2005).

19. S. H. Chen, D. Katsis, A. W. Schmid, J. C. Mastrangelo, T. Tsutsui, and T. N. Blanton, "Circularly polarized light generated by photoexcitation of luminophores in glassy liquid-crystal films," *Nature*, **397**, 506 (1999).

20. J. D. Jackson, *Classical Electrodynamcis*, Wiley, New York (1999).

21. WVASE32, J.A. Woollam Co., Inc.

22. D. E. Aspnes, "Optical properties of thin films," *Thin Solid Films*, **89**, 249 (1982).

23. J. Gospodyn, personal communication, February 2006.

24. H. van Nieuwenhuizen and H. B. Haanstra, "Microfractography of thin films," *Philips Technical Review*, **27**, 87 (1966).

25. R. N. Tait, T. Smy, and M. J. Brett, "Modelling and characterization of columnar growth in evaporated films," *Thin Solid Films*, **226**, 196 (1993).

26. R. N. Tait, T. Smy, and M. J. Brett, "Structural anisotropy in oblique-incidence thin metal-films," *Journal of Vacuum Science and Technology*, **10**, 1518 (1992).

27. I. Hodgkinson, Q. H. Wu, B. Knight, A. Lakhtakia, and K. Robbie, "Vacuum deposition of chiral sculptured thin films with high optical activity," *Applied Optics*, **39**, 642 (2000).

28. I. Hodgkinson and Q. H. Wu, "Serial bideposition of anisotropic thin films with enhanced linear birefringence," *Applied Optics*, **38**, 3621 (1999).

29. A. Lakhtakia, R. Messier, M. J. Brett, and K. Robbie, "Sculptured thin films (STFs) for optical, chemical and biological applications," *Innovations in Materials Research*, **1**, 165 (1996).

30. A. Lakhtakia, "Local inclination angle: a key structural factor in emission from chiral sculptured thin films," *Optics Communications*, **202**, 103 (2002).

31. A. Lakhtakia, "On radiation from canonical source configurations embedded in structurally chiral materials," *Microwave and Optical Technology Letters*, **37**, 37 (2003).

32. V. I. Kopp, Z.-Q. Zhang, A. Z. Genack, "Lasing in chiral photonic structures," *Progress in quantum electronics*, **27**, 369 (2003).

33. K. Bjorknas, P. Raynes, and S. Gilmour, "Effects of molecular shape on the photoluminescence of dyes embedded in a chiral polymer with a photonic band gap," *Journal of Materials Scienc: Materials in Electronics*, **14**, 307 (2003).

34. D. J. Broer, J. Franciscus, J. J. van Tongeren, R. J. Visser, *US Patent Application*, 2005/0179371A1 (2005).

35. J. Schmidtke and W. Stille, "Fluorescence of a dye-doped cholesteric liquid crystal film in the region of the stop band: theory and experiment," *The European Physical Journal B*, **31**, 179 (2003).

CHAPTER 5
Fabrication and structural characterization of nanostructured Alq_3 thin films

This chapter outlines the single-step fabrication process used to produce organic luminescent nanostructured thin films of tris-(8-hydroxyquinoline) aluminum (Alq_3) and highlights the remarkable structural properties of chiral Alq_3 thin films. The fabrication procedure will be presented followed by the investigation of the structural properties of these nanostructured Alq_3 thin films through SEM and VASE characterization. These characterization methods allowed for some key observations that will prove useful to future research upon vacuum-deposited organic nanostructured thin films fabricated by GLAD. The initial growth of these films consisted of a solid layer before the films began to form porous nanostructures. The thickness of the initial solid layer was dependent upon the substrate conditions and the deposition angle. The column tilt angles of Alq_3 films were also measured and were higher than predicted by Tait's rule. Helical Alq_3 films were fabricated, and the individual helices were found to form in a nearly hexagonal close-packed array. Also, the individual helices were fairly uniform and free of broadening imperfections common to porous inorganic chiral thin films.

5.1 Fabrication

Previously, porous organic chiral thin films were fabricated using a templating and inversion process in which an inorganic chiral film fabricated by GLAD served as the initial template [1, 2]. While this is itself a powerful technique, it involves a series of processing steps. Also, it does not readily provide a means to overcome the microstructural imperfections of the template, such as the column bifurcation and broadening effects that are common in inorganic films fabricated with GLAD. A precise, single-step process for fabricating organic porous chiral thin films would be advantageous for photonics and other applications demanding uniform film morphologies. The chiral Alq_3 films discussed here constituted the first directly vacuum deposited porous organic chiral thin films, and exhibited remarkable structural uniformity and self-ordering. It should be noted briefly that at the same time as the initial studies of porous chiral Alq_3 films were reported, an initial study that demonstrated the fabrication of parylene helices was also reported [3]. However, this study only reported the fabrication methods used to produce the parylene helices, which involved the rough vacuum spray pyrolysis of parylene onto rotating substrates held at glancing angles of incidence. The report did not depict any results beyond a few initial SEM images of the films. Furthermore, the parylene helices produced did not exhibit size scales compatible with producing optical effects at visible wavelengths, as the diameters of structures were hundreds of nanometers in diameter.

Fabrication of nanostructured Alq_3 films was carried out under high vacuum conditions in a vacuum chamber (Fig. 5.1) containing the same type of motion control apparatus as used in the fabrication of inorganic GLAD films. The motivation and initial fabrication apparatus for this work was developed in collaboration with Dr. Kenneth Westra, the director of the University of Alberta Nanofabrication Facility. The key

differences between the apparatus shown in Fig. 5.1 and that which was discussed in *Chapter 3* was that instead of an electron beam gun a low temperature effusion cell (LTE21000 K, Kurt J. Lesker Company) was used to sublimate the source material. The use of a low-temperature effusion cell to sublimate the Alq_3 source material allowed for very stable control of the source temperature, and thus the deposition rate, during the deposition. Also, the throw distance between the source and the center of the substrate chuck was only 24 cm, as opposed to the 42 cm throw distance used in the electron beam evaporation system. This was a result of there being insufficient space in the vacuum chamber to facilitate the longer throw distance. During the deposition, the source materials were held in an alumina crucible within the effusion cell. Typically, source temperatures in the range of 270°C – 300°C were used for the fabrication of the Alq_3 samples discussed here. This led to deposition rates at the substrate surface that were ~ 0.5 – 2 Å/s, after adjusting the deposition rate for the geometry introduced by the GLAD apparatus. The deposition rate was monitored by a quartz crystal microbalance (QCM) placed near the substrate chuck. Control of the rotation rates of the deposition angle and substrate rotation motors was based upon the deposition rate measured by the QCM. All of the Alq_3 films fabricated in this study were sublimated under high vacuum conditions, most often at base pressures less than 2×10^{-6} Torr.

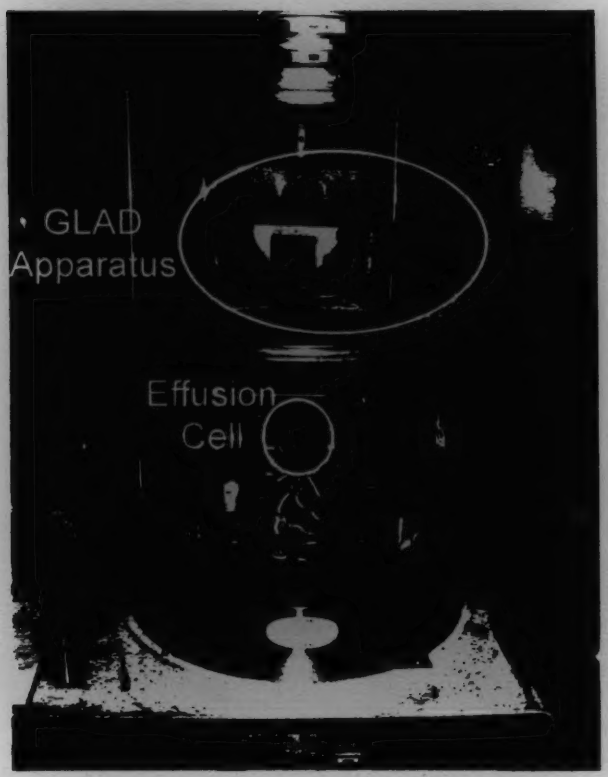

FIGURE 5.1

Deposition apparatus. A typical deposition system used in the fabrication of nanostructured Alq_3 thin films is pictured. An effusion cell was used to heat the source material and produce a stable deposition rate. The GLAD apparatus consisted of two computer-controlled stepper motors.

The films were grown using source material supplied by Gelest (> 99% purity). The source material was stored in a vacuum furnace at 125°C to drive off any water vapor in the powder, but was not purified or otherwise processed once received from the manufacturer. This storage technique improved the stability of the Alq_3 source material during the film depositions. Source material that was stored in air was subject to explosive spitting during the depositions, which was due, in part, to large amounts of

trapped moisture in the source powder that was stored in air. The potential for further improvements to the Alq_3 source stability is currently being investigated, with the use of higher purity Alq_3 fine-powders showing initial promise. Future experiments may also explore the possibility of using substrate cooling to provide a great degree of control over the nanostructural morphologies obtained and the film growth.

Using the effusion cell-based GLAD deposition system, tilted columnar and helical films were deposited on as-supplied silicon wafers and 7059 glass slides yielding structures as shown in Fig. 5.2a and 5.2b. These structures were very uniform, smooth, and not subject to column broadening, in contrast to comparable inorganic films. Vertical pillar morphologies (Fig. 5.2c) and SBD-pillar morphologies [4] (Fig. 5.2d) were not as impressive. Because vertical pillar and SBD-pillar morphologies were not critical to the study of circularly polarized luminescence from nanostructured Alq_3 films, they were not explored any further in the studies discussed here. However, it seemed that the poorer structures yielded with these morphologies might be related to the surface energies and the size of the individual Alq_3 monomers that were arriving at the substrate. One interesting feature of all of the films was the presence of a solid layer of Alq_3 that grew on the substrate surface prior to the formation of the individual nanostructures.

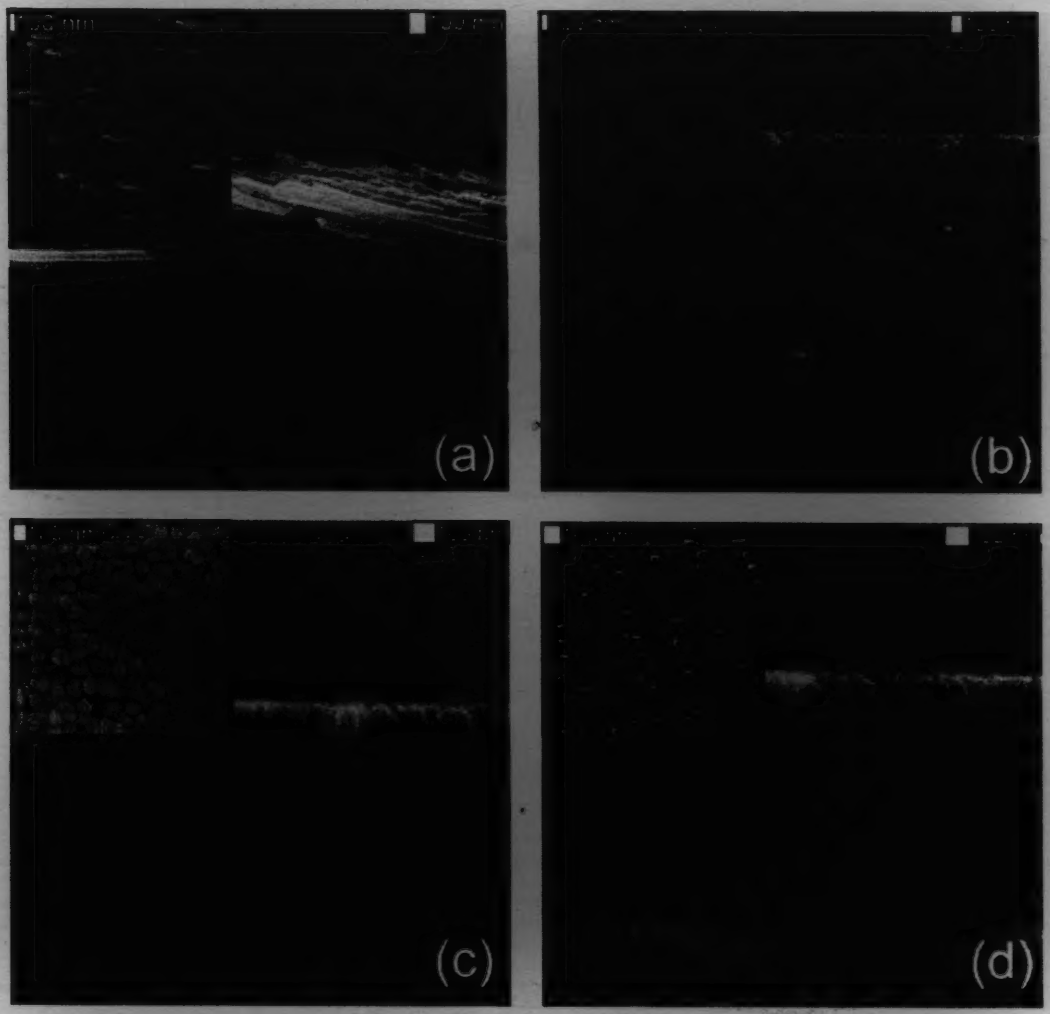

FIGURE 5.2

SEM micrographs of (a) tilted columnar, (b) helical, (c) pillar, and (d) SBD-pillar Alq_3 films. Plan (inset) and section views are shown. The structures produced for the tilted columnar and helical morphologies were very uniform and smooth, and the helical structures formed in a nearly hexagonal close-packed array. The structures produced for pillar and SBD-pillar morphologies were less ideal, possibly as a result of the surface energies and size of monomers arriving at the substrate.

The remarkably smooth nanostructures formed by tilted columnar and helical Alq_3 films and the initial solid layer were explained in light of the findings of Brinkmann *et al.* [5, 6]. Their work demonstrated that the early stages of normal-incidence Alq_3 film growth upon an apolar surface resulted in a non-random pattern of droplets forming on the substrate. They found that the droplets exhibited a spherical cap shape with a nearly constant contact angle for surface coverage ranging from 8 – 100 % where 100% represents a complete monolayer. This indicated that secondary nucleation and coarsening phenomena common to many inorganic thin film growth mechanisms [7] were absent from the growth of their Alq_3 samples. Similarly, the smooth, uniform features of the tilted columnar and chiral Alq_3 films depicted in Fig. 5.2 were apparently due to the absence of secondary nucleation and coarsening phenomena, seemingly as a result of the size of the critical nucleus in these films being larger than is often the case [6]. The large critical nucleus results in depletion regions surrounding the nuclei in which the arrival of new Alq_3 monomers is unable to achieve sufficient saturation for the formation of additional nuclei.. The lack of broadening in the structures depicted in Fig. 2a and 2b also seemed to be a result of the lack of secondary nucleation during the growth. These smooth features and their arrangement upon the substrate are somewhat reminiscent of the droplet arrays formed during condensation of liquid-like systems upon cold substrate [8].

The experiments discussed here used substrates of glass or native-oxide-passivated Si wafers. These substrates were hydrophilic, and could be considered to be unlike those used by Brinkmann *et al.* Thus, the initial growth of the nanostructured Alq_3 did not exhibit the individual droplet growth typical of Alq_3 film growth on hydrophobic substrates, because the Alq_3 was initially wetted to the substrate. Hence, the initial solid layer of film growth can be termed the wetting layer. Above a certain thickness, the

impinging Alq_3 monomers had reduced affinity for the surface of the amorphous solid Alq_3 layer and began to dewet, forcing the film growth to proceed in a partial wetting regime [5]. Once the growth entered this partial wetting regime, self-shadowing effects dominated. This seemed to prevent further nucleation and growth on the surface of the solid film because the Alq_3 droplets that formed began to receive more of the incoming glancing incidence vapor flux, and growth preferentially occurred at these sites Thus, arriving Alq_3 monomers impinged upon the existing droplets. The impinging monomers partially wet to those droplets to minimize their surface energy, producing the smooth uniform features depicted above.

Brinkmann *et al.* analyzed the non-random droplet patterns that they observed in terms of a phenomenological capture zone model [9]. In this model, each nucleus on a substrate was surrounded by a region such that additional adatoms arriving in that region would contribute to the growth of the nucleus of that region, or capture zone. Accordingly, the early stages of film growth were subject to direct ripening of nuclei [10], in which closely neighboring nuclei merge. This was in contrast to Ostwald ripening [10, 11] which involves large nuclei growing and coarsening at the expense of small nuclei which disappear, even for nuclei separated by large distances. Direct ripening during the early stages of Alq_3 film growth established a minimum nearest neighbor distance, because neighboring nuclei lying closer than such a distance merged. Thus, a non-random pattern of the nuclei with short-range order was established early within the deposition. Furthermore, Brinkmann *et al.* [6] found that diffusive interactions between droplets caused their centers of mass to migrate to empty regions on the substrate, which reinforced the formation of a preferred nearest neighbor distance. The nearly hexagonal close-packed (hcp) arrangement of the helical Alq_3 structures observed here could be comprehended using Brinkmann's findings also. The combined effects of the

non-random nuclei pattern, the diffusive interactions between the Alq_3 droplets, and the continuous substrate rotation were thought to influence the self-organization of the helical Alq_3 structures. These effects would encourage the formation of the nanostructures in an arrangement with a high degree of rotational symmetry, where the separations between structures were determined by the nearest neighbor distance established by the direct ripening process.

To further illustrate the self-organized nature of helical Alq_3 films compared to inorganic GLAD films, the plan views of a graded pitch helical Alq_3 film and a pillar Y_2O_3:Eu film are both depicted in Fig. 5.3. The ordering, or lack thereof, for the films was be established by taking the 2-dimensional (2D) Fourier transform of these plan-view SEM images of the films. To do so, the 2D fast Fourier transform (FFT) implemented in ImageJ was used [12]. The radial location of the first (or only) ring in the FFT images indicated the first nearest neighbor (or most probable) column spacing. The presence of additional localized rings in the FFT image of the Alq_3 film represented additional nearest neighbor spacings, and indicated that a degree of ordering was present in the plane parallel to the substrate. However, the presence of bright rings as opposed to a rotationally symmetric array of bright points in the FFT image was indicative of a lack of long-range ordering. This suggested that the partial ordering exhibited by the chiral Alq_3 films was actually only short-range ordering -- a result that was consistent with the possible growth behaviour discussed previously. The FFT image of inorganic film lacked the presence of a localized ring, which indicated the absence of ordering. Thus, the nanostructures in the Alq_3 film were spaced more uniformly and exhibited an heightened degree of orientational ordering compared to an inorganic film.

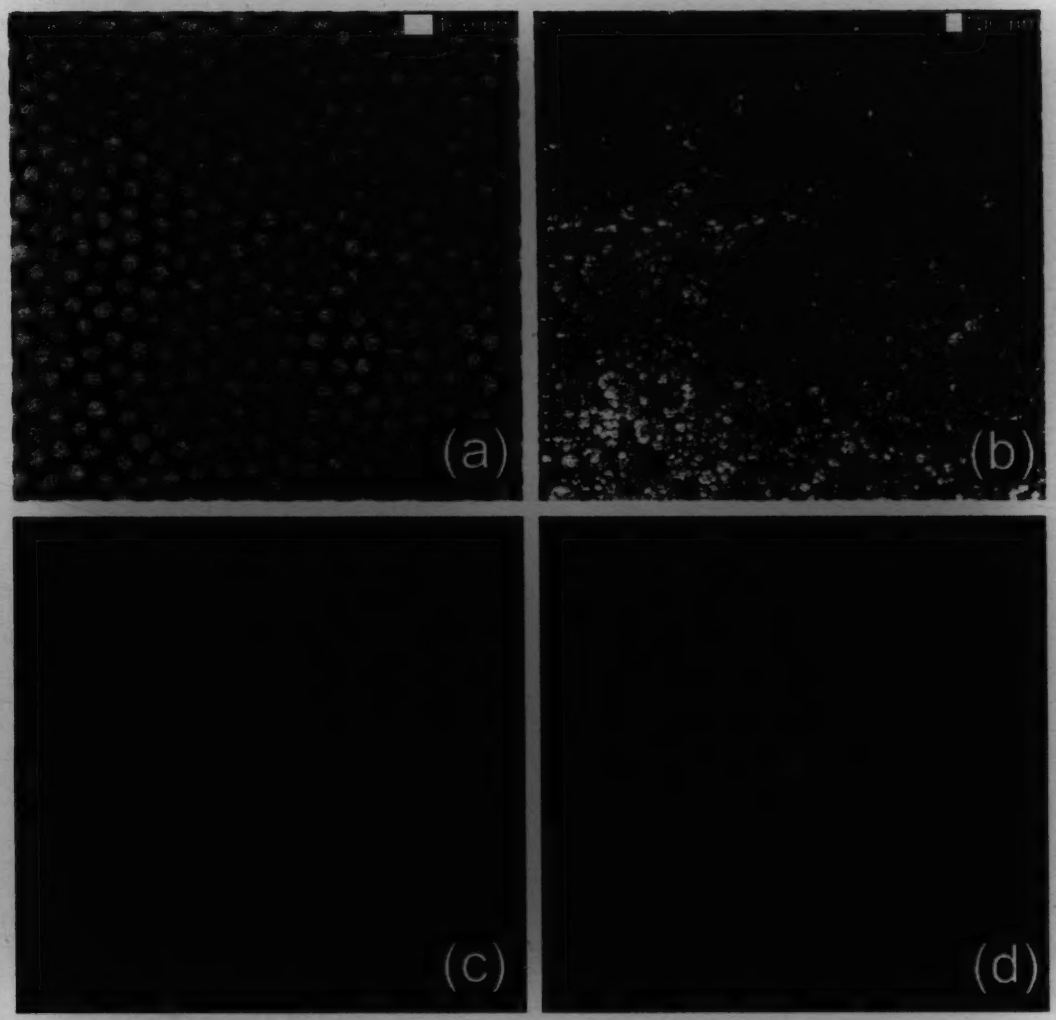

FIGURE 5.3

SEM micrographs and 2D FFT of SEM micrographs of organic and inorganic GLAD films. Plan view SEM micrographs of a (a) graded-pitch chiral Alq_3 film and (b) pillar Y_2O_3:Eu film are depicted. The 2D-FFT of the (c) graded-pitch chiral Alq_3 and (d) pillar Y_2O_3:Eu images were also obtained. The 2D-FFT of the graded-pitch chiral Alq_3 film contained concentric rings indicating that the individual structures had some short range order and thus they were in a partially ordered array. No concentric rings were observed for the 2D-FFT of the pillar Y_2O_3:Eu image.

5.2 Controlling the wetting layer thickness

One of the most intriguing elements of the observed growth of nanostructured Alq_3 films was the role played by the interactions between the substrate and the deposited molecules. As Brinkmann *et al.* proposed [6], the potential use of the chemical nature of the molecule and the substrate to obtain spontaneous hexagonal arrays of molecules could prove quite useful for organizing film growth on the nanoscale. Their findings regarding the growth of Alq_3 droplets on an apolar substrate suggested that similar substrates could enable the fabrication of nanostructured Alq_3 films that had no initial wetting layer. The ability to control the formation of the wetting layer could prove critical to the development of some applications involving nanostructured organic films, including electroluminescent devices and sensors. Furthermore, the elimination of the wetting layer could be used to form nanostructured organic films in periodic arrangements other than hexagonal close-packed arrays [13 – 16]. The effect of chemical treatments upon substrates prior to film deposition was preliminarily investigated to this end (Fig. 5.4). A monolayer of octadecyltrichlorosilane was applied to the substrate in order to increase the hydrophobicity, which meant that the substrate was less polar. This prevented the formation of the wetting layer during the growth of a helical Alq_3 film, but did not produce any deleterious defects or film degradation. These preliminary results were obtained in collaboration with fellow students Bryan Szeto, Shufen Tsoi, and Rebecca Hansen, who are continuing to investigate the potential uses of a variety of substrate treatments for applications of nanostructured organic thin films.

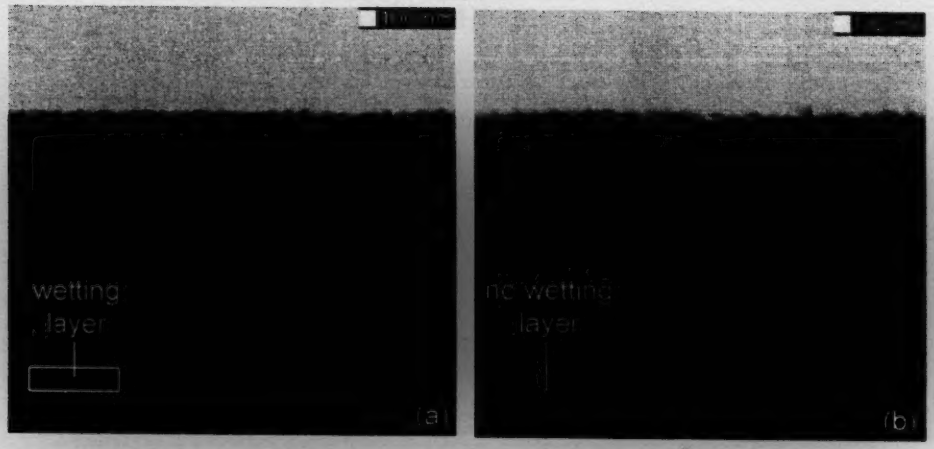

FIGURE 5.4

Effect of surface treatments on the formation of the wetting layer. SEM micrographs of chiral Alq_3 films grown at the same time on (a) untreated, native-oxide-passivated silicon and on (b) silicon treated with octadecyltrichlorosilane revealed that the surface treatment prevented the formation of the wetting layer. Both samples were deposited simultaneously at a deposition angle of 75°.

Interestingly, the thickness of the wetting layer was not only dependent upon the chemical nature of the substrate, but also upon the deposition angle (Fig. 5.5). The wetting layer was substantially reduced from ~ 170 nm in the case of the film deposited at $\alpha = 75°$ to ~ 40 nm in the case of the film deposited at $\alpha = 85°$. This trend was further quantified by measuring the wetting layer thickness for additional chiral Alq_3 films grown at deposition angles of $75° \leq \alpha \leq 85°$, the results of which are shown in Fig. 5.6. (Note that no data were acquired for $80° < \alpha < 85°$ because concurrent studies of the optical properties of these Alq_3 films indicated that samples fabricated in the range $75° \leq \alpha \leq 80°$ were of the most interest for chiral optical measurements.) The trend towards reduced wetting layer thickness for films deposited at larger angles of incidence was understood

according to the following rationale: at lower deposition angles the polarity match between the substrate and Alq_3 resulted in the formation of Alq_3 droplets with strong affinity for the substrate and thus a low contact angle. Simultaneously, the self-shadowing effect induced by GLAD led to the formation of spaces between neighboring nuclei. Initially, the low contact angles of the Alq_3 droplets dominate, and the droplets spread out into the spaces formed as a result of the self-shadowing effect. This led to coalescence of neighboring droplets and the formation of a solid wetting layer, likely with some surface topography. Eventually, the polarity match between the impinging Alq_3 molecules and the amorphous Alq_3 wetting layer became poor enough for the growth to enter the partial wetting regime. In this regime, the contact angle of the Alq_3 droplets was higher than at the very start of the deposition, which would lead to an additional enhancement of the self-shadowing effect, with self-shadowing becoming dominant at some critical thickness. At higher deposition angles, this critical thickness would be thinner because the spacing induced by the self-shadowing would be larger.

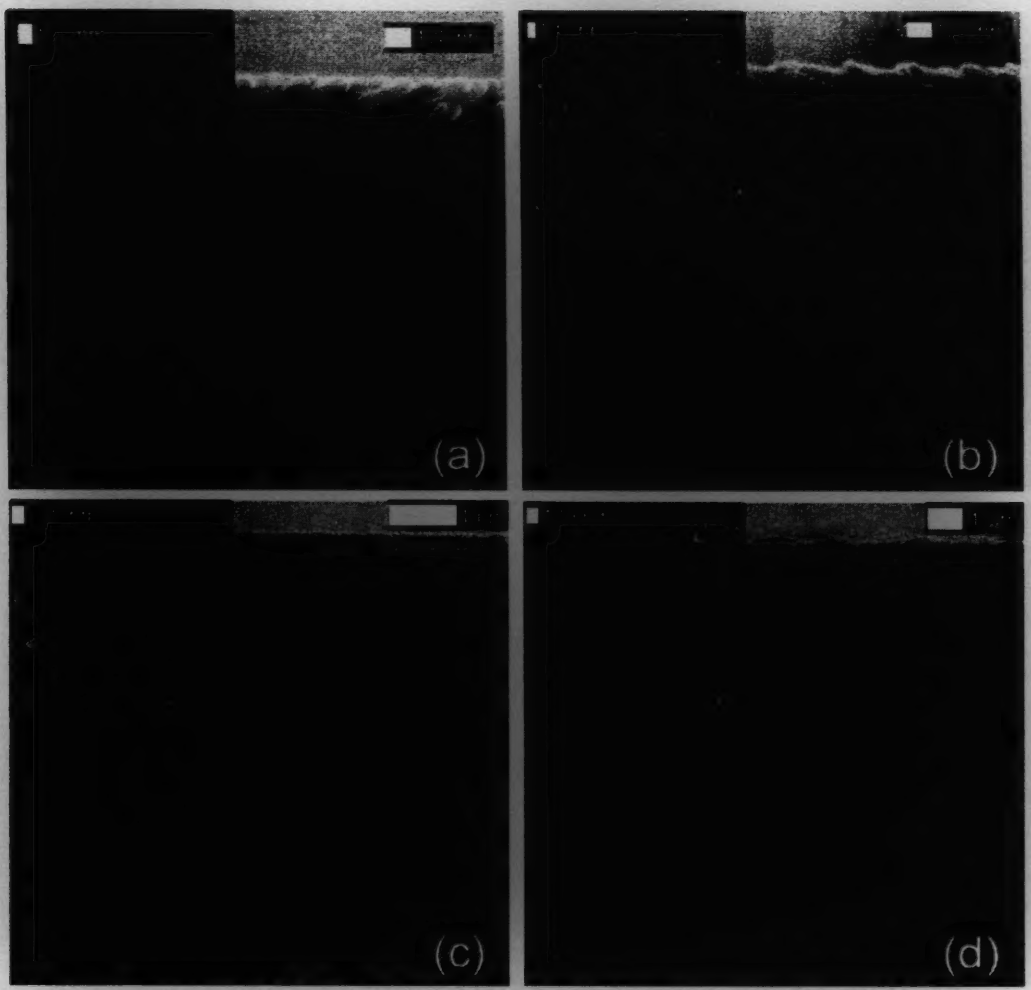

FIGURE 5.5

SEM micrographs of chiral Alq_3 films. Films grown at deposition angles of (a) 75°, and (b) 85° are shown, along with (c) ~ 20 turn and (d) ~ 40 turn samples both fabricated at deposition angles of 78°. Plan (inset) and section views are shown. The structures formed in ordered arrays under all of these conditions, and very thick films could be fabricated without encountering any significant broadening imperfections.

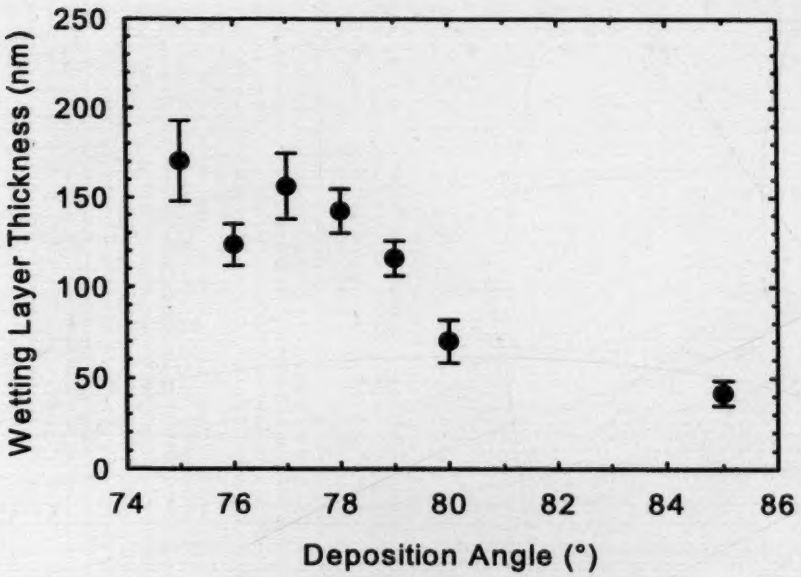

FIGURE 5.6

Effect of deposition angle on wetting layer thickness. The wetting layer decreased with deposition angle because self-shadowing effects were more dominant for higher deposition angles. The error bars represent the standard deviation of the wetting layer thickness measured for each deposition angle.

These methods of altering the wetting layer thickness of nanostructured Alq_3 films could prove instrumental in a number of future applications, including the formation of nanostructured Alq_3 films in arrays with designed periodicity. An initial attempt at growing periodic nanostructured Alq_3 films, in this case square spiral films, upon a tetragonal array of SU-8 seeds with a 150 nm periodicity produced some encouraging results (Fig 5.7). This was done in collaboration with Mark Summers, who fabricated the SU-8 seed arrays with e-beam lithography. Despite of the presence of the wetting layer, the first arms of the square spirals appeared to maintain the spacing imparted by the SU-8 seeds for a choice of seed spacing that was close to the natural spacing of the Alq_3

structures. Subsequent arms of the square spirals tended to bifurcate or merge and thus did not follow the tetragonal order of the seed array. However, it seemed clear that the greatest potential for fabricating arbitrary arrays of smooth and uniform nanostructures of Alq_3 will ultimately be possible by combining lithographically fabricated nodule arrays with appropriate chemical treatments to eliminate the formation of the wetting layer.

FIGURE 5.7

Square spiral Alq_3 film on a tetragonal array of seeds. An SEM micrograph of a square spiral Alq_3 film grown onto an array of SU-8 seeds with a periodicity of 150 nm is shown. The first portion of the structure appeared to form with the same periodicity as the seed array.

5.3 Column geometry of nanostructured Alq_3 films

Image analysis of both section and plan view SEM micrographs of helical Alq_3 films deposited at various angles of incidence was used to reveal how the cross-sectional shapes of the individual helical nano-columns varied with deposition angle. The fabrication of films at various angles of incidence was performed with assistance of

Bryan Szeto, a fellow graduate student. The analysis was carried out using the built-in measurement tools of ImageJ [12]. The nano-column diameters measured from both plan view and section view micrographs seemed to be nearly constant with deposition angle (Fig. 5.8). The error bars were taken to be the standard deviation of the nano-column diameters measured for a given sample. These standard deviations of the nano-column diameters also varied little with deposition angle. This seemed to suggest that the cross-sectional shapes of the Alq_3 helices were determined primarily by the properties of the material itself. This interesting observation certainly was deserving of further investigation, however, such investigation was beyond the scope of this thesis.

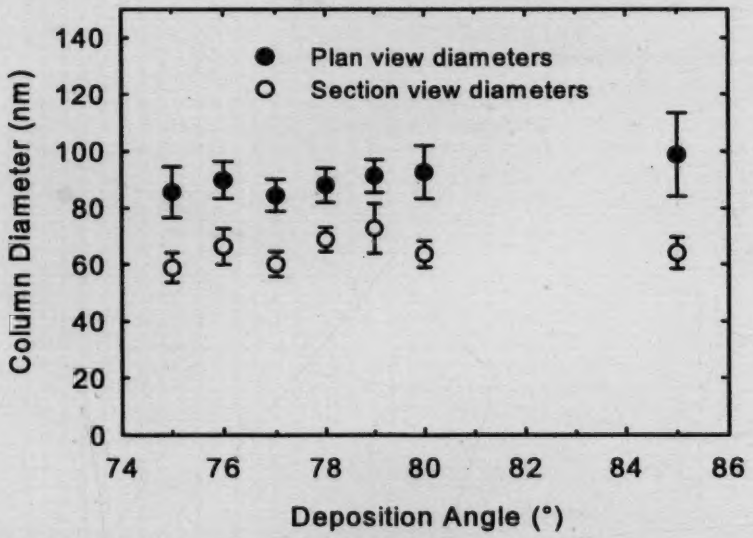

FIGURE 5.8

Effect of deposition angle on column diameter in Alq_3 helices. The diameters of were measured from both section view (side views) and plan view (top-down views) SEM images. The plan view diameters, or cross-sections, of the nanostructures were larger than the section view diameters. Both data sets showed little variation with deposition angle. The error bars represent the standards deviation of the column diameters measured for each deposition angle.

The column spacings of the helical Alq_3 films were estimated from the 2D-FFT of plan-view SEM images of the films. Figure 5.9 shows a plan view of a typical helical Alq_3 film along with its 2D-FFT power spectra. As discussed previously, the nearest neighbor column spacing was indicated by the radius at which the first maximum in the FFT images occurred [5, 17]. Because the column diameter was essentially constant with deposition angle, the column spacing can be considered to be an estimate of the porosity of the films. The column spacing (and porosity) of the films clearly increased with deposition angle (Fig. 5.10). The column spacing of the most porous structures studied here ($\alpha = 85^\circ$) was ~ 85% greater than that of the least porous structures ($\alpha = 75^\circ$). An additional set of helical Alq_3 films was fabricated at a constant deposition angle (78°) and with increasing numbers of turns. Analysis of these films revealed that the column spacing was invariant with increasing number of turns (Fig. 5.11). This was to be expected, given the lack of column competition [18] in the growth of these structures.

FIGURE 5.9

SEM micrograph of a helical Alq_3 film (~ 5 turns, 2.5 microns thick) and its 2D-FFT image. The 2D-FFT images of helical Alq_3 films had incomplete concentric ring structures. This was possibly because the plan view SEM images of helical Alq_3 films showed a finite arc of the helices instead of looking into the ends of the helices.

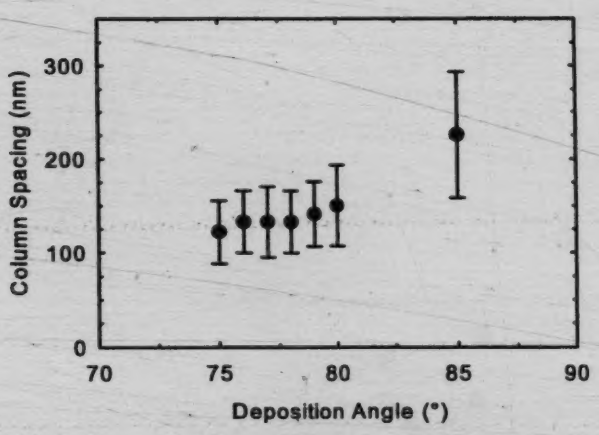

FIGURE 5.10

Effect of deposition angle on inter-columnar spacing in helical Alq_3 films. The inter-columnar spacing in helical Alq_3 films increased somewhat with deposition angle. This was related to the increased porosity of films fabricated at higher deposition angles. The error bars represent the standard deviation of the column spacings measured for each deposition angle.

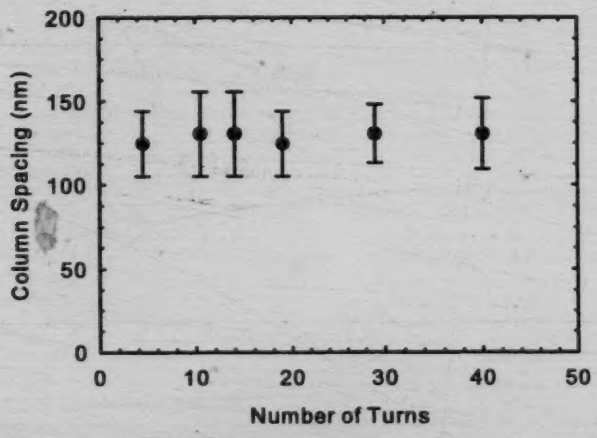

FIGURE 5.11

Effect of numbers of turns on inter-columnar spacing in helical Alq_3 films. The inter-columnar spaced in helical Alq_3 films varied little as additional turns were grown in a film. This provided quantitative evidence that the structural properties of helical Alq_3 films were fairly uniform with thickness.

Thus, highly porous nanostructured Alq_3 films were readily formed by fabricating samples at higher deposition angles, producing films with far fewer imperfections than comparably porous inorganic GLAD films. This may have been because the impinging vapor flux was in a thermodynamic regime that caused it to form smooth, amorphous droplets, and that encouraged subsequent flux to partially wet to these existing such droplets to minimize their surface energy. While the films were more porous at higher deposition angles, the cross-sectional shapes of the individual nanostructures varied little with deposition angle. The ability to form chiral thin films with controllable porosities and consistent nanostructural shapes may prove useful for future efforts at fabricating hybrid structures with GLAD films through the infiltration of LCs [19, 20] or dye molecules [21].

5.4 Variation of film porosity and column tilt angle with deposition angle

The variation of the film porosity with deposition angle was characterized for tilted columnar films using the same VASE analysis procedures [22] similar to those discussed in *Chapter 4*. In addition to determining the film porosity, this analysis was also used to determine the variation of the column tilt angle, β, and the principal indices of refraction (in *Chapter 6*) with deposition angle for the tilted columnar Alq_3 films. Again, the VASE analysis was performed in collaboration with James Gospodyn. The first stage of the VASE analysis consisted of determining an appropriate optical model for a solid Alq_3 film. This model was subsequently used to develop a biaxial effective medium model of the tilted columnar Alq_3 films. The models were fit to experimental reflection-mode Mueller matrix ellipsometry data acquired by VASE for angles of incidence in the range of 30 – 75°, and for wavelengths over the range of 300 – 1300 nm for each sample considered.

The solid Alq_3 film model consisted of the silicon substrate, an Alq_3 layer, and a surface roughness layer that was an effective medium composed of 50 % void and 50 % Alq_3 to model the effect of a non-flat surface to the top of the medium (Fig. 5.12). Oscillator models have been shown to yield good fits for VASE data of Alq_3 films in previous studies [23]. Thus, the Alq_3 layer was modeled using the combination of a single Lorentz oscillator and a single Tauc-Lorentz oscillator [24]. The imaginary part of the dielectric function contributed by the Lorentz oscillator was determined by Eq. 5.1, while the imaginary part contributed by the Tauc-Lorentz oscillator was given by Eq. 5.2. Note that Eq. 5.1 and 5.2 are both written for the case of single oscillators here. The real parts of both contributions were determined by the integration of the Kramers-Kronig relation for the imaginary parts [25].

$$\varepsilon_2(\omega) = \frac{AEC}{(E^2 - E_0^2)^2 + (EC)^2} \tag{5.1}$$

$$\varepsilon_2(\omega) = \begin{cases} \frac{1}{E}\frac{AEC}{(E^2 - E_0^2)^2 + (EC)^2} & \text{for } E > E_g \\ 0 & \text{for } E \le E_g \end{cases} \tag{5.2}$$

The best fit to the experimental data was obtained for a Lorentz oscillator with an energy (E_0) of 5.10 eV, an amplitude (A) of 36.46 eV^2, and broadening (C) of 0.09 eV, and a Tauc-Lorentz oscillator with an energy of 2.92 eV, an amplitude of 18.37 eV^2, broadening of 0.52 eV, and a band gap energy of 2.65 eV. The fitting process determined the thickness of the solid Alq_3 layer to be 249 nm, and the surface roughness layer was ~ 1 nm thick.

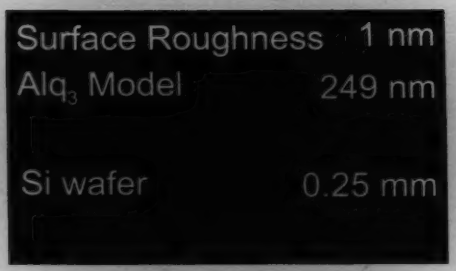

FIGURE 5.12

Optical model of solid Alq_3 film. The optical model used in the VASE analysis of the solid Alq_3 film consisted of the silicon substrate, an oscillator layer to describe the Alq_3 film, and a surface roughness layer. The oscillator layer consisted of one Lorentz oscillator and one Tauc-Lorentz oscillator. The surface roughness layer was an effective medium composed of 50 % void and 50 % Alq_3.

The combined Lorentz/Tauc-Lorentz model established for Alq_3 was then applied to the case of tilted columnar films (Fig. 5.13). The optical constants of the individual columns were assumed to obey the Lorentz/Tauc-Lorentz model. The biaxial nature of the films was addressed through the use of the coupled Bruggeman-biaxial layers. The Bruggeman effective medium layer was composed of void and Alq_3. The biaxial layer was coupled to the Bruggeman so as to enable the determination of the orientation of the columns. A solid layer of Alq_3 between the substrate and the Bruggeman-biaxial layer was also included to account for the wetting layer in each film. Finally, a surface roughness layer consisting of 50 % void and 50 % Alq_3 was included. The thickness values for the wetting layer, Bruggeman-biaxial layer, and surface roughness layer were all included as fit parameters. Additionally, the orientation angles of the columns (i.e. both the column tilt and the sample rotation), and the relative amounts of void and Alq_3 (i.e. the porosity) were also determined from the fits between the model and the data. As with the VASE modeling discussed in *Chapter 4*, the use of SEM data (both in terms of thickness values and column tilt angles) was used to confirm that the obtained fits were unique and realistic.

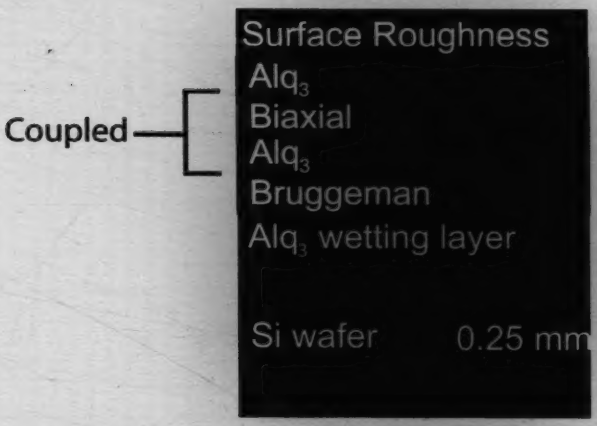

FIGURE 5.13

Optical model of a tilted columnar Alq_3 film. The optical model used in the VASE analysis of the tilted columnar Alq_3 films consisted of the silicon substrate, an Bruggeman effective medium layer, a biaxial layer that was coupled to the Bruggeman layer, and a surface roughness layer. The Bruggeman effective medium layer was a combination of void and Alq_3, with the Alq_3 being described by the oscillator model determined for a solid Alq_3 film.

The variation of the column tilt angle with deposition angle is shown in Fig. 5.14. The column tilt angle increased as the deposition angle increased, but the trend in the measured column tilt angles did not follow either Tait's rule [26] or the tangent rule [27]. The measured column tilt angles were higher than predicted by Tait's rule, reaching values as high as 76°. The reasons for this are not understood, as of yet. This behavior may be related to the absence of coarsening phenomena in the growth of the Alq_3 structures. The size of the Alq_3 clusters that impinge on the substrate may also play a role, as well as the mobility of the clusters upon the substrate. Additionally, the porosity increased with deposition angle (Fig. 5.15). A maximum porosity of ~ 65 % was obtained at a deposition angle of 89°. This variation of the porosity with deposition angle did not fit Tait's rule for porosity either. All of the measured porosities were significantly lower

than those predicted by Tait's rule. Other studies that compared inorganic GLAD films to Tait's rule similarly reported porosities lower than predicted by the theory [22, 26]. Also, the high column tilt angles displayed by the tilted columnar Alq_3 films suggested that such films might be useful for square spiral-based three-dimensional photonic crystal structures. Some geometries of square spiral photonic crystals require higher column tilt angles than are achievable with the growth of inorganic GLAD films [28, 29]. Alq_3 square spirals could possibly be fabricated with the desired column tilt angles, and the processed following deposition to form an high refractive index mold of the Alq_3 square spirals that would act as the photonic crystal.

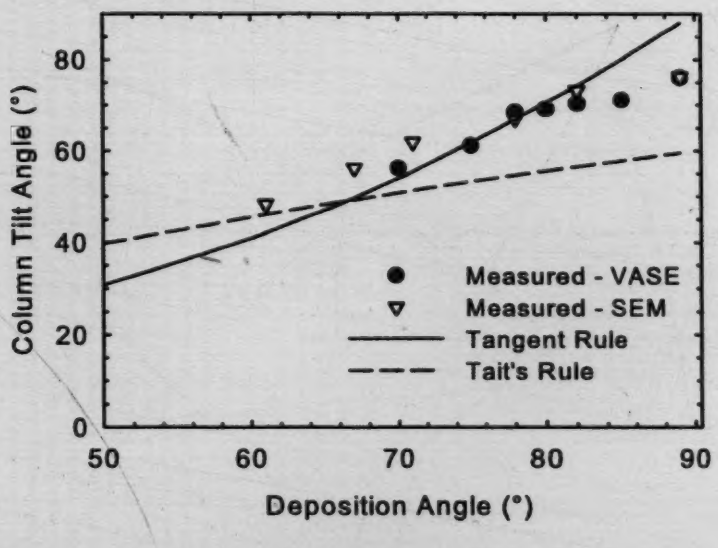

FIGURE 5.14

Effect of deposition angle on column tilt angle in tilted columnar Alq_3 films. Data sets were measured by both VASE and SEM analysis. Neither Tait's rule nor the tangent rule quantitatively fit the data. Notably, the measured tilt angles reached values higher than predicted by Tait's rule. No error bars are displayed because the 90 % confidence limits calculated as part of the VASE analysis give error bars that are smaller than the symbols plotted.

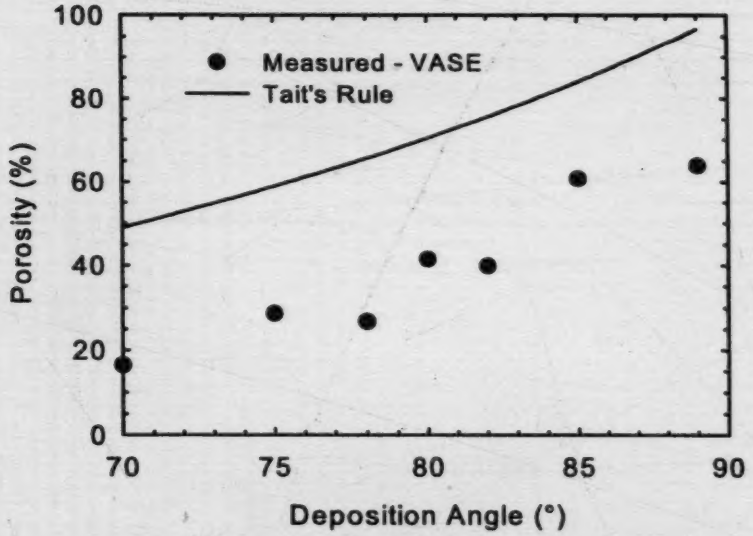

FIGURE 5.15

Effect of deposition angle on porosity in tilted columnar Alq_3 films. The porosity determined by VASE analysis of tilted columnar Alq_3 films was compared to Tait's rule for porosity (Eq. 4.8 in Chapter 4). The measured data followed a trend similar to Tait's rule. However, Tait's rule predicted high porosities than those that were observed. No error bars are displayed because the 90 % confidence limits calculated as part of the VASE analysis give error bars that are smaller than the symbols plotted.

5.5 Summary

Novel nanostructured organic films were fabricated by depositing Alq_3 films with the GLAD technique. These were the first directly deposited organic nanostructured films with controllable porosities. In addition to fundamentally altering the types of materials that can be used to directly deposit porous nanostructured material, the nanostructured Alq_3 films were found to exhibit a number of remarkable structural properties. This was

because these films grew through a different nucleation and ripening process than the inorganic materials typically used to deposit GLAD films. Specifically, direct ripening effects during the nucleation stage of growth and the absence of coarsening phenomena allowed nanostructured Alq_3 films to form an array of smooth, uniform structures which did not broaden with increased film thickness for morphologies such as tilted columnar and helical thin films. The individual helical structures in helical Alq_3 films also exhibited a nearly hexagonal close-packed order because of the direct ripening effects during the initial growth of the film, and the substrate rotation. Films grown on polar substrates, such as glass or as-supplied silicon substrates, included an initial solid wetting layer because the polarity of the substrate was a good match to that of the deposited molecules. Deposition onto hydrophobic or apolar substrates prevented the formation of such a wetting layer. The ability to tune the chemical nature of the substrate and to introduce lithographically defined topography to the substrate could allow for the growth of nanostructured Alq_3 films in non-hexagonal periodic arrays, potentially increasing the range of applications for which these films may ultimately be used. The smooth, ordered and non-broadening helical Alq_3 films suggest that these films may be useful as chiral optical materials. The high porosities (~ 65 %) achievable may be useful for potential applications in hybrid optical devices involving the infiltration of LCs or dye molecules. Similarly, the high column tilt angles (~ 75°), which reached values higher than those predicted by theory, encourage the use of these nanostructured organic thin films as templates for square spiral photonic crystals. The initial application which was focused upon for this thesis was the chiral optical properties of the chiral Alq_3 films, including the selective transmittance of circularly polarized light and the emission of circularly polarized photoluminescence (*Chapter 6*).

References

1. K. D. Harris, K. L. Westra, and M. J. Brett, "Fabrication of perforated thin films with helical and chevron pore shapes," *Electrochemical and Solid State Letters*, **4**, C39 (2001).

2. A. L. Elias, K. D. Harris, C. W. M. Bastiaansen, D. J. Broer, and M. J. Brett, "Large-area microfabrication of three-dimensional, helical polymer structures," *Journal of Micromechanics and Microengineering*, **15**, 49 (2005).

3. S. Pursel, M. W. Horn, M. C. Demirel, and A. Lakhtakia, "Growth of sculptured polymer submironwire assemblies by vapor deposition," *Polymer*, **46**, 9544 (2005).

4. I. Hodgkinson and Q.H. Wu, "Serial bideposition of anisotropic thin films with enhanced linear birefringence," *Applied Optics*, **38**, 3621 (1999).

5. M. Brinkmann, F. Biscarini, C. Taliani, I. Aiello, and M. Ghedini "Growth of mesoscopic correlated droplet patterns by high-vacuum sublimation," *Phyiscal Review B*, **61**, R16 339 (2000).

6. M. Brinkmann, S. Graff, and F. Biscarini, "Mechanism of nonrandom pattern formation of polar-conjugated molecules in a partial wetting regime," *Physical Review B*, **66**, 165430 (2002).

7. J. A. Venables, G. D. T. Spiller, and M. Hanbücken, "Nucleation and growth of thin films," *Reports on Progress in Physics*, **47**, 399 (1984).

8. T. M. Rogers, K. R. Elder, and R. C. Desai, "Droplet growth and coarsening during heterogeneous vapor condensation," *Physical Review A*, **38**, 5303 (1988).

9. J. A. Blackman and P. A. Mulheran, "Scaling behavior in submonolayer film growth: a one-dimensional model," *Physical Review B*, **54**, 11681 (1996).

10. E. Ruckenstein and D. B. Dadyburjor, "Direct ripening of crystallites on a substrate," *Thin Solid Films*, **55**, 89 (1978).

11. O. Krichevsky and J. Stavans, "Correlated Ostwald ripening in two dimensions," *Physical Review Letters*, **70**, 1473 (1993).

12. ImageJ, image processing freeware, available at http://reb.info.nih.gov/ij/.

13. M. Malac, R. F. Egerton, M. J. Brett, and B. Dick, "Fabrication of submicrometer regular arrays of pillars and helices," *Journal of Vacuum Science and Technology B*, **17**, 2671 (1999).

14. B. Dick, M. J. Brett, T. J. Smy, M. R. Freeman, M. Malac, and R. F. Egerton, "Periodic magnetic microstructures by glancing angle deposition," *Journal of Vacuum Science and Technology A*, **18**, 1838 (2000).

15. M. O. Jensen and M. J. Brett, "Periodically structured glancing angle deposition thin films," *IEEE Transactions on Nanotechnology*, **4**, 269 (2005).

16. M. O. Jensen and M. J. Brett, "Functional pattern engineering in glancing angle deposition thin films," *Journal of Nanoscience and Nanotechnology*, **5**, 723 (2005).

17. K. Kaminska, A. Amassian, L. Martinu, and K. Robbie, "Growth of vacuum evaporated ultraporous silicon studied with spectroscopic ellipsometry and scanning electron microscopy," *Journal of Applied Physics*, **97**, 013511 (2005).

18. D. Vick, T. Smy, and M. J. Brett, "Growth behavior of evaporated porous thin films," *Journal of Materials Research*, **17**, 2904 (2002).

19. J. C. Sit, D. J. Broer, and M. J. Brett, "Alignment and switching of nematic liquid crystals embedded in porous chiral thin films," *Liquid Crystals*, **27**, 387 (2000).

20. S. R. Kennedy, J. C. Sit, D. J. Broer, and M. J. Brett, "Optical activity of chiral thin film and liquid crystal hybrids," *Liquid Crystals*, **28**, 1799 (2001).

21. N. G. Wakefield, A. L. Elias, M. J. Brett, and J. C. Sit, "Optical behaviour of hybrid LC/inorganic nanostructures," *SPIE Proceedings*, **6135**, in press (2006).

22. J. Gospodyn and J. C. Sit, "Characterization of dielectric columnar thin films by variable angle Mueller matrix and spectroscopic ellipsometry," *Optical Materials*, in press (2006).

23. A. B. Djurišić, C. Y. Wong, W. L. Guo, T. W. Lau, E. H. Li, Z. T. Liu, H. S. Kwok, L. S. M. Lam, and W. K. Chan, "Spectroscopic ellipsometry of the optical functions of *tris* (8-hydroxyquinoline) aluminum (Alq_3)," *Thin Solid Films*, **416**, 233 (2002).

24. G. E. Jellison, Jr. and F. A. Modine, "Parameterization of the optical functions of amorphous materials in the interband region," *Applied Physics Letters*, **69**, 371 (1996).

25. J. D. Jackson, *Classical Electrodynamics*, Wiley, New York (1999).

26. R. N. Tait, T. Smy, and M. J. Brett, "Modelling and characterization of columnar growth in evaporated films," *Thin Solid Films*, **226**, 196 (1993).

27. H. van Nieuwenhuizen and H. B. Haanstra, "Microfractography of thin films," *Philips Technical Review*, **27**, 87 (1966).

28. S. R. Kennedy, "Photonic applications of nanostructured thin films," *Ph.D. Dissertation*, University of Alberta (2003).

29. M. O. Jensen, "Photonic crystal engineering in glancing angle deposition thin films," *Ph.D. Dissertation*, University of Alberta (2004).

CHAPTER 6
Optical characterization of nanostructured Alq_3 thin films

This chapter discusses the key results of the optical characterization of chiral Alq_3 thin films. The findings presented outline the physical basis for the form birefringence exhibited by tilted columnar Alq_3 thin films, as determined from the variation of the principal indices of refraction of tilted columnar Alq_3 thin films with deposition angle. The variation of the principal indices of refraction with deposition angle was then used to understand the strength variation of the circular Bragg phenomena exhibited by chiral Alq_3 thin films with deposition angle. This information aided in the design and fabrication of chiral Alq_3 thin films with large numbers of turns which exhibited circular Bragg phenomena with magnitudes of 98% in transmittance and 71% for photoluminescence.

6.1 Optical characterization methods

Two main optical characterization techniques were used in studying nanostructured Alq_3 thin films – spectroscopic ellipsometry and Stokes polarimetry, with the former used to determine the transmittance mode characteristics of the samples and the latter being used to probe the photoluminescent mode characteristics. Variable angle spectroscopic ellipsometry was utilized to determine the principal indices of refraction of tilted columnar Alq_3 thin films.

6.1.1 Variable angle spectroscopic ellipsometry

As in *Chapter 4*, the principal indices of refraction, n_x, n_y, n_z, of a tilted columnar thin film are defined as the index perpendicular to the deposition plane, the index perpendicular to the columns but within the deposition plane, and the index along the columns, respectively. Figure 6.1 provides a schematic depiction of a tilted columnar Alq_3 film with x-, y-, and z-axes labeled relative to the columns. Knowledge of the principal indices enables the determination of the normal incidence birefringence of tilted columnar thin films (see Eqns. 4.9 and 4.10 in *Chapter 4*) [1]. This is useful because it has been theoretically demonstrated that the strength of the circular Bragg phenomena exhibited by helical films produced by GLAD or SBD is proportional to the square of the local birefringence of the helical structures [2], and the normal incidence birefringence of a tilted columnar thin film is a close approximation of this local birefringence [3]. The principal indices of refraction of tilted columnar thin films can be determined through VASE analysis [4], as shown in earlier sections. The VASE models developed in *Chapter 5* for tilted columnar Alq_3 films were used to determine the principal indices of refraction of various tilted columnar Alq_3 samples..

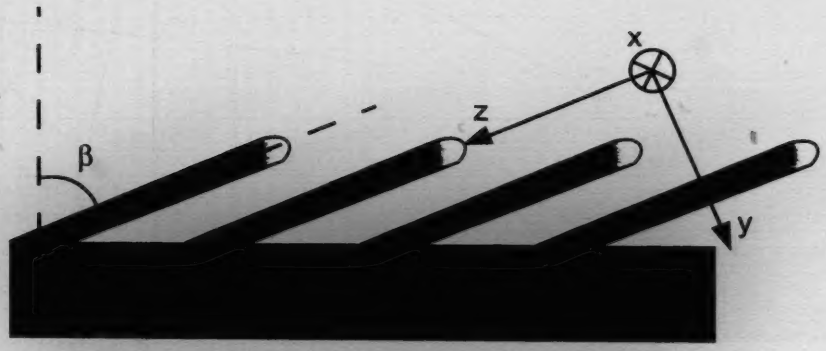

FIGURE 6.1
Schematic diagram of a tilted columnar thin films fabricated using GLAD. The axes of the principal indices of refraction and the column tilt angle are depicted.

6.1.2 Transmittance-mode spectroscopic ellipsometry

To measure the polarization behavior of light transmitted through the films, the same methods as used in *Chapter 4* were implemented. These allowed T_{LCP} and T_{RCP} to be determined, as well as the selective transmittance of circularly polarized light, which provided a clear indication of the presence of circular Bragg phenomena.

6.1.3 Stokes polarimetry

The characterization of the polarization state of the photoluminescent output of the samples was carried out using Stokes polarimetry [5]. For Alq_3 nanostructured films, however, the experimental photoluminescence apparatus depicted in *Chapter 4* could not be used because the films were easily damaged by the pulsed laser excitation. Even the minimum fluence of the 266 nm pulsed laser excitation that would yield a detectable photoluminescence signal was high enough to significantly damage the films (Fig. 6.2).

The nature of this damage was not thoroughly investigated here, but appeared to be similar to other reported observations of surface damage from nanosecond pulsed lasers [6, 7]. Thus, the characterization of the polarized photoluminescence was achieved using a less intense, continuous wave laser diode as the excitation source. The apparatus used for characterizing the photoluminescence of the Alq_3 samples is depicted in Fig. 6.3.

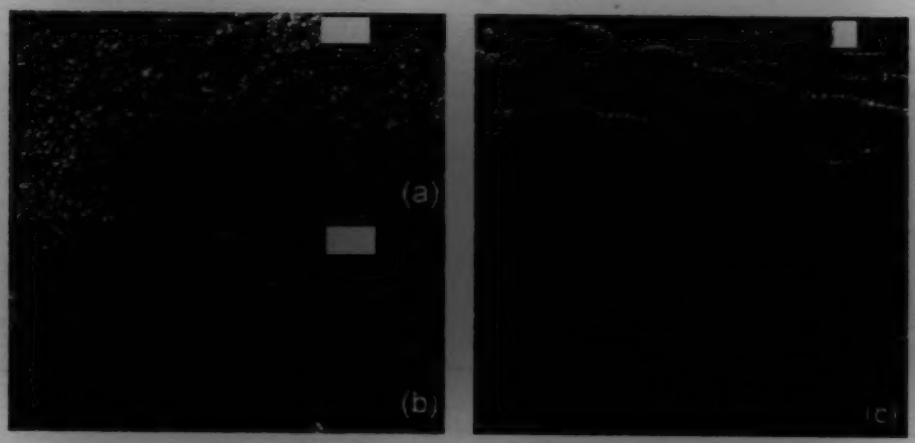

FIGURE 6.2

Laser damage in nanostructured Alq_3 films. A comparison of (a) a region of a tilted columnar film that wa not been exposed to laser excitation from a pulsed 266 nm laser to (b) a region that was in the beam path is shown. Laser damage was observed in (b), as well as for (c) a helical film exposed to the same laser excitation. Note that (a) and (b) were simply different region of the same sample, and the orientation and magnification of the sample was the same in both images.

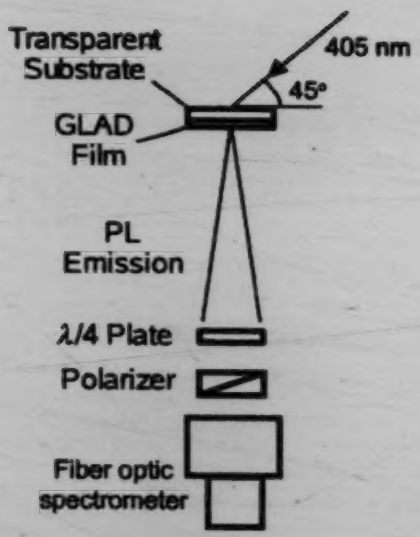

FIGURE 6.3

Schematic diagram of the photoluminescence detection and Stokes polarimetry apparatus. A laser diode with an emission wavelength of 405 nm was used to excite the sample. The energy of the beam was controlled by two partially-crossed Glan-Taylor polarizers (not shown). The polarization state of the luminescent emission was characterized by placing an achromatic quarter waveplate and a Glan-Taylor polarizer in the output beam path.

An AlGaN laser diode (B&Wtek Inc.) with an emission wavelength of 405 nm served as the excitation source. The beam energy incident upon the samples was limited using two partially-crossed Glan-Taylor polarizers. The photoluminescent emission from the sample was passed through an achromatic quarter waveplate and a Glan-Taylor polarizer and then coupled to a spectrometer (SD2000, Ocean Optics) via a fiber optic cable. The intensity measured by the spectrometer was a function of the rotational positions of the quarter waveplate and the Glan-Taylor polarizer. One can determine

orientations, relative to the sample, of the quarter waveplate and polarizer that can be used to measure the Stokes parameters of the photoluminescent light emitted by the samples (see *Appendix C* for details). Because the grating in the spectrometer was known to exhibit a polarization-dependent reflectivity, the rotational orientation of the Glan-Taylor polarizer in the output beam path was fixed. The sample and quarter waveplate were instead rotated to positions that enabled the measurement of each of the Stokes parameters. From the measured Stokes parameter, the overall degree of polarization, ρ, and the degree of circular polarization, ρ_c, can be determined (these were defined previously in Eq. 4.6 in *Chapter 4*).

6.2 Principal indices of refraction of tilted columnar Alq_3 thin films

Using the models developed in *Chapter 5* for determining the column tilt angle, β, and the porosity of the tilted columnar Alq_3 thin films, the principal indices of refraction were determined for the samples listed in Table 6.1. Examples of the dispersions of the principal indices of refraction for samples B ($\alpha = 75^\circ$), D ($\alpha = 80^\circ$), and F ($\alpha = 85^\circ$) are given in Fig. 6.4. The principal indices tended to decrease for wavelengths longer than ~ 425 nm, though a pronounced peak was observed near 425 nm. This peak arose because the solid Alq_3 films were best modeled by an oscillator model with an oscillator that had a spectral location near this wavelength (see *Chapter 5* for details) [8]. This was consistent with the results of A. B. Djurišić *et al.* [8] and C. Himcinschi *et al.* [9], which both found peaks in the index of refraction of solid Alq_3 films near 425 nm. However, the values for the indices obtained in the Djurišić and Himsinschi studies were higher than those observed in Fig. 6.4 owing to the solid nature of their films. Figure 6.4 also

demonstrates how the films deposited at higher deposition angles had lower principal indices of refraction for a given wavelength because such films were more porous than those fabricated at lower deposition angles. This was in keeping with effective medium theory, which assumes that the refractive index of a mixed medium will be a weighted average of the refractive indices of the component media of which the mixture is comprised. At higher porosities, a greater amount of the medium was low-index void, which resulted in a lower effective refractive index.

TABLE 6.1

Tilted columnar Alq_3 films fabricated at various deposition angles.

Sample	Nanostructure Type	Deposition Angle (°)	Thickness (nm)
A	Tilted columnar	70	600
B	Tilted columnar	75	650
C	Tilted columnar	78	2730
D	Tilted columnar	80	460
E	Tilted columnar	82	2160
F	Tilted columnar	85	605
G	Tilted columnar	89	1295

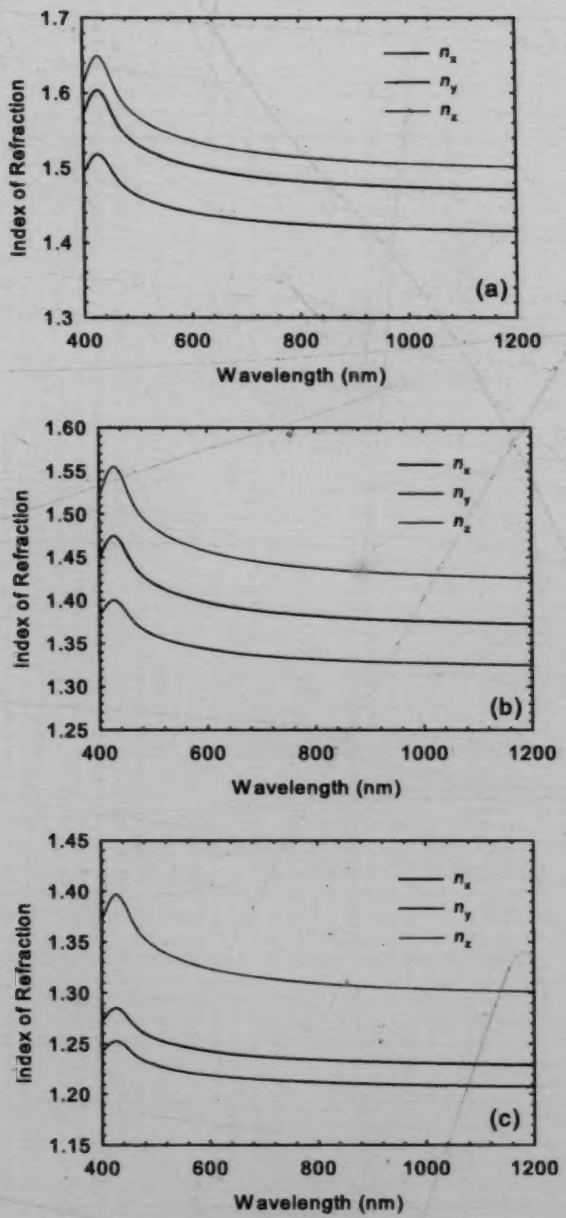

FIGURE 6.4

Dispersion of the principal refractive indices of tilted columnar Alq_3 films. The spectral variation of the principal indices of refraction for tilted columnar Alq_3 thin films deposited at (a) 75°, (b) 80°, and (c) 85°. Note that the magnitude of the indices decreased with deposition angle, while the separation between n_z and n_x increased with deposition angle.

Figure 6.5 depicts the variation in the principal refractive indices with deposition angle at a wavelength of 525 nm. As would be expected, all three principal indices tended to decrease with deposition angle while also obeying the relation $n_y < n_x < n_z$. There was some skew to the data, however: the indices measured for the thicker samples ($\alpha = 78°$ and $\alpha = 82°$) seemed to be higher than would be expected for the trend given by the other data points. This was likely due to increased scattering from the thicker samples which resulted in poorer fits for the VASE analysis for these data points because the VASE analysis could not account for scattering [4]. The refractive index differences (n_x-n_y, n_z-n_y, n_z-n_x) and normal incidence birefringence, Δn, were determined from the principal indices (Fig. 6.6). The normal incidence birefringence was found to be negative, and to become increasingly negative at higher deposition angles. The birefringence reached a magnitude ($|\Delta n|$) greater than 0.07 for the sample deposited at 89°. This was in contrast to inorganic tilted columnar thin films for which the normal incidence birefringence was found to be positive and reached a maximum for deposition angles in the range $60° < \alpha < 70°$ [1]. The values of $|\Delta n|$ observed for the Alq_3 films were quite strong for films deposited at $\alpha \geq 75°$, but they were only about half of the highest value reported for TiO_2 and Ta_2O_5 fabricated by SBD at lower deposition angles [10]. This was because the form birefringence of these biaxial thin films has been shown to depend on the index contrast between the material of the nanostructures (Alq_3 and TiO_2) and the medium surrounding the nanostructures (air) [11]. Given that the bulk index of refraction of a solid Alq_3 is ~ 1.7, compared to the considerably higher bulk index of TiO_2 (~ 2.8 [12]) it was not surprising that the birefringence of the Alq_3 structures was less than that achieved by SBD TiO_2 structures.

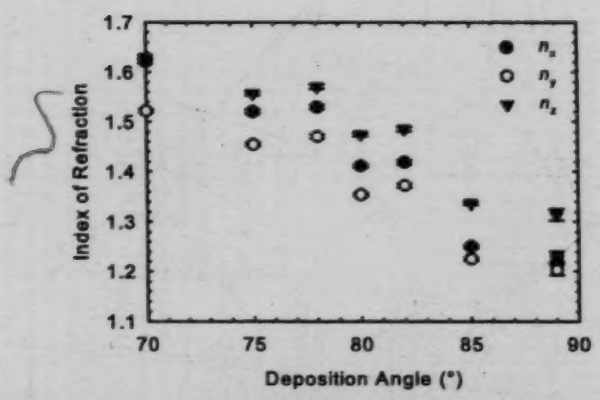

FIGURE 6.5

Variation of the principal indices of refraction of tilted columnar Alq_3 thin films with deposition angle. The principal indices shown were measured at a wavelength of 525 nm. The error bars were based on the 90 % confidence limits calculated as part of the VASE analysis. The indices of the thicker samples ($\alpha = 78°$ and $\alpha = 82°$) tended to be higher than the rest of the samples, likely as a result of increased scattering in these samples.

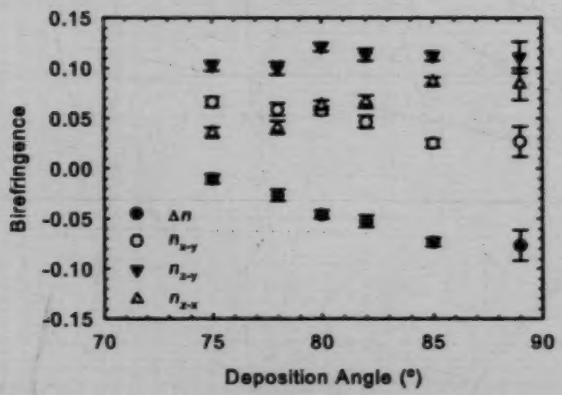

FIGURE 6.6

Variation of the birefringence of tilted columnar Alq_3 thin films with deposition angle at a wavelength of 525 nm. The differences n_{x-y}, n_{z-y}, n_{z-x}, and the normal incidence birefringence are shown. The error bars were based on the 90 % confidence limits calculated as part of the VASE analysis. The magnitude of the normal incidence birefringence increased with deposition angle.

The discrepancy between the sign of the normal incidence birefringence of organic and inorganic titled columnar thin films was a result of the geometries present in these two situations. When viewed along the z-axis of the columns, inorganic tilted columnar films exhibit a fan-shaped cross-section (Fig. 6.7a) [13]. This is because the self-shadowing effect is not present in the direction perpendicular to the deposition plane. When viewed at normal incidence to the substrate, the cross-sections of the columns for such inorganic tilted columnar thin films are still essentially fan shapes with their long axes aligned perpendicular to the deposition plane. As the posts of organic tilted columnar thin films are essentially domed cylinders that are tilted over at an angle, β, the shapes they exhibit in a cross-section parallel to the substrate are ellipses with the long axes laying parallel to the deposition plane (Fig. 6.8). Thus, $|\Delta n|$ should increase with increasing deposition angle for the Alq_3 samples as the columns are tilted farther over (i.e. as β increases with α, as per *Chapter 5*) because the ellipses will have a larger anisotropy at higher deposition angles. The long axes of these ellipses would then be parallel to the deposition plane. Hence, the normal incidence birefringence of tilted columnar Alq_3 films had the opposite sign when compared to inorganic tilted columnar films.

FIGURE 6.7

SEM micrographs of the column cross-sections of inorganic and organic tilted columnar thin films. (a) TiO_2 and (b) Alq_3 tilted columnar thin films are shown. The inorganic film was composed of structures with fan-shaped cross-sections because of the self-shadowing effect only acts in the deposition plane, not in the plane perpendicular to it. The Alq_3 film had structures with circular to slightly elliptical cross-sections.

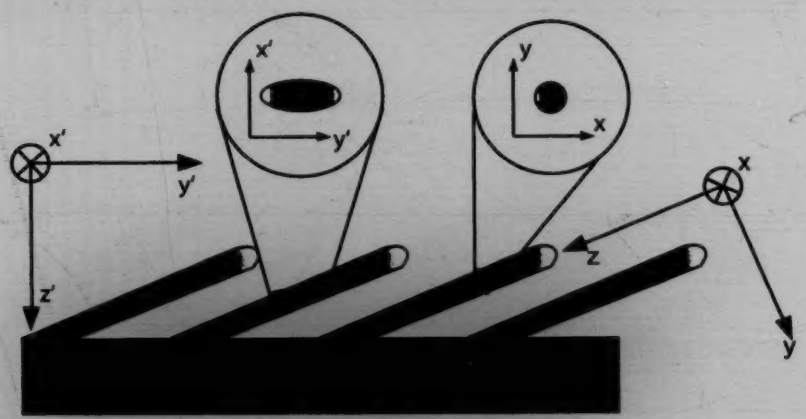

FIGURE 6.8

Schematic representation of the source of the normal incidence birefringence of tilted columnar Alq_3 thin films. When viewed along the z-axis (down the length of the columns) the structures are nearly circular. When viewed from the z'-direction (i.e. along the direction perpendicular to the substrate plane) the structure encountered is elliptical. The structures will become more elliptical for the z' view when the columns are tilted off normal more (i.e. when β is higher).

6.3 Degree of polarization of photoluminescent output from tilted columnar Alq_3 thin films

The Stokes parameters and overall degree of polarization of the photoluminescent output of samples C ($\alpha = 78^{\circ}$), E ($\alpha = 82^{\circ}$), and G ($\alpha = 89^{\circ}$) in Table 6.1 were determined and are shown in Fig. 6.9 for sample G. The maximum degree of polarization and the normal incidence birefringence (at a wavelength of 525 nm) observed are plotted in Fig. 6.10. The maximum overall degree of polarization increased with deposition angle in a manner similar to the variation of the normal incidence birefringence with deposition angle. The maximum observed overall degree of polarization was ~ 25 % and was measured for sample G. The degree of circular polarization (and S_3) for the same sample was near 0 %, which indicated that linear polarization components (S_1 and S_2) were the sole cause of the high overall degree of polarization.

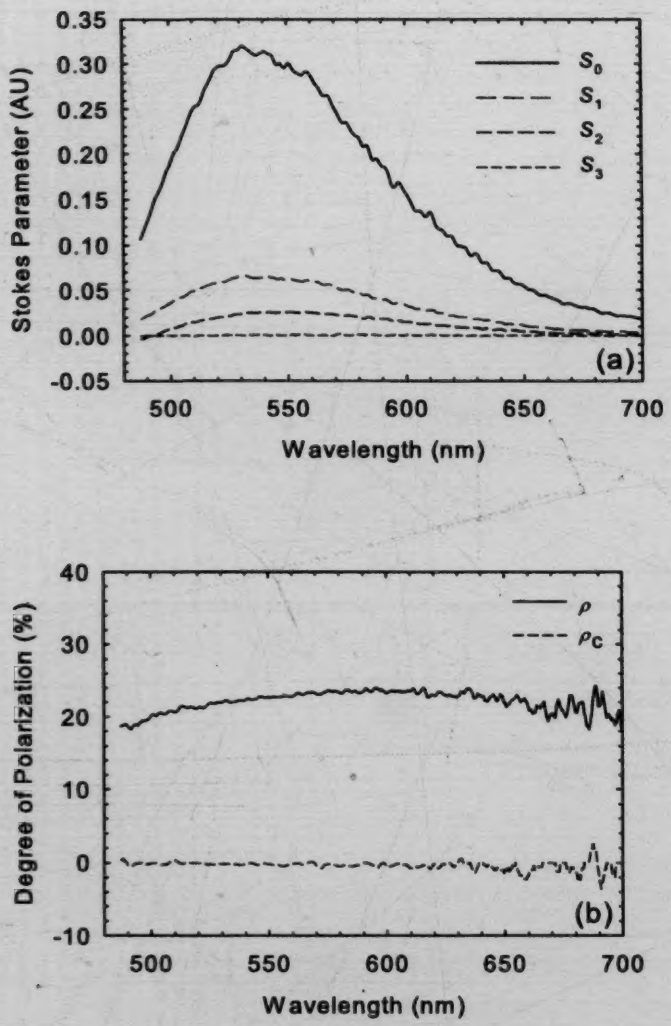

FIGURE 6.9

Spectral variation of (a) Stokes parameters and (b) degree of polarization for sample G. The S_1 and S_2 parameters were non-zero. The S_3 parameter was near zero for all wavelengths which resulted in no degree of circular polarization. Thus, the degree of polarization observed was caused by linearly polarized components.

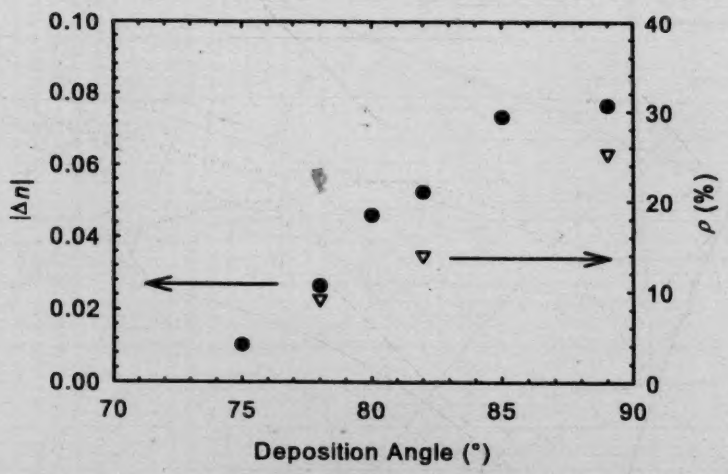

FIGURE 6.10

Variation of the magnitude of the normal incidence birefringence at $\lambda = 525$ nm and maximum overall degree of polarization of tilted columnar Alq_3 thin films with deposition angle. The maxmimum overall degree of polarization of the photoluminescent output is only shown for samples C ($\alpha = 78°$), E ($\alpha = 82°$), and G ($\alpha = 89°$) because the other samples were too thin to provide reliable data. The maximum overall degree of polarization increased with deposition angle in a fashion similar to the increase of $|\Delta n|$ with deposition angle.

6.4 Variation of circular Bragg phenomena with deposition angle in chiral Alq_3 thin films

The optical properties were characterized for a series of chiral Alq_3 thin films fabricated at a variety of deposition angles. These samples are listed in Table 6.2.

TABLE 6.2
Chiral Alq_3 films fabricated at various deposition angles.

Sample	Nanostructure Type	Deposition Angle (°)	Pitch (nm)	Thickness (nm)	Number of Turns
H	Helix (RH)	75	314	1350	4.3
I	Helix (RH)	76	365	1720	4.7
J	Helix (RH)	77	345	1380	4.0
K	Helix (RH)	78	307	1375	4.5
L	Helix (RH)	79	310	1360	4.4
M	Helix (RH)	80	316	1480	4.7
N	Helix (RH)	85	328	1630	5.0

Analysis of SEM micrographs obtained for these samples (*Chapter 5*) revealed that the porosity increased with deposition angle, as expected. Because the porosity is related to the average index of refraction, a film with higher porosity would be expected to exhibit a circular Bragg phenomenon at a lower wavelength than a similar film with lower porosity but the same pitch. Changes in pitch would also lead to the observation of circular Bragg phenomena at different wavelengths, with a larger pitch value leading to a circular Bragg phenomenon situated at a longer wavelength (see *Chapter 2*). Also, the strength of the circular Bragg phenomenon has been predicted to increase with the square of the birefringence and number of turns for the sample [2]. Note that for this sample set, the number of turns was approximately constant across the samples, and thus any variation in the strength of the circular Bragg phenomena observed for this set of samples was due to the relative refractive indices and birefringence of the samples, and

not to the number of turns present. Figure 6.11, which depicts the normalized selective transmittance of circularly polarized light through samples H, I, M, and N, demonstrates all of these effects. The spectra clearly demonstrate how the different pitches and deposition angles of samples I and N gave rise to an ~ 100 nm shift in the peak wavelength of the circular Bragg phenomena. Sample H (α = 75°) and sample M (α = 80°) had nearly identical values of pitch of 316 nm and 314 nm, respectively, but the increased deposition angle (decreased average refractive index) of sample M compared to sample H still led to an ~ 30 nm shift in peak wavelength of the circular Bragg phenomena. These shifts should be quantitatively predictable using Eq. 2.12, however, additional measurements of the effective indices of refraction of chiral films are necessary to produce reliable quantitative predictions. The chiral films all consisted of right-handed structures, so the RCP was reflected, absorbed, and scattered [14], and LCP light was preferentially transmitted. Additionally, higher values of $T_{\text{LCP-RCP}}$ were observed for the samples made at higher deposition angles.

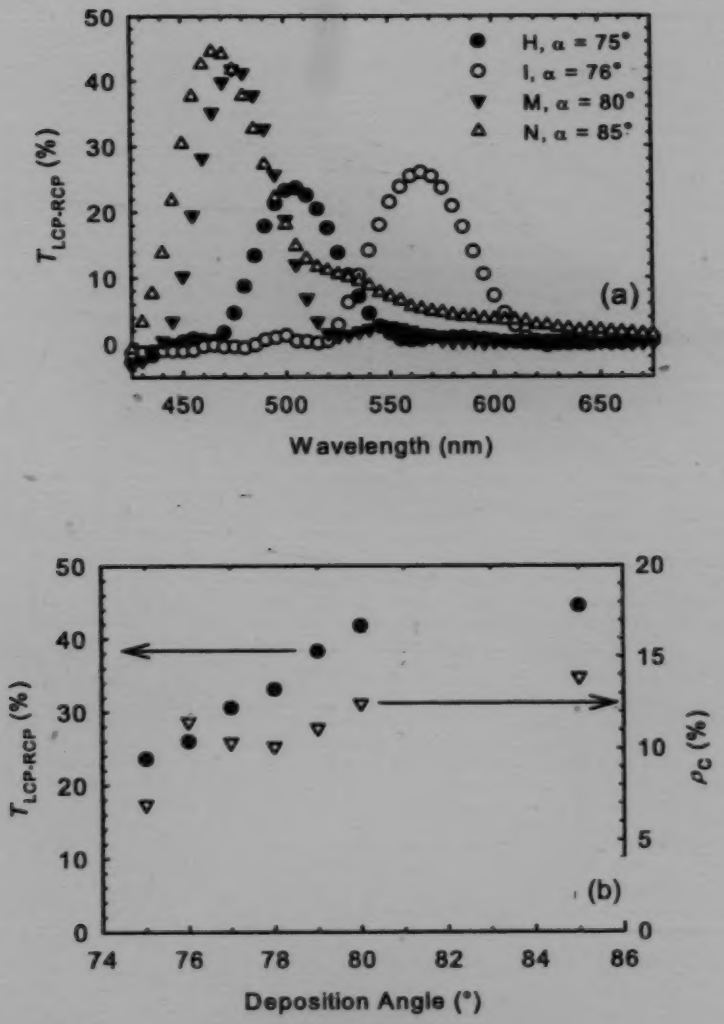

FIGURE 6.11

Dependence of circular Bragg effect strength and location upon film deposition angle. Spectra of the (a) normalized selective transmittance of circularly polarized light for samples H ($\alpha = 75°$), I ($\alpha = 76°$), M ($\alpha = 80°$), and N ($\alpha = 85°$) are shown. (b) The selective transmittance of circularly polarized light and degree of circular polarization of the photoluminescent output increased with deposition angle for all samples in Table 6.2. Note that the selective transmittance of circularly polarized light was normalized to the left-handed transmittance to minimize diffuse scattering contributions.

Similar results were obtained for measurements of the degree of circular polarization of the photoluminescent output of these samples in Fig. 6.11b. The circular Bragg phenomena were stronger for the transmittance measurements than for the photoluminescence measurements. This was because in transmittance the detected light traveled through the entire film structure, while for photoluminescence the light emission was likely somewhat localized, such that some of the detected light would not travel through the entire film structure [15].

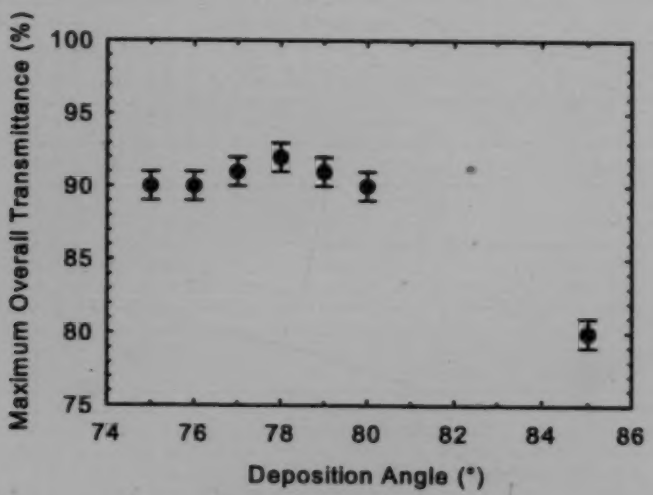

FIGURE 6.12

Evidence of increased scattering in chiral Alq_3 films deposited at higher angles of incidence. The maximum overall transmittance with deposition angle due to an increased level of scattering [14].

It should be noted that the selective transmittance of circularly polarized light was normalized to the LCP transmittance, to minimize diffuse scattering contributions. Scattering in inorganic helical GLAD films tends to increase as the films become more porous [14]. Figure 6.12 provides evidence of this for organic helical structure by showing the variation in the maximum overall transmittance with increasing deposition angle.

Thus, while the magnitudes of the circular Bragg phenomena increased with deposition angle, owing to a strong dependence on Δn, the use of films fabricated at deposition angles greater than 80° to produce strong circular Bragg phenomena was limited because of the increased scattering for such films.

6.5 Strong circular Bragg phenomena in thick chiral Alq_3 films

For chiral Alq_3 films to be used in applications such as circular polarization filters [3], circularly polarized light emitters [16, 17], or low-threshold lasers [18], the circular Bragg phenomena must be much stronger than was obtained for the samples listed in Table 6.2. These samples produced a maximum degree of circular polarization of ~ 14 % with a 5-turn helical structure deposited at 85°. One straightforward method of obtaining samples with stronger circular Bragg phenomena is to fabricate samples with more turns, thus adding more periods to the 1D photonic crystal formed by the chiral medium [3].

For inorganic chiral thin films fabricated at high deposition angles ($\alpha > 70°$), the benefit of adding more turns to a film is obtained only up to a certain thickness, after which the helical structure degrades and ceases to provide additional strengthening of the circular Bragg phenomenon [12, 19]. Since chiral Alq_3 films have been demonstrated not to broaden or undergo structural degradation even in films as thick as 10 μm, additional turns should serve to strengthen the circular Bragg phenomena in very thick films. The magnitudes of the circular Bragg phenomena of chiral Alq_3 films were shown to increase with deposition angle (Fig. 6.11), which would seem to suggest that highly porous, very thick chiral films would yield the strongest circular Bragg phenomena. However, scattering effects must also be considered. At higher deposition angles, scattering is more prominent, which would result in a decrease in overall transmittance. Furthermore,

scattering would be worse in thicker films because there are proportionally more air-film interfaces from which light could scatter. Thus, a compromise had to be made when selecting the deposition angle for fabricating chiral Alq_3 films that exhibit very strong circular Bragg phenomena. To explore the potential for fabricating chiral Alq_3 films exhibiting strong circular Bragg phenomena, samples were fabricated at a deposition angle of 78° with each sample having the same pitch but a different number of turns. These samples are listed in Table 6.3.

TABLE 6.3
Chiral Alq_3 films fabricated with various numbers of turns.

Sample	Nanostructure Type	Deposition Angle (°)	Pitch (nm)	Thickness (nm)	Number of Turns
O	Helix (RH)	78	344	1550	4.5
P	Helix (RH)	78	315	3310	10.5
Q	Helix (RH)	78	318	4455	14
R	Helix (RH)	78	317	6020	19
S	Helix (RH)	78	323	7910	24.5
T	Helix (RH)	78	285	8255	29
U	Helix (RH)	78	314	10210	32.5
V	Helix (RH)	78	317	12680	40

Examples of the LCP and RCP transmittance and photoluminescence, and $T_{LCP\text{-}RCP}$ and ρ_c spectra obtained for samples P (10.5 turns), R (19.5 turns), and V (40 turns) are shown in Fig. 6.13, 6.14, and 6.15, respectively. The minimum values of T_{RCP} and I_R were both observed for the sample V, and were 0.93 % and 0.614 (AU), respectively. This resulted in maximum observed values of $T_{LCP\text{-}RCP}$ and ρ_c of 98 % and 71 %, respectively – values much stronger than the best results obtained for the Y_2O_3:Eu samples. The many side-lobes present in the spectra of the 40-turn sample (and to a lesser degree the 19.5-turn sample) occurred because of interference effects common to interference

filters and similar structures. Additionally, it was found that the 10.5-turn film produced slightly enhanced emission for I_R at the long wavelength edge of the circular Bragg region, however this did not occur for the other samples. This enhanced emission was likely a manifestation of the Purcell effect [20]. This was only observed in 10.5-turn sample because the absorption of Alq_3 was quite high at 405 nm ($\sim 4 \times 10^4$ cm^{-1}) [21], such that most of the excitation light was absorbed in a small portion of the film. For samples thicker than the 10.5-turn sample, the excitation beam was likely absorbed too far from the center of the films to effectively couple the emitted light to the resonant modes necessary to observe the Purcell effect [22]. The 10.5-turn sample, on the other hand, did not exhibit a fully developed circular Bragg phenomenon, so the Purcell effect would only be weakly observed. This is discussed further in *Section 6.6*.

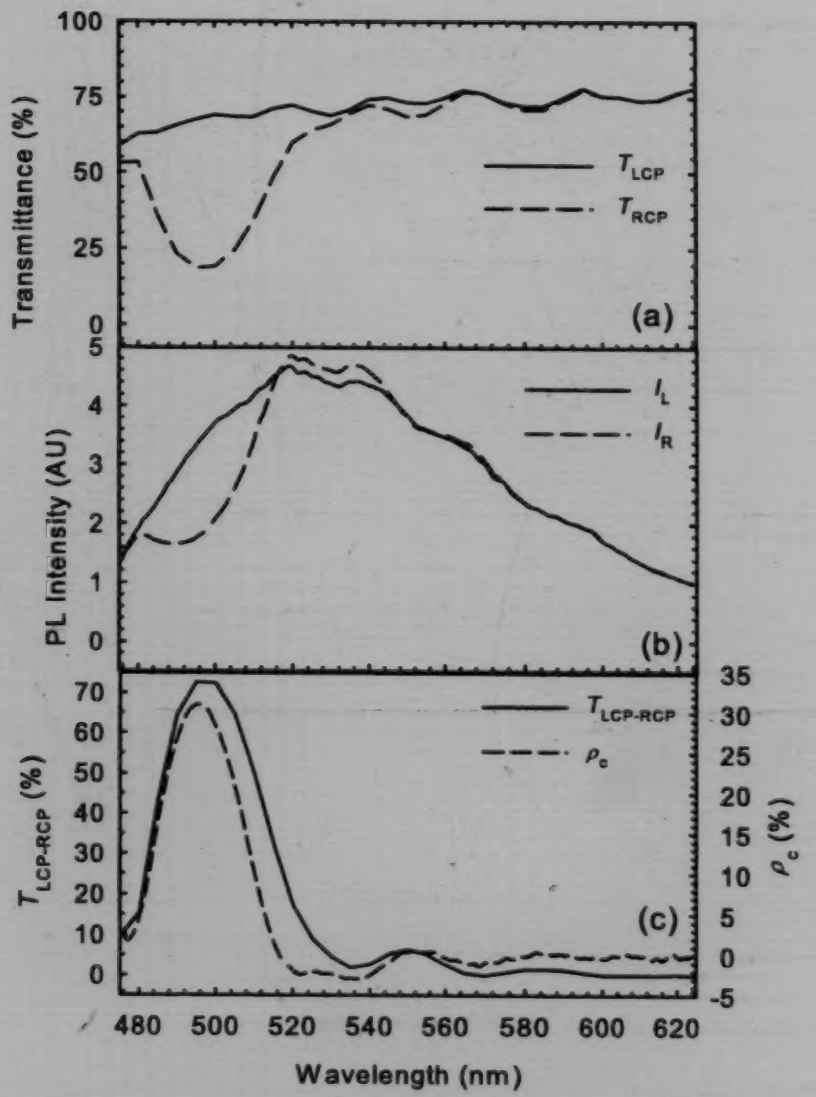

FIGURE 6.13

Circular Bragg phenomena in a 10.5-turn chiral Alq_3 sample. The (a) LCP and RCP spectra for transmittance, (b) photoluminescence, and (c) $T_{LCP-RCP}$ and ρ_c spectra are depicted. The RCP photoluminescent emission was slightly higher than the LCP emission at the long wavelength edge of the circular Bragg regime.

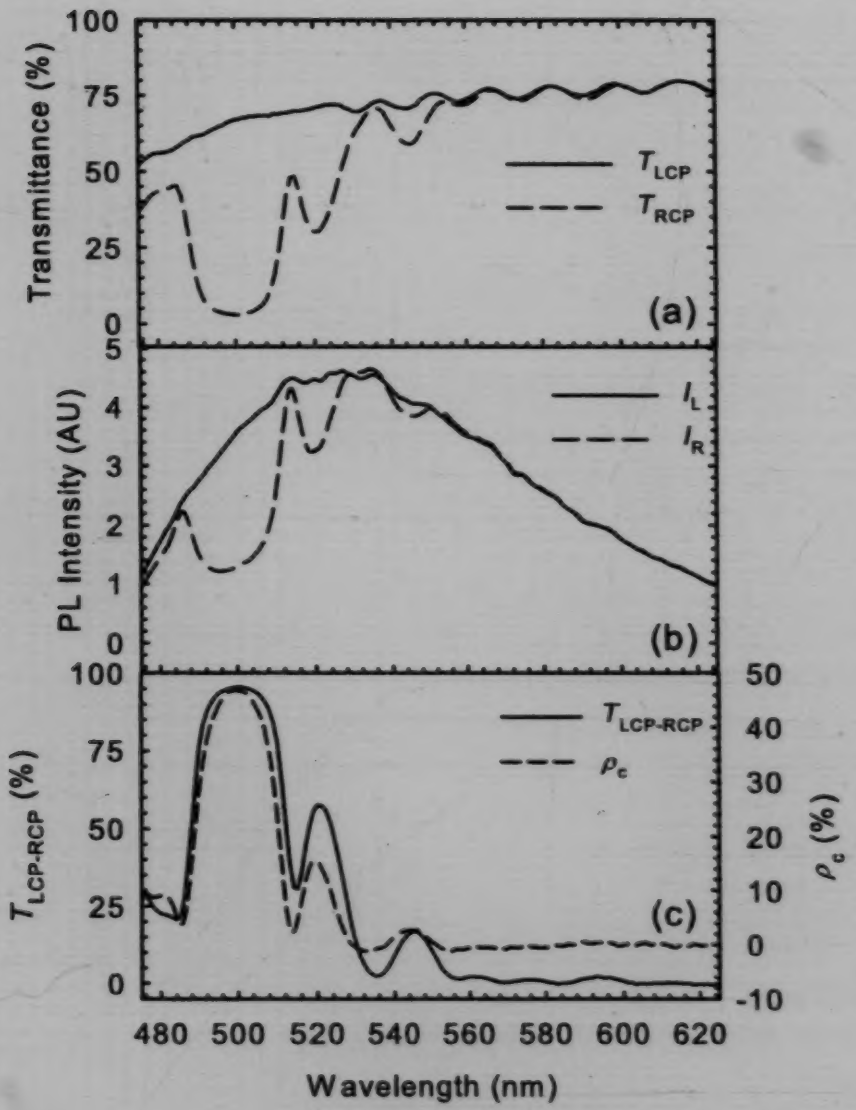

FIGURE 6.14

Circular Bragg phenomena in a 19-turn chiral Alq_3 sample. The (a) LCP and RCP spectra for transmittance, (b) photoluminescence, and (c) $T_{LCP-RCP}$ and ρ_c spectra are depicted. The strong circular Bragg effect for this film resulted a peak $T_{LCP-RCP}$ ~ 95 %. The peak ρ_c value was ~ 47 %. The bandwidth of the circular Bragg effect was ~ 25 nm in transmittance and ~ 20 nm for the photoluminescence data.

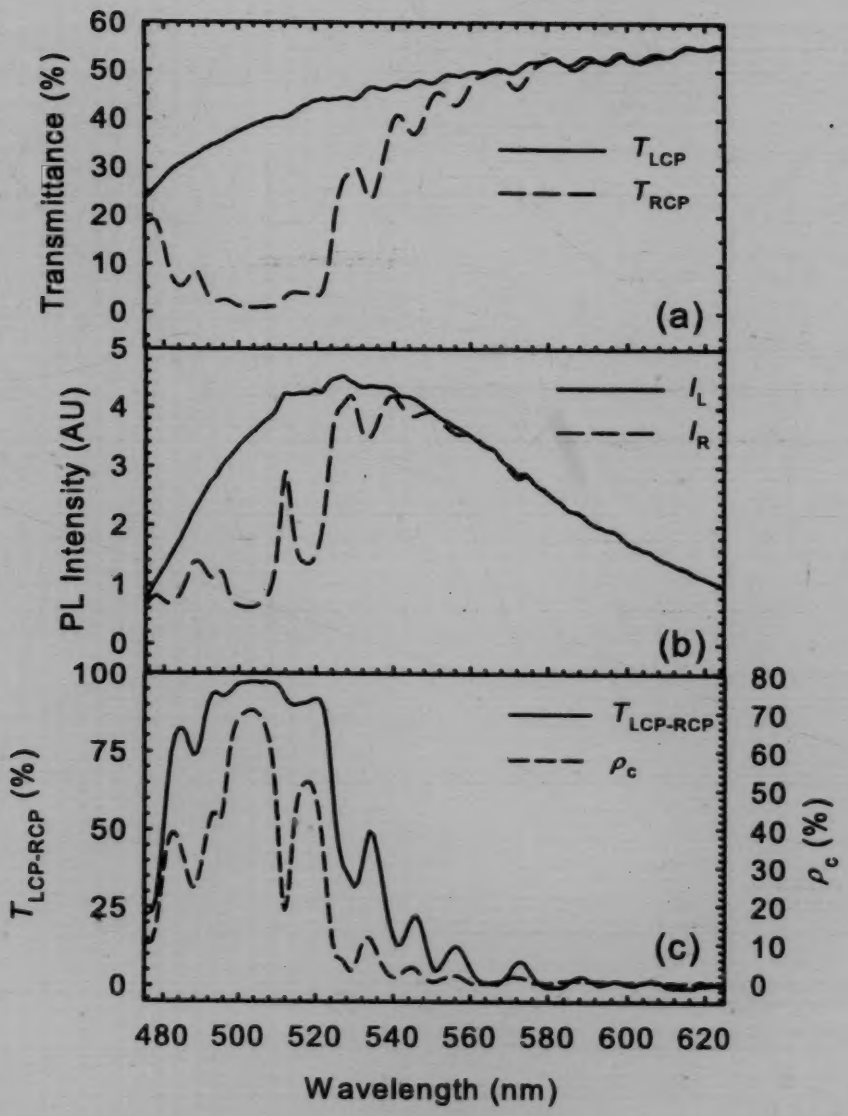

FIGURE 6.15

Circular Bragg phenomena in a 40-turn chiral Alq_3 sample. The (a) LCP and RCP spectra for transmittance, (b) photoluminescence, and (c) $T_{LCP-RCP}$ and ρ_c spectra are depicted. The strong circular Bragg effect for this film resulted a peak $T_{LCP-RCP}$ ~ 98 %. The peak ρ_c value was ~ 71 %. The bandwidth of the circular Bragg effect was ~ 46 nm in transmittance and ~ 20 nm for the photoluminescence data.

The full-width at half-maximum (FWHM) bandwidth of the circular Bragg phenomena seemed to increase with the number of turns for the transmittance data, but not for the photoluminescence data. The 19.5-turn sample had an ~ 15 nm bandwidth, while the 40-turn sample had an ~ 46 nm bandwidth for the transmittance measurements. The FWHM for the ρ_c data was ~ 20 nm for both the 19.5-turn and 40-turn samples. This discrepancy was likely a result of imperfections in the 40-turn sample that resulted in a range of pitches being present throughout the 40-turns of the sample. One such imperfection was the result of particulate impact during the deposition, which significantly degraded the structure (Fig. 6.16) and produced regions in which the pitch of the helices did not match the desired pitch. This structural degradation likely also had contributed to the decrease in overall transmittance of the samples with additional turn. This is because the distorted regions of the film seemed to have size scales (1 – 10 μm) that likely led to increased scattering from the films. Scattering from air-Alq_3 interfaces within the films also occurred, though, and was likely the dominant cause of the decreased transmittance of the thicker films.

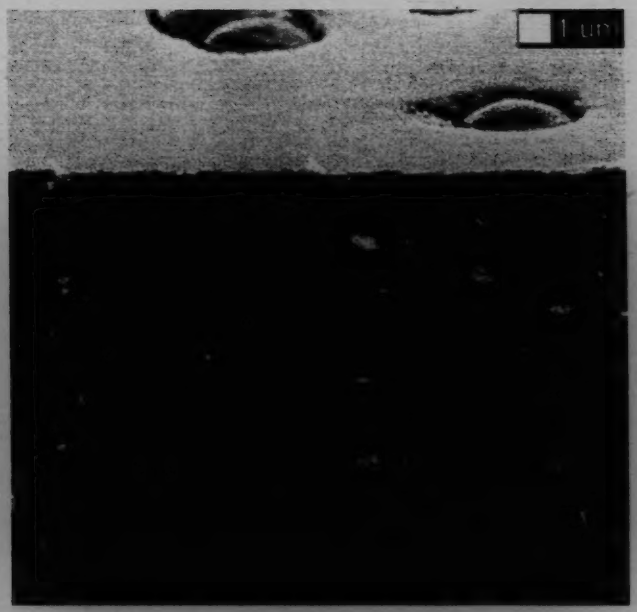

FIGURE 6.16

SEM image of surface damage that occurred during film deposition. The impact of particulate ejected from the evaporation source during film fabrication caused the formation of nodules on the film surface. The helical structures in the regions surrounding these nodules were distorted, which led to changes in the physical pitch of the structures in these regions. The nodules were also suspected to act as scattering centers.

The spectral distribution of the Stokes parameters of samples P, R, and V are depicted in Fig. 6.17. The linear polarization Stokes parameters, S_1 and S_2, were both non-zero, as shown in Fig. 6.17, but the magnitudes of S_1 and S_2 at any given wavelength tended to be low compared to the magnitude of S_3. As a result, the polarization state of the light emitted could be described as partially circularly polarized — some of the light emitted remained unpolarized, while only a small amount had linearly polarized components – or elliptically polarized.

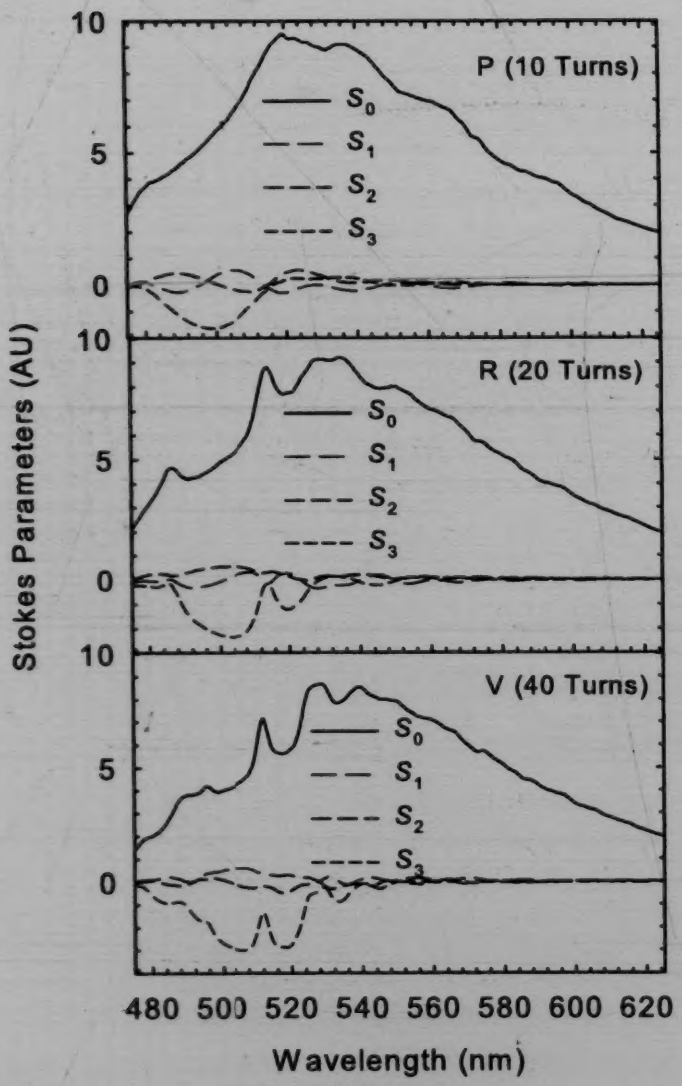

FIGURE 6.17

Measured Stokes parameters for various chiral Alq_3 films. The Stokes parameters of sample P (10.5 turns), R (19.5 turns), and V (40 turns) are depicted. The S_3 parameter was the strongest of the Stokes parameters (besides S_0) for each sample. The S_1 and S_2 parameters were non-zero in the spectral region of the circular Bragg phenomena, however they both tended to be close to zero. Because these parameters were non-zero, the polarization state of the emitted light could best be described as elliptically polarized or partially-circularly polarized.

Figure 6.18 shows the maximum values of $T_{LCP\text{-}RCP}$ and ρ_c for each of the samples listed in Table 6.3. $T_{LCP\text{-}RCP}$ increased rapidly to values > 90 % within the first 15 turns, and then leveled off at values of ~ 97 % after ~ 25 turns. On the other hand, ρ_c reached values of ~ 70 % after 40 turns. The trend for ρ_c seemed to indicate that further strengthening of the circular Bragg phenomena observed in the photoluminescent output could be achieved with the incorporation of additional turns. For both the transmittance and photoluminescence measurements, however, the strongest circular Bragg phenomenon was observed for the 40-turn film (sample V), for which $T_{LCP\text{-}RCP}$ = 98 % and ρ_c = 71 %.

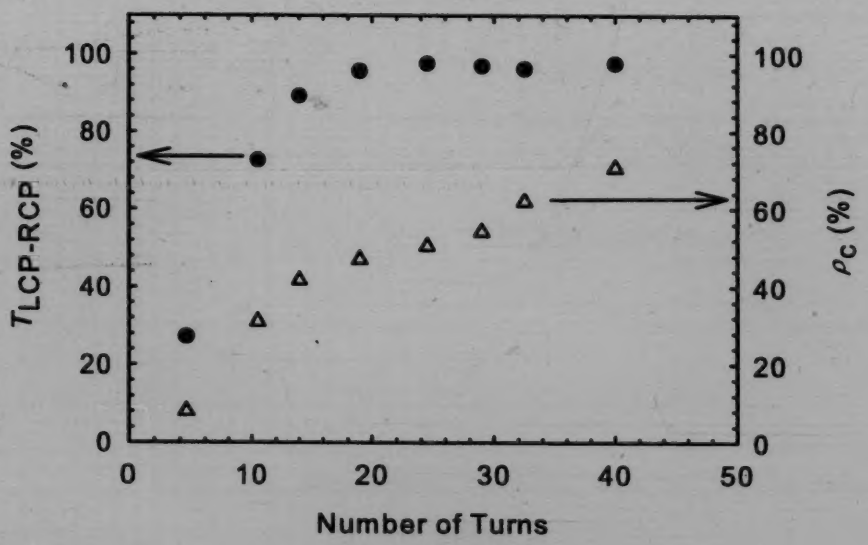

FIGURE 6.18

Variation of the maximum selective transmittance of circularly polarized light and degree of circular polarization with the number of turn. The maximum values of $T_{LCP\text{-}RCP}$ and ρ_c of the photoluminescent emission for each of the sample listed in Table 6.3 are shown. $T_{LCP\text{-}RCP}$ increased rapidly while ρ_c increased more slowly. The trend for ρ_c suggested that additional turns would result in further increases in this value.

Examining T_L/T_R and I_L/I_R also provided a useful metric for quantifying the strength of the circular Bragg phenomena produced by these films. These ratios quantify the degree to which the handedness of circularly polarized light that couples with the film structure is rejected (reflected, absorbed, or scattered). For use in applications, it is important to maintain a high transmittance of the handedness of light that is passed by the structure. However, it is also crucial to minimize the transmittance of the handedness of light that couples with the structure. These rejection ratios contain information that is equivalent to that presented for $T_{LCP\text{-}RCP}$ and ρ_c, but it is worthwhile considering these ratios as well, since they provide the most direct comparison to other published works on circular Bragg phenomena in chiral media. The maximum circular polarization ratios observed here were 43 and 5.8, for transmittance and emission, respectively, and were both observed for the 40-turn sample. Table 6.4 provides some perspective of how the observed results compared with other published values for circular Bragg phenomena in vacuum-deposited chiral thin films and in luminescent cholesteric LC and polymer media. The list of data provided for luminescent cholesteric LC and polymer media is not exhaustive, but nonetheless provides some insight into the potential offered by such techniques. Dense chiral TiO_2 films formed by SBD and cholesteric LC media yield superior circular Bragg phenomena when compared to the porous chiral Alq_3 films. These are, in turn, superior to chiral TiO_2 films formed by GLAD (@ $\alpha > 70°$). The circular Bragg phenomena of porous chiral Alq_3 films are on a similar scale to those of dense chiral TiO_2 films formed by SBD and cholesteric LC media, in spite of their porosity. At this stage of development, porous chiral Alq_3 films would be a poor choice for some optical applications. However, the ultimate advantage offered by such films is the combination of strong circular Bragg phenomena with high porosity. This can be exploited for sensing

applications, and to form hybrid media with device applications akin to the LC-chiral thin film hybrids that have been fabricated with inorganic chiral thin films produced by GLAD [23]. Furthermore, if similar chiral structures and circular Bragg phenomena can be demonstrated using other small molecule organics using the GLAD process, the potential offered by these novel materials is substantial owing to the enormous variety of organic materials which may be tailored for use in specific applications.

TABLE 6.4

Comparison between chiral optical properties of various chiral media.

Medium	T_{LCP}/T_{RCP}	l_t/l_a
Luminescent cholesteric LCs [17,22]	400	16
Dye-doped cholesteric LCs [24]	35	12
Chiral TiO_2 Fabricated by SBD [3]	160	n/a
Chiral TiO_2 Fabricated by GLAD [19]	6	n/a
Chiral Alq_3 Fabricated by GLAD [this thesis]	43	5.8

6.6 Potential for fabrication of enhanced spontaneous emission and low-threshold lasers using chiral Alq_3 films

Additional improvements in the magnitude of the circular Bragg phenomena yielded by Alq_3 chiral films could prove useful in developing such films for use in producing enhanced spontaneous emission [15, 17, 22, 24] and for low-threshold lasing applications [18]. Such an application would make use of the chiral film to obtain distributed feedback of one handedness of circularly polarized light. This leads to an observation of the Purcell effect, which is the enhancement of spontaneous emission at the edges of the stop band owing to the presence of non-trivial boundary conditions, such as those present in cavities or distributed feedback architectures [20]. Emission is

suppressed within the stopband, causing a build up of the photonic density of states at the band edges, thus enhancing emission at the band edges. The group velocity approaches zero at the band edge, leading to longer dwell times for the emitted photons, which enables stimulated emission from appropriately designed samples. When laser dye molecules, such as 4-(dicyanomethylene)-2-methyl-6-(4-dimethylamino styryl)-4H-pyran (DCM), are introduced as luminescent centers in a cholesteric LC film, enhanced spontaneous emission [24] and band edge lasing [25] can be observed. Lasing from such structures is explained by distributed feedback theory.

The observation of the Purcell effect from luminescent chiral structures is a necessary prerequisite to the fabrication of low-threshold band edge lasing devices based upon such structures. The Purcell effect has been observed in a variety of chiral material systems including dye-doped cholesteric LCs [15, 24], luminescent cholesteric LCs [17, 22], and dye-doped cholesteric polymers [26, 27]. Woon *et al.* have developed a highly birefringent luminescent glassy liquid crystalline material that has been observed to yield highly circularly polarized photoluminescence over a broad spectral range (> 110 nm) [17]. The high polarization ratios (400:1 for transmittance [28] and 16:1 for photoluminescence [17]) observed by Woon *et al.* and the broad spectral range over which circular Bragg phenomena are observed for their 3 μm thick samples are due to the high birefringence of their material system, which ranges from 0.65 at 475 nm to 0.35 at 600 nm [17]. In spite of their exceptional optical results, the Purcell effect was not readily observed from their highly birefringent luminescent cholesteric liquid crystal when excited by a 405 nm laser beam, but was easily observed for excitation by a 458 nm laser beam. This led Woon *et al.* to formulate a theoretical description that accounted for the wavelength dependence of the absorption of their samples [22]. In the case of 405-nm excitation, they observed

that the excitation beam was absorbed within a thin layer of the sample, leading to poor coupling of the emitted light to the resonant modes of the periodic structure. The 458 nm excitation penetrated deeper into their samples leading to better coupling of the emission to the resonant modes.

Only slight evidence of the Purcell effect was observed for the 10.5-turn chiral Alq_3 thin film discussed here (Fig. 6.13). The samples with larger numbers of turns did not exhibit any evidence of the Purcell effect. As discussed previously, this was likely a result of the same absorption-based mechanism demonstrated by Woon *et al.* to inhibit the Purcell effect for some of their samples [22]. Thus, only fabricating chiral Alq_3 films with more turns in an attempt to produce films that strongly exhibit the Purcell effect would be insufficient, as the films should be excited with a different wavelength than the 405 nm line used in the experiments presented here.

Defect layers in chiral structures have been predicted and experimentally verified to be useful in the production of low-threshold lasing from cholesteric liquid crystal structures and other chiral films [27, 29]. Defects, such as a non-chiral spacer layer or an instantaneous twist of the chiral structure, introduce a phase discontinuity into the 1D photonic crystal formed by the chiral structure, leading to a narrow bandpass within the stopband produced by the chiral structure. Schmidtke *et al.* [27] fabricated a defect mode in a dye-doped cholesteric polymer network through the careful alignment and lamination of two dye-doped cholesteric polymer films such that a 90° twist was introduced at the junction between the two layers. This yielded two lasing modes: the band edge mode, which occurred for the handedness of light that was suppressed by the chiral structure; and the defect mode, which occurred for the handedness of light that was unaffected by the chiral structure. This was theoretically predicted by Kopp and Genack [29]. The

primary shortcoming of this approach, however, is the difficulty of reliably aligning and laminating the two separate samples to produce the necessary twist defects. Twist defects and spacer layer defects are both easily fabricated in chiral thin films using GLAD or SBD, though, and have been implemented for the fabrication of narrow bandpass filters [30] and sensors [31]. If dye-doped chiral GLAD films could be produced, it would be straightforward to engineer various defects during the fabrication of films to achieve various lasing modes.

A chiral Alq_3 film containing a tilted columnar defect is shown in Fig. 6.19, along with its selective transmittance spectrum. The sample depicted in Fig. 6.19 was similar to sample T, as it was composed of 30 turns (or periods), the majority of which were of a helical morphology, except the 20th one had a tilted columnar morphology. The defect altered the constraints imposed by the structure on the photonic density of states of light in the film, and gave rise to the sharp transmittance peak at 500 nm for RCP light (Fig. 6.19c) [32, 33]. The other transmittance peak at 483 nm was a side lobe of the circular Bragg peak. This preliminary work suggests that film defects may prove useful in future efforts to engineer nanostructured Alq_3 thin films for defect-mode emissive devices similar to those proposed by Kopp and Genack [29], and produced by Schmidtke [27].

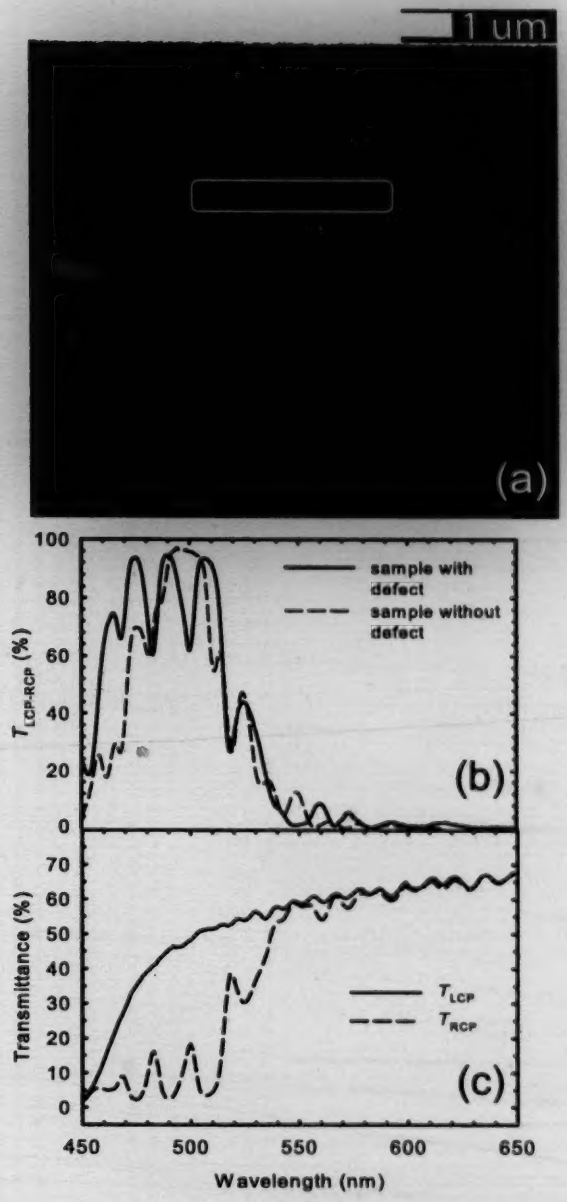

FIGURE 6.19

Optical defects in chiral Alq_3 films. The (a) physical structure of a chiral Alq_3 film with a tilted columnar defect is depicted along with (b) the selective transmittance of circularly polarized light for this sample and for a comparable, defect-free structure (sample T). (c) The presence of the defect state led to a spectral hole within the circular polarization stop band at 500 nm in the right circularly polarized transmittance spectrum [32, 33].

Another interesting possibility is presented by the potential for fabricating a mechanically tunable low-threshold lasing structure. The Young's modulus of Alq_3 is low (~ 2.3 GPa [34]) compared to most inorganic materials (> 100 GPa), and it has been demonstrated that inorganic GLAD helices can be compressed with a nanoindenter [35, 36]. Chiral Alq_3 films should prove even easier to compress. Furthermore, an estimate of the potential electromechanical compression of chiral Alq_3 films has shown that a compression of ~ 30 nm could be achieved with an applied voltage of ~ 100 V [37]. If this compression was achieved through an electromechanical actuation mechanism then the production of tunable, low-threshold lasing structures or tunable narrow bandpass filters would be possible.

6.7 Summary

The optical properties of various novel nanostructured Alq_3 films were characterized using techniques such as VASE, transmission Mueller matrix ellipometry, and Stokes polarimetry. The aim of these studies was to assess the potential use of chiral Alq_3 films as circularly polarized light emitters. As a first step, the principal indices of refraction of tilted columnar Alq_3 thin films fabricated at deposition angles in the range of $70° < \alpha < 90°$ were determined. These data enabled the determination of the normal incidence birefringence of these structures, which was found to increase with deposition angle. The mechanism that caused this behaviour was determined: at higher deposition angles, the columns were tilted to greater degrees with the result that their cross-section in the plane parallel to the substrate became more anisotropic. Additionally, the strength of the circular Bragg phenomena exhibited chiral Alq_3 thin films was found to increase

with deposition angle. These data were used to design and fabricate chiral Alq_3 thin films with large numbers of turns, in order to produce stronger circular Bragg phenomena. These films were indeed shown to produce strong circular Bragg phenomena, with the strongest phenomenon being observed for a 40-turn sample. The 40-turn chiral film yielded a selective transmittance of circularly polarized light and a degree of circular polarization of the photoluminescent output of 98 % and 71 %, respectively. These results were compared with values obtained for other vacuum-deposited chiral thin films and cholesteric LC or polymer media. The circular Bragg phenomena of the chiral Alq_3 films were on a comparable scale to some of the other media, in spite of the porosity of the chiral Alq_3 films. By achieving such strong circular Bragg phenomena for porous chiral films, it may be possible to use these films for sensing applications, or for forming hybrid media with device applications [24]. Additionally, some band edge enhanced emission was observed for one-handedness of circularly polarized photoluminescence from chiral Alq_3 films, which may be used as the basis of a band edge lasing device in the future.

References

1. I. Hodgkinson, Q. H. Wu, and S. Collett, "Dispersion equations for vacuum-deposited tilted-columnar biaxial media," *Applied Optics*, **40**, 452 (2001).
2. I. Hodgkinson, Q. H. Wu, B. Knight, A. Lakhtakia, and K. Robbie, "Vacuum deposition of chiral sculptured thin films with high optical activity," *Applied Optics*, **39**, 642 (2000).
3. Q. H. Wu, I. J. Hodgkinson, and A. Lakhtakia, "Circular polarization filters made of chiral sculptured thin films: experimental and simulation results," *Optical Engineering*, **39**, 1863 (2000).

4. J. Gospodyn and J. C. Sit, "Characterization of dielectric columnar thin films by variable angle Mueller matrix and spectroscopic ellipsometry," *Optical Materials*, in press (2006).

5. E. Collett, *Polarized Light: Fundamentals and Applications*, Marcel Dekker, New York (1993).

6. J. F. Young, J. E. Sipe, J. S. Preston, and H. M. van Driel, "Laser-induced periodic surface damage and radiation remnants," *Applied Physics Letters*, **41**, 261 (1982).

7. J. F. Young, J. S. Preston, H. M. van Driel, and J. E. Sipe, "Laser-induced periodic surface structure. II. Experiments on Ge, Si, Al, and brass," *Physical Review B*, **27**, 1155 (1983).

8. A. B. Djurišić, C. Y. Wong, W. L. Guo, T. W. Lau, E. H. Li, Z. T. Liu, H. S. Kwok, L. S. M. Lam, and W. K. Chan, "Spectroscopic ellipsometry of the optical functions of *tris* (8-hydroxyquinoline) aluminum (Alq_3)," *Thin Solid Films*, **416**, 233 (2002).

9. C. Himcinschi, N. Meyer, S. Hartman, M. Gersdorff, M. Friedrich, H.-H. Johannes, W. Kowalsky, M. Schwambera, G. Strauch, M. Heuken, and D. R. T. Zahn, "Spectroscopic ellipsometric characterization of organic films obtained via organic vapor phase deposition," *Applied Physics A*, **80**, 551 (2005).

10. I. Hodgkinson and Q.H. Wu, "Serial bideposition of anisotropic thin films with enhanced linear birefringence," *Applied Optics*, **38**, 3621 (1999).

11. I. Hodgkinson and Q.H. Wu, *Birefringent Thin Films and Polarizing Elements*, World Scientific, Singapore (1998).

12. A. C. van Popta, J. C. Sit, and M. J. Brett, "Optical properties of porous helical thin films," *Applied Optics*, **43**, 3632 (2004).

13. D. Vick, T. Smy, and M. J. Brett, "Growth behavior of evaporated porous thin films," *Journal of Materials Research*, **17**, 2904 (2002).

14. J. B. Sorge, A. C. van Popta, J. C. Sit, and M. J. Brett, "Effect of porosity on optical properties of chiral films," *Proceeding of SPIE*, **5931**, paper #55.

15. K. Bjorknas, P. Raynes, and S. Gilmour, "Effects of molecular shape on the photoluminescence of dyes embedded in a chiral polymer with a photonic band gap," *Journal of Materials Scienc: Materials in Electronics*, **14**, 307 (2003).

16. S. H. Chen, D. Katsis, A. W. Schmid, J. C. Mastrangelo, T. Tsutsui, and T. N. Blanton, "Circularly polarized light generated by photoexcitation of luminophores in glassy liquid-crystal films," *Nature*, **397**, 506 (1999).

17. K. L. Woon, M. O'Neill, G. J. Richards, M. P. Aldred, S. M. Kelly, and A. M. Fox, "Highly circularly polarized photoluminescence over a broad spectral range from a calamitic, hole-transporting, chiral nematic glass and from an indirectly excited dye," *Advanced Materials*, **15**, 1555 (2003).

18. V. I. Kopp, Z.-Q. Zhang, and A. Z. Genack, "Lasing in chiral photonic structures," *Progress in Quantum Electronics*, **27**, 369 (2003).

19. A. C. van Popta, M. J. Brett, and J. C. Sit, "Double-handed circular Bragg phenomena in polygonal helix thin films," *Journal of Applied Physics*, **98**, 083517 (2005).

20. E. M. Purcell, "Spontaneous emission probabilities at radio frequencies," *Physical Review*, **69**, 681 (1946).

21. D. Z. Garbuzov, V. Bulović, P. E. Burrows, S. R. Forrest, "Photoluminescence efficiency and absorption of aluminum-tris-quinolate (Alq_3) thin films," *Chemical Physics Letters*, **249**, 433 (1996).

22. K. L. Woon, M. O'Neill, G. J. Richards, M. P. Aldred, and S. M. Kelly, "Stokes parameter studies of spontaneous emission from chiral nematic liquid crystals as a one-dimensional photonic stopband crystal: experiment and theory," *Physical Review E*, **71**, 041706 (2005).

23. J. C. Sit, D. J. Broer, and M. J. Brett, "Alignment and switching of nematic liquid crystals embedded in porous chiral thin films," *Liquid Crystals*, **27**, 387 (2000).

24. J. Schmidtke and W. Stille, "Fluorescence of a dye-doped cholesteric liquid crystal film in the region of the stop band: theory and experiment," *The European Physical Journal B*, **31**, 179 (2003).

25. V. I. Kopp, B. Fan, H. K. M. Vithana, and A. Z. Genack, "Low-threshold lasing at the edge of a photonic stop band in cholesteric liquid crystals," *Optics Letters*, **23**, 1707 (1998).

26. H. Finkelmann, S. T. Kim, A. Muñoz, P. Palffy-Muhoray, B. Taheri, "Tunable mirrorless lasing in cholesteric liquid crystalline elastomers," *Advanced Materials*, **13**, 1069 (2001).

27. J. Schmidtke and W. Stille, "Defect mode emission of a dye doped cholesteric polymer network," *Physical Review Letters*, **90**, 083902 (2003).

28. K. L. Woon, M. O'Neill, G. J. Richards, M. P. Aldred, and S. M. Kelly, "Stokes-parameter analysis of the polarization of light transmitted through a chiral nematic liquid-crystal cell," *Journal of the Optical Society of America A*, **22**, 760 (2005).

29. V. I. Kopp and A. Z. Genack, "Twist defect in chiral photonic structures," *Physical Review Letters*, **89**, 033901 (2002).

30. I. J. Hodgkinson, Q. H. Wu, K. E. Thorn, A. Lakhtakia, M. W. McCall, "Spacerless circular-polarization spectral-hole filters using chiral sculptured thin films: theory and experiment," *Optics Communications*, **184**, 57 (2000).

31. A. Lakhtakia, M. W. McCall, J. A. Sherwin, Q.H. Wu, and I. J. Hodgkinson, "Sculptured-thin-film spectral holes for optical sensing of fluids," *Optics Communications*, **194**, 33 (2001).

32. M. M. Hawkeye, personal communication, January 2006.

33. A. C. van Popta, personal communication, February 2006.

34. Y. Cao, C. Kim, S. R. Forrest, and W. Soboyejo, "Effects of dust particles and layer properties on organic electronic devices fabricated by dust sampling," *Journal of Applied Physics*, **98**, 033713 (2005).

35. M. W. Seto, K. Robbie, D. Vick, M. J. Brett, and L. Kuhn, "Mechanical response of thin films with helical microstructures," *Journal of Vacuum Science and Technology B*, **17**, 2172 (1999).

36. M. W. Seto, B. Dick, and M. J. Brett, "Microsprings and microcantilevers: studies of mechanical response," *Journall of Micromechanics and Microengineering*, **11**, 582 (2001).

37. G. Dice, personal communication, January 2006.

CHAPTER 7
Summary and conclusions

7.1 Summary

Luminescent chiral thin films were fabricated by glancing angle deposition (GLAD) and optically characterized to establish the polarization behavior they exhibit. Fabrication procedures were developed to enable the study of both inorganic Y_2O_3:Eu films and organic Alq_3 films. Experimental observation of circularly polarized luminescence from luminescent chiral thin films was achieved using chiral Y_2O_3:Eu films. Degrees of circular polarization for the photoluminescent emission from chiral Y_2O_3:Eu films as high as 5 % were obtained using films that were ~ 50 % porous. A number of factors limited the ability to improve these results. These included the low normal incidence birefringence of the nanostructures in Y_2O_3:Eu films, nanostructure column broadening, and the necessity to use a high-temperature post-deposition annealing process to improve the crystallinity of the films. Optical characterization, including an initial determination of the principal indices of refraction of tilted columnar Y_2O_3:Eu films, suggested that denser films fabricated at lower deposition angles might yield better results. However, achieving overlap of the spectral locations of the photoluminescent emission band and the circular Bragg phenomenon was a necessary requirement for maximizing the observed

degree of circular polarization for the photoluminescent emission. This was complicated by the high-temperature post-deposition annealing process because the location of the circular Bragg phenomenon would shift relative to the design wavelengths as a result of the annealing process.

The complications and limitations encountered in working with chiral Y_2O_3:Eu films caused the focus of the research to shift to efforts to fabricate and characterize chiral luminescent films from other materials. In doing so, chiral Alq_3 films were successfully fabricated, demonstrating that direct deposition of nanostructured organic thin films with engineered nanoscale morphologies is possible. Using a modified GLAD apparatus with an effusion cell source, nanostructured Alq_3 films were fabricated. The individual nanostructures were found to exhibit no coarsening phenomena during growth. Accordingly, the nanostructures were smooth, uniform, and did not broaden. The individual nanostructures of these chiral films were also found to self-organize into a nearly hexagonal close-packed array with short-range order.

The optical properties of nanostructured Alq_3 films provided other intriguing results. The principal indices of refraction of tilted columnar Alq_3 films were determined for a select range of deposition angles. Analysis of these indices revealed that the normal incidence birefringence of the structures increased with deposition angle. The source of this trend was discovered to be the increasingly elliptical nature of the column cross-section when viewed from normal incidence relative to the substrate. This was a different source of form birefringence than has been observed for inorganic tilted columnar films, which exhibit form birefringence because of their fan-shaped cross-sections. The maximum normal incidence birefringence was approximately 4 times greater than the same factor for the tilted columnar Y_2O_3:Eu films. Between the potential offered by the

smooth, non-broadening structures of the Alq_3 films, and the stronger normal incidence birefringence of such films, it was evident that stronger circular Bragg phenomena could be achieved with chiral Alq_3 films.

Based upon the encouraging optical properties of tilted columnar Alq_3 films, efforts to fabricate chiral Alq_3 films exhibiting strong circular Bragg phenomena were undertaken. The strengths of the circular Bragg phenomena exhibited by chiral Alq_3 films were found to increase with deposition angle, however the overall transmittance of the films simultaneously decreased because of increased scattering. These trends guided the fabrication of chiral Alq_3 films with large numbers of turns that displayed stronger circular Bragg phenomena in both transmittance and photoluminescence modes than the Y_2O_3:Eu films studied in the first half of this work.. The strongest circular Bragg phenomenon was observed in a 40-turn film that displayed a selective transmittance of circularly polarized light of ~ 98 %, and a degree of circular polarization for photoluminescent emission of ~ 71 %. Remarkably, even after 40 turns, the individual nanostructures did not broaden. The structural properties of these chiral Alq_3 films were a substantial improvement over porous inorganic chiral thin films, and the chiral optical properties displayed effects that showed immense potential for photonic device applications.

7.2 Suggested future research

Because the work conducted in this thesis was only an initial exploration of the design and fabrication of nanostructured luminescent thin films fabricated by GLAD, there remains a wide-range of topics to further explore. Studies of the angular emission profiles of luminescent nanostructured thin films fabricated by GLAD are currently under investigation. Efforts to fabricate and characterize gradient index films of both Y_2O_3:Eu and Alq_3 to produce luminescent interference filter structures are also underway, with the aim being to yield gradient index structures for which the Purcell effect might be observed. Similarly, the strong circular Bragg phenomena exhibited by the chiral Alq_3 films studied here suggested that experiments with an alternate excitation source, one that would penetrate deeper into thick chiral Alq_3 films, would be useful in determining their potential for use in low-threshold mirrorless lasing applications. If the results of such experiments demonstrate sufficient enhancement of the photoluminescence at the band edges, then it should be possible to form a mirrorless laser by co-depositing a laser dye, such as 4-(dicyanomethylene)-2-methyl-6-(4-dimethylamino styryl)-4H-pyran (DCM), during the growth of chiral Alq_3 films. Additionally, the porous nature of the chiral Alq_3 films studied here suggests that they may be infiltrated with fluids, including dyes and liquid crystals. It may be possible to form switchable devices, which could be combined with the fabrication of low-threshold lasers using chiral Alq_3 films to yield a switchable lasing device. Appropriate optical and film growth models must also be developed to establish predictive capabilities for designing and reliably fabricating future nanostructured thin film samples for optical applications. Many of these projects are currently progressing and being explored by members of Dr. Brett's research group (James Gospodyn, Matthew Hawkeye, Bryan Szeto, and Shufen Tsoi), as well as external collaborators (Michael Taschuk).

The newly discovered ability to directly fabricate nanostructured organic thin films with GLAD has enabled many new avenues of research that are unrelated to studies of light emitting films. Among these are the study of the mechanical properties of nanostructured Alq_3 films, which are also of interest because the bulk modulus of Alq_3 is much lower than that of most inorganic materials. Accordingly, these films may potentially be compressible, and thus be useful in micro-electro-mechanical system (MEMS) or nano-electro-mechanical system (NEMS) applications. Such results may enable the use of these films as mechanically tunable optical filters. Attempts to expand and enhance the fabrication procedure for the direct deposition of nanostructured organic thin films with GLAD are also underway. These are focused upon the use of lowered substrate temperatures during deposition to enable the fabrication of films from additional organic materials, substrate surface treatments to eliminate the presence of the wetting layer, the use of lithographically defined topography to produce films with ordered arrays in a non-hexagonal arrangement, and the study of the effect of substrate rotation speed on the nanostructure produced. The aim of these efforts is to produce nanostructured organic thin films from specific organic materials, and with other nanostructural morphologies. These efforts to further explore the growth and applications of nanostructured organic thin films are being undertaken by a number of Dr. Brett's graduate students and research associates, including Graeme Dice, Anastasia Elias, Michael Fleischauer, Mark Summers, Bryan Szeto, and Shufen Tsoi.

Ultimately, all of these various efforts are aimed at the development of applications of luminescent GLAD films or organic GLAD films, such as sensors, photovoltaics, electroluminescent devices, interference and polarization filters, lasers, and three-dimensional photonic crystals. These possibilities are likely to benefit from the discoveries described here.

APPENDIX A
Thin film density and z-factor calibration method

As Y_2O_3:Eu is not a standard e-beam evaporation material, the density and z-factor are not readily available in e-beam evaporation guidebooks, such as that provided by Inficon [1]. Such guidebooks do have entries for Y_2O_3, listing the density as the same as the bulk value of 5.01 g/cm^3 and the z-factor as 1.000. Typically, the densities of thin films are lower than the bulk density and the z-factor of 1.000 is listed as being untested in such tables. Two simple procedures [2] were used to determine accurate values for the 5.6 wt% Eu source materials used in the work described in this thesis.

A.1 Thin Film Density Calibration

1. A clean substrate was loaded into the system and affixed to a location near the sensor head for the quartz crystal microbalance.
2. The quartz crystal microbalance (QCM) controller was programmed with the bulk density value, d_o (5.01 g/cm^3 in this case), a z-factor of 1.000, and a tooling factor of 100 %.
3. A fresh quartz crystal was loaded into the sensor head and a short deposition was performed, consisting of 100 – 500 nm of accumulated thickness, t_{QCM}, as measured by the QCM.

4. The substrate was removed from the system and an accurate thickness measurement was obtained, $t_{measured}$, for the deposited film. Acceptable thickness measurement methods used included cross-sectional SEM imaging or contact profilometry.
5. The actual density, d, was be calculated from Eq. A.1.

$$d = d_o \frac{t_{QCM}}{t_{measured}} \qquad \text{(A.1)}$$

A.2 Z-factor Calibration

1. A fresh quartz crystal was loaded into the sensor head.
2. The quartz crystal microbalance (QCM) controller was programmed with an accurate density value, a z-factor of 1.000, and a tooling factor of 100 %.
3. A long deposition was performed, such that the crystal was near failure or had less than 50 % life remaining.
4. The thickness reading on the QCM controller was zeroed.
5. A substrate was loaded into the system and a short deposition was performed, consisting of 100 – 500 nm of accumulated thickness as measured by the QCM using the same crystal as above.
6. The substrate was removed from the system and an accurate thickness measurement was obtained for the deposited film. The crystal was left in the sensor head and care was taken to not alter the state of the QCM controller (i.e. the thickness was not zeroed and controller was left powered on).
7. The z-factor entered in the QCM controller was adjusted until the thickness displayed by it matched the thickness measured for the substrate.

A.3 Results

The methods described above were used on multiple occasions to measure the density and z-factor for Y_2O_3:Eu films deposited from the 5.6 wt% Eu source material, yielding average values of 3.42 g/cm^3 for density and 1.121 for z-factor.

References

1. *Material Evaporation Guide*, Inficon, available via www.inficon.com/en.
2. "Chapter 5," *XTC2 Deposition Controller Manual*, Inficon.

APPENDIX B
Polarized photoluminescence data for Y_2O_3:Eu: an example

The following figure (Fig B.1) shows an example of the data obtained for the polarized photoluminescence measurements in *Chapter 4*, along with the fit to the data of a modified version of Eq. 4.5 that included the effect of the grating. The grating effect was included by multiplying by a factor of $(1 + G\cos(2\psi))$. The parameter, G, was the variability in the transmission of linearly polarized light as it is rotated between being parallel and perpendicular to the grooves of the spectrometer grating, and it was determined from the manufacturer's specifications for the grating. The Stokes parameters and figures of merit were calculated from the fitted curve. The 'linear' data was obtained by measuring the photoluminescent emission for various orientations of the Glan-Taylor polarizer in the output beam path (see Fig. 4.2), but without the quarter waveplate in the output beam path. The 'circular' data was obtained in a similar manner, but with the quarter waveplate in the output beam path.

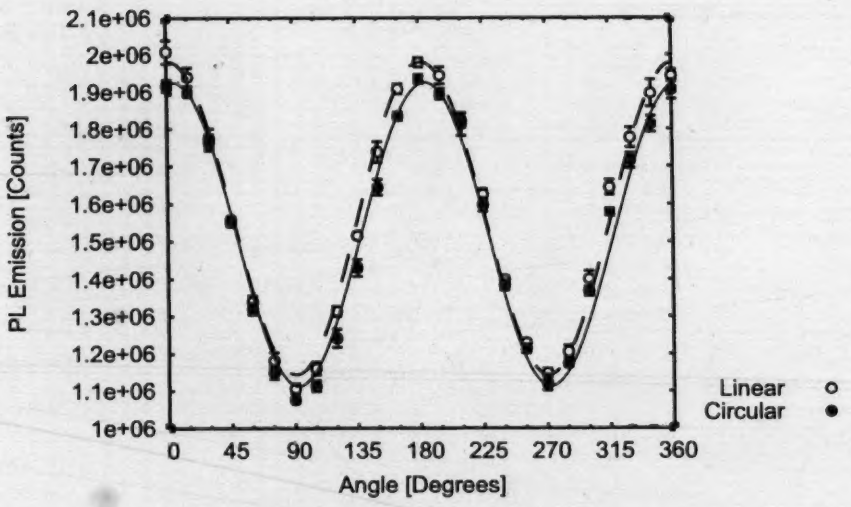

Table 1: Best Fit Stokes Parameters

Parameter	Units	Linear	Circular
S_0	[Counts]	3.141e+06±1.484e+04	3.053e+06±1.717e+04
S_1	[Counts]	-5.716e+04±2.019e+04	-6.218e+04±2.336e+04
S_2	[Counts]	3.125e+04±1.972e+04	
S_3	[Counts]		8.880e+04±2.281e+04

Table 2: Calculated Polarization Parameters

Parameter	Units	Nominal Value	Error
ρ	[N]	0.036	0.007
ρ_c	[N]	0.029	0.007

Appendix C
Stokes parameter measurements of Alq_3 films

For measuring the Stokes parameters of the photoluminescent emission from nanostructured Alq_3 films, the combination of an achromatic quarter waveplate and a Glan-Taylor polarized were placed in the output beam path (see Fig. 6.3). In order to eliminate the effects of the polarization-dependent reflectivity of the spectrometer grating, the rotational position of the polarizer was held fixed such that the polarization state incident upon the spectrometer was the same for every measurement. By altering the rotational positions of the sample and the quarter waveplate, the polarization state incident upon the Glan-Taylor polarizer was varied and the intensity of the output of the Glan-Taylor polarizer varied accordingly. The rotational positions of the sample and the quarter waveplate that enabled the determination of the Stokes parameters were derived in the following manner.

The intensity of light incident upon the spectrometer in Fig. 6.3 can be determined by considering the Mueller matrices of an ideal waveplate and an ideal linear polarizer (Eq. C.1).

$$M_{qw} = \begin{pmatrix} 1 & 0 & 0 & 0 \\ 0 & \cos^2 2\theta + \sin^2 2\theta \cos\Delta & \sin 2\theta \cos 2\theta (1 - \cos\Delta) & -\sin 2\theta \sin\Delta \\ 0 & \sin 2\theta \cos 2\theta (1 - \cos\Delta) & \sin^2 2\theta + \cos^2 2\theta \cos\Delta & \cos 2\theta \sin\Delta \\ 0 & \sin 2\theta \sin\Delta & -\cos 2\theta \sin\Delta & \cos\Delta \end{pmatrix}$$

$$M_{pol} = \frac{1}{2}\begin{pmatrix} 1 & \cos 2\psi & \sin 2\psi & 0 \\ \cos 2\psi & \cos^2 2\psi & \cos 2\psi \sin 2\psi & 0 \\ \sin 2\psi & \cos 2\psi \sin 2\psi & \sin^2 2\psi & 0 \\ 0 & 0 & 0 & 0 \end{pmatrix} \qquad \text{(C.1)}$$

Here ψ is the rotation angle of the polarizer axis relative to the sample, θ is the rotation angle of the fast axis of the quarter waveplate relative to the sample, and Δ is the retardance of the quarter waveplate. The equation determining the output Stokes vector for light passing through these two optical elements is given by Eq. C.2.

$$S_{out} = M_{pol} M_{qw} S_{in} \qquad \text{(C.2)}$$

Thus, the total Mueller matrix for the system is $M = M_{pol} M_{qw}$. The intensity measured by the spectrometer will be given by the first element of S_{out}. Thus, only the first row of M is of interest. This row is then multiplied by a generalized input Stokes vector to obtain Eq. C.3, following some simplification.

$$I(\psi,\theta,\Delta) = \frac{1}{2}\begin{bmatrix} S_0 + S_1\left(\cos 2\psi \cos^2 2\theta + \cos\Delta \sin^2 2\theta + \sin 2\psi \sin 4\theta \sin^2\frac{\Delta}{2}\right) + \\ S_2\left(\sin 2\psi \left(\cos^2 2\theta \cos\Delta + \sin^2 2\theta\right) + \cos 2\psi \sin 4\theta \sin^2\frac{\Delta}{2}\right) + \\ S_3 \sin(2(\psi - \theta))\sin\Delta \end{bmatrix} \qquad \text{(C.3)}$$

From Eq. C.3, it can be seen that certain values of ψ, θ, and Δ give rise to circumstances where I, the intensity measured by the spectrometer, is only a function of two of the input Stokes parameters (the wavelength dependence is ignored here). Accordingly, a measurement system for determining each of the Stokes parameters can be devised simply by finding combinations of ψ, θ, and Δ that ensure that some of the Stokes parameter terms do not contribute to the acquired intensity signal. One such set of orientations is given in Eq. C.4.

$$
\begin{aligned}
I\left(0°, 0°, 90°\right) &= \frac{1}{2}\left[S_0 + S_1\right] \\
I\left(-90°, -90°, 90°\right) &= \frac{1}{2}\left[S_0 - S_1\right] \\
I\left(-45°, -45°, 90°\right) &= \frac{1}{2}\left[S_0 - S_2\right] \\
I\left(0°, -45°, 90°\right) &= \frac{1}{2}\left[S_0 + S_3\right]
\end{aligned}
\qquad \text{(C.4)}
$$

Measurements can then be obtained by noting that Eq. C.4 assumes a constant sample orientation. Rotational positions for the sample and the quarter waveplate can be determined that effectively produce the orientations given in Eq. C.4, but without requiring the rotational position of the polarizer to be changed.